Title
Laser Trapping of 21 Na Atoms

Author
Lu, Zheng-Tien

Publication Date
1994-09-13

LBL-36120
UC-413

Lawrence Berkeley Laboratory
UNIVERSITY OF CALIFORNIA

Laser Trapping of ^{21}Na Atoms

Z.-T. Lu
(Ph.D. Thesis)

September 1994

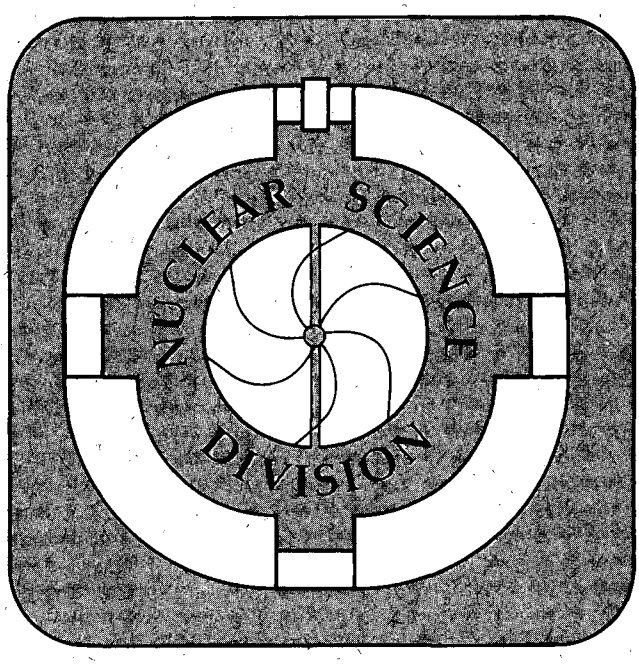

Prepared for the U.S. Department of Energy under Contract Number DE-AC03-76SF00098

DISCLAIMER

LBL-36120

Laser Trapping of ^{21}Na Atoms

by

Zheng-Tian Lu

Ph.D. Thesis

Department of Physics

University of California at Berkeley

and

Nuclear Science Division

Lawrence Berkeley Laboratory

University of California

Berkeley, CA 94720

September 1994

This work was supported by the Director, Office of Energy Research Division of Nuclear Physics of the Office of High Energy and Nuclear Physics of the U.S. Department of Energy under Contract DE-AC03-76SF00098.

Abstract

Laser Trapping of ^{21}Na Atoms

by

Zheng-Tian Lu

Doctor of Philosophy in Physics

University of California at Berkeley

Professor Stuart J. Freedman, Chair

This thesis describes an experiment in which about four thousand radioactive ^{21}Na ($t_{1/2}$ = 22 sec) atoms were trapped in a magneto-optical trap with laser beams. Trapped ^{21}Na atoms can be used as a beta source in a precision measurement of the beta-asymmetry parameter of the decay of $^{21}Na \rightarrow {}^{21}Ne + \beta^{+} + \nu_e$, which is a promising way to search for an anomalous right-handed current coupling in charged weak interactions. Although the number of trapped atoms that we have achieved is still about two orders of magnitude lower than what is needed to conduct a measurement of the beta-asymmetry parameter at 1% of precision level, the result of this experiment proved the feasibility of trapping short-lived radioactive atoms. In this experiment, ^{21}Na atoms were produced by bombarding ^{24}Mg with protons of 25 MeV at the 88" Cyclotron of Lawrence Berkeley Laboratory. A few recently developed techniques of laser manipulation of neutral atoms were applied in this experiment. The ^{21}Na atoms emerging from a heated oven were first transversely cooled. As a result, the on-axis atomic beam intensity was increased by a factor of 16. The atoms in the beam were then slowed down from thermal speed by applying Zeeman-tuned slowing technique, and subsequently loaded into a magneto-optical trap at the end of the slowing path. The last two chapters of this thesis present two studies on the magneto-optical trap of sodium atoms. In particular, the mechanisms of magneto-optical traps at various laser frequencies and the collisional loss mechanisms of these traps were examined.

To my grandmother Ms. Qin-Luan Xia, mother Ms. Ying-Hua Wang, and father Mr. Xiao-Jiang Lu, who raised me up in a difficult time before China turned around.

To my wife Ms. Diyang Wu for love.

To my son Peter, whose born added new meaning into everything I do.

To my teachers, who molded me into a person whom I like.

Table of Contents

List of Figures

Acknowledgment

First of all, I would like to thank my advisor, Stuart Freedman, for providing me the opportunity to work on a very rewarding thesis project. Throughout the project, he guided when I was puzzled, encouraged when I was troubled, and forgave when I made mistakes. He also provided a stable financial support which is very important to me and my family.

I am grateful to Song-Quan Shang, whose deep insight, ingenious experimental skills, and tremendous energy brought successes to this project. I will never forget the moment when Shang dashed back to the laser room, fists in the air, and announced that he saw trapped ^{21}Na atoms. I thank Brian Fujikawa, who made me to do things with a higher standard. I thank Kevin Coulter, who started this project and turned me into a student in the field of experimental physics. I thank my other colleagues who also participated in this project, in particular Linda Young, Chris Bowers, Justin Mortara, Eric Wasserman, and Kevin Yasumura.

I thank Eugene Commins and Harry Lee, for their support, wisdom, encouragement, and advice. I thank many people in the field of laser trapping and cooling, who provided their expertise to help this project, in particular Carl Wieman, Bill Phillips, Steve Rolston, and Fujio Shimizu.

I thank Claude Lyneis and the staff of the 88" Cyclotron at the Lawrence Berkeley Laboratory for their essential support. I thank the machinists of the 88" Cyclotron and the

physics department of UC Berkeley, who helped building the beamlines for this project. Special thanks to Andy Brocato for making two tapered solenoids.

I spent my joyful graduate school years in four excellent institutions. I am grateful to people at the physics department of University of California at Berkeley, the Nuclear Science Division of Lawrence Berkeley Laboratory, the physics department of University of Chicago, and the Physics Division of Argonne National Laboratory.

Chapter I

Introduction

1.1 Laser Manipulation of Neutral Atoms

It all started in 1975, when the idea of laser cooling was proposed independently by Theodore W. Hänsch and Arthur L. Schawlow of Standford University for a gas sample of atoms [HA75] and by Dave Wineland and Hans G. Dehmelt of the University of Washington for trapped ions [WI75]. They proposed that atoms (or ions) can be slowed by interacting with light whose frequency is detuned below the atomic resonance. Since then, laser manipulation of atoms and ions has grown into a major sub-field of atomic physics.

Looking back, a few memorable achievements stand out. Laser cooling was first demonstrated on trapped ions in 1978 by D. J. Wineland et al. at National Bureau of Standards [WI78]; laser deceleration of an atomic beam was first demonstrated in 1982 by William D. Phillips and Harold Metcalf at National Bureau of Standards [PH82]; magneto-optical trap was first demonstrated in 1987 by E. L. Raab et al. at AT&T Bell laboratories at Holmdel [RA87]; and sub-Doppler cooling was discovered in 1988 by P. D. Lett et al. at, once again, the National Bureau of Standards [LE88].

The developments in this field were aided by sophisticated industrial technologies. The single-mode dye laser was the single most important tool in the experiments noted in the previous paragraph. The demands of the telecommunication industry lead to the production of the inexpensive diode lasers, various types of optical modulators and optical fiber, which are widely used in laser manipulation experiments.

By now, almost twenty years after the original idea, the techniques of laser manipulation have matured enough to be applied to fundamental problems. Cold collisions between trapped atoms have been studied with a number of alkali elements (see Chapter X), and isotope shifts of metastable xenon atoms were measured [WA93]. Many applications are still under development. For example, greatly extending the measurement time, the atomic fountain [KA91] seems ideal for providing extremely precise spectroscopic information, which may be useful in experimental searches for atomic EDM (permanent Electric Dipole Moment), measurements of the atomic parity mixing effects and the next generation of measurements leading to a better atomic frequency standard. Atom optics became a very active field with the demonstrations of mirrors [AM93], beam splitters and gratings for atoms. Outside of atomic physics, in the work described in this thesis, short lived radioactive atoms (^{21}Na, $t_{1/2} = 22$ sec) were recently trapped for the first time. With this demonstration it is now clear that rare and radioactive atoms can be trapped, making a number of new and sensitive studies of the weak interaction possible. Applications of radioactive atom trapping may lead to other useful applications in addition to fundamental experiments of atomic, nuclear and particle physics. The most exciting applications are probably not yet discovered.

1.2 Why Trapping Radioactive Atoms

There is no essential difference between trapping stable atoms and trapping radioactive atoms. In practice, however, the shorter the lifetime, the more difficult it is to trap. While it is extremely difficult to trap radioactive atoms of milli-seconds of half-life, the ^{87}Rb atoms whose half-life is 50 billion years were trapped with the same procedures used on its stable partner, ^{85}Rb. In between the extremes, trapping is feasible but made difficult because of the short supply of the radioactive atoms.

There are at least two current problems which motivated us to develop techniques for trapping short lived isotopes. The first involves the study of atomic parity mixing. Extending these measurements to radioactive species may improve our knowledge of the Weinberg angle as we discuss in Sec. 2.2. The second involves studies of nuclear decays. Sources of trapped radioactive atoms could lead to a new generation of high precision experiments. One example is considered in Section 2. 1.

1.3 A Typical Atom Trap

There are different types of atom traps, the magneto-optical trap (MOT) is the most popular one due to its large trap depth and its stability. It has been the work-horse for all the applications noted in the previous section. The parameters of the MOT vary widely. Considered here is only a working example, serving as an introduction to detailed descriptions in subsequent chapters.

Figure 1.1 shows the main elements of a MOT. In a typical MOT, 10^7 sodium atoms are trapped in a region with a diameter of 1 mm. The atoms are confined by the incoming photons from the six directions. A bright spot can be seen by eyes since the trapped atoms constantly absorb and emit photons. The spin orientation of the trapped atoms are randomly distributed.

The laser beams are circularly polarized, with their polarization directions arranged as drawn in Figure 1.1. The diameter of the laser beams is about 1 cm, and the light intensity of each beam is around 10 mW/cm^2. The frequency of the laser is 10 MHz less than the frequency of the resonance transition between $3S_{1/2}$ F=2 ground state and $3P_{3/2}$ F'=3 excited state of sodium, whose natural linewidth is 10 MHz. With frequency detuned, the laser light cools as well as traps, which is an essential feature of a stable trap. The effective temperature of the trapped atom ensemble is about 1 mK.

A two loop Helmholtz coil provides the essential magnetic field. Unlike the usual Helmholtz arrangement, the currents in the two coils are opposing, so the resulting magnetic field is a quadrupole field with cylindrical symmetry. The atoms are trapped near the center where the field strength is zero and the gradient of field strength is about 10 Gauss/cm.

Such a trap has an effective potential depth of 0.5 Kelvin and capture speed of 20 m/s, i.e. those atoms that enter the region where laser beams cross with speed less than 20 m/s are likely to be captured. Obviously, a collision between a trapped atom and a free atom or molecule at thermal speed (600 m/s) will free the trapped atom so ultra-high vacuums are important. At 1 x 10^{-9} Torr of vacuum pressure, in average, an atom stays in the trap for about 3 seconds. The 10^7 atoms in the trap reflects a dynamic balance between capture and loss.

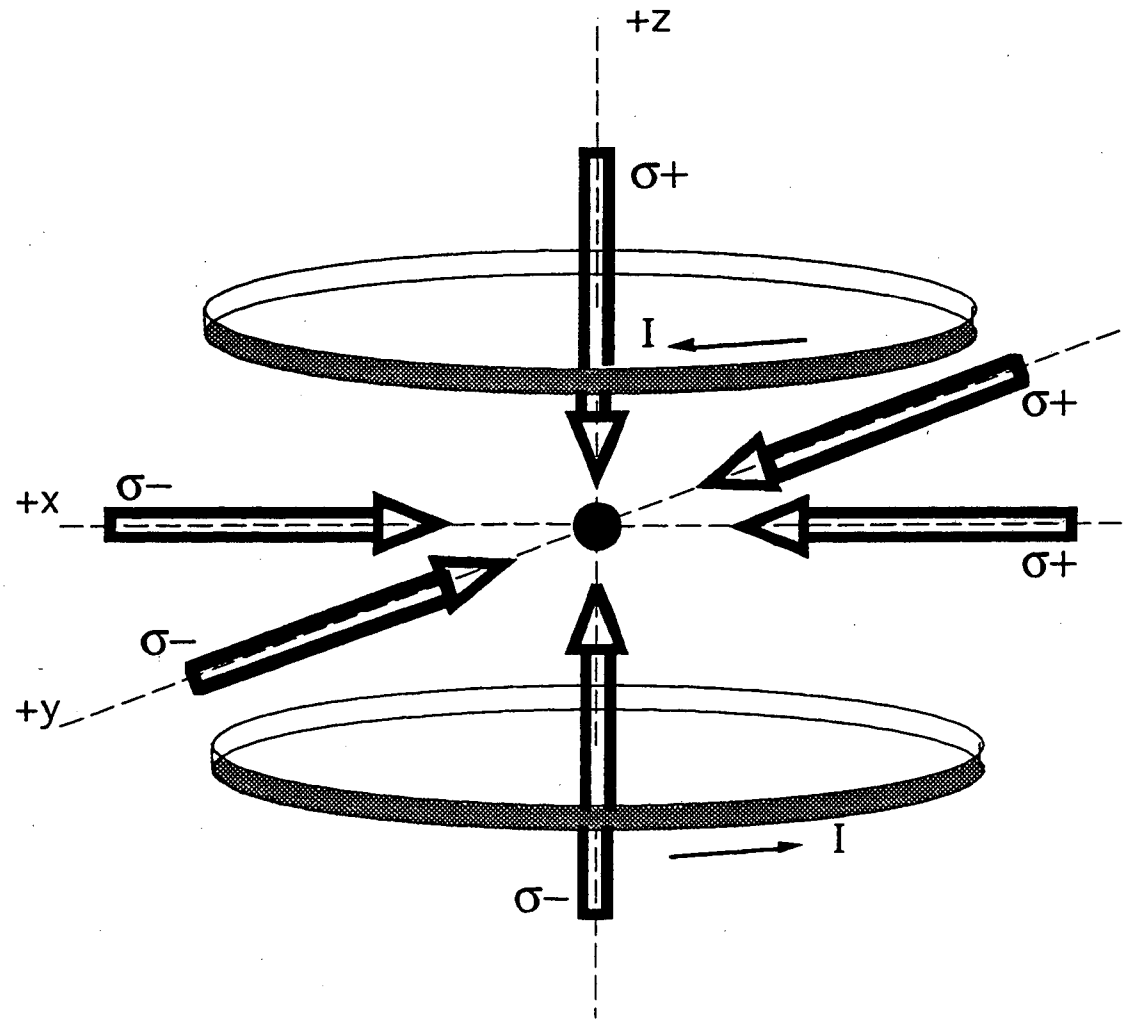

Figure 1.1 A typical magneto-optical trap geometry. Atoms are trapped in the center region at the null magnetic field generated by two coils carrying currents in opposite directions. Laser beams are indicated by heavy arrows. Their polarization directions are marked with reference to the spatial axis of the drawing.

Chapter II

Applications of Trapped Radioactive Atoms

2.1 The Beta-Asymmetry Parameter of ^{21}Na

2.1.1 Beta-Asymmetry Parameter

As a consequence of non-invariance of the weak interaction with respect to spatial reflection symmetry, the angular distribution of beta particles emitted by polarized nuclei display an "up-down" asymmetry, i.e. a difference in the emission probability between θ and $180°-\theta$ (see Fig 2.1), where θ is the angle between the momentum of the beta particle and spin of the nucleus. A measurement of this effect was proposed by Tsung Dao Lee and Chen Ning Yang as a test of parity invariance of the weak interaction [LE56]. Less than a year later, the asymmetry was observed on the beta decay of ^{60}Co by C. S. Wu et al. [WU57], thus confirming the existence of parity violation.

In the present Standard Model of the Weak and Electromagnetic Interaction [HO89], only left-handed currents are coupled by weak interaction and the angular distribution of beta particles can be formulated as

$$d\Gamma \propto [1 + AP\frac{v}{c}\cos(\theta)]d\Omega \quad . \qquad (2.1)$$

Here Γ is the decay rate; **A**, is the Beta-asymmetry parameter; $P=\langle I_z\rangle/I$ is the polarization of the nuclei; v is the speed of the beta particle; and Ω is the solid angle.

A has been measured in many systems, including the "mirror decays" of Neutron [BO86], ^{19}Ne [CA75], ^{17}F [SEV89], ^{29}P [MAS90], and ^{35}Ar [GA88]. A mirror decay is a beta decay that the parent nucleus and the daughter nucleus form an iso-doublet, the two nuclei have the same spin, and the number of neutrons (protons) of the parent nucleus equals to the number of protons (neutrons) of the daughter nucleus.

2.1.2 Measuring A as a Test of the Standard Model

The beta-asymmetry parameter, **A**, is a characteristic property of a decay channel of a nucleus and can be calculated with nuclear form factors. **A** is slightly dependent on the energy of beta particles. In the case of β^+ mirror decay, following the notation of [HO89], the value of **A** extrapolated to zero kinetic energy of beta particles can be formulated as

$$A(0)=\frac{\frac{1}{j+1}-2\sqrt{\frac{j}{j+1}}\left(\frac{a}{c}\right)+T_1}{1+\left(\frac{a}{c}\right)^2+T_2} \qquad (2.2)$$

Here j is the spin of the nucleus; **a** is the vector form factor and **c** is the axial-vector form factor; T_1 and T_2 are the contributions from the induced nuclear form factors.

While factor a can be predicted by the Conserved Vector Current Hypothesis, which is now a part of the Standard Model, factor c can be obtained from another measurement, for example the half-life of the decay, through the following relation:

$$f^R t_{\frac{1}{2}} = \pi^3 \ln 2 \frac{1}{G_F{}^2 \cos^2\theta_c \left(a^2 + c^2 + T_3\right)} \qquad (2.3)$$

Here f^R is the integrated phase space factor corrected by the effect of the electromagnetic interaction between the daughter nucleus and the outgoing beta particle, including radiative corrections; $t_{1/2}$ is the half-life; G_F is the Fermi coupling constant; θ_c is the Cabbibo angle; and T_3 is the contribution from the induced nuclear form factors.

The induced terms, T_1, T_2 and T_3, are on the order of the beta particle energy divided by the nucleon mass, $O(10^{-3})$ in general. They are dominated by the contribution from weak magnetism. According to the Conserved Vector Current Hypothesis, the weak magnetism term of a mirror decay can be precisely calculated from measured nuclear magnetic moments of the parent and daughter nucleus.

In the case of ^{21}Na decaying to ^{21}Ne through positron emission (see Appendix C), there are two decay channels, each has its own beta-asymmetry parameter. From the measured half-life and branching ratio, the beta-asymmetry parameter of the main branch can be calculated [NA91],

$$\begin{aligned} A\left(\frac{3^+}{2} \rightarrow \frac{3^+}{2}\right) &= \frac{\frac{2}{5} + \sqrt{\frac{12}{5}}\left(\frac{a}{c}\right)}{1 + \left(\frac{a}{c}\right)^2} + T \\ &= 0.862 - 0.002(\text{induced term}) \pm 0.006 \\ &= 0.860 \pm 0.006 \end{aligned} \qquad (2.4)$$

The other branch, $3/2^+ \rightarrow 5/2^+$, is a pure Gamow-Teller decay and its beta-asymmetry parameter can be calculated as

$$A\left(\frac{3^+}{2} \rightarrow \frac{5^+}{2}\right) = -\frac{3}{5} + T' \quad . \tag{2.5}$$

The induced correction T' is not known precisely, but it can be neglected at current precision level since its contribution to the measured asymmetry is reduced by the small branching ratio.

Now a relation between $A\left(\frac{3^+}{2} \rightarrow \frac{3^+}{2}\right)$ and $t_{1/2}$ is established. Although the procedures are tedious, all of them are contained in the Standard Model. Therefore, values of $A\left(\frac{3^+}{2} \rightarrow \frac{3^+}{2}\right)$ and $t_{1/2}$ of a mirror decay can be combined to test the Standard Model. In order to know how sensitive this test is, we need a counter model. The Left-Right Symmetric Model [BE77] is such a counter model that is very fashionable nowadays.

2.1.3 Measuring A to Search for Right-Handed Coupling

Based on the gauge group of $SU(2)_L \otimes SU(2)_R \otimes U(1)$, the Left-Right Symmetric Model [BE77, NA91] is an extension of the Standard Model of the electro-weak interaction. For the charged current weak interaction, the LRS model proposes two gauge bosons, W_R and W_L, with the mass of W_R much higher than the mass of W_L as a consequence of spontaneous left-right symmetry breaking, in order to explain that only left-handed coupling is observed at low energies accessible to current experiments. The LRS model

can be parametrized in terms of two parameters, a mixing angle ζ and a mass-square ratio δ. The mixing angle is needed since the gauge boson eigenstates of charged current weak interaction, W_R and W_L, are not necessarily the same as their mass eigenstates, W_1 and W_2. Instead, they are related by

$$\begin{aligned} W_1 &= W_L \cos\zeta - W_R \sin\zeta \\ W_2 &= W_L \sin\zeta + W_R \cos\zeta \end{aligned} \tag{2.6}$$

With M_1 and M_2 defined as the mass of W_1 and W_2 respectively, the second parameter is defined by

$$\delta = \left(M_1 / M_2 \right)^2 \tag{2.7}$$

Since the experimental tests of the Standard Model have all been positive, it is expected that $M_1 \approx 80\ \mathrm{GeV/c^2}$, $M_1 << M_2$ and $\delta, \zeta << 1$. In fact, this model reduces to the Standard Model when δ, ζ are set to zero.

Non-zero δ and ζ would result in anomalous experimental observables. Many experiments have been conducted to search for such a tiny effect. So far, all valid results agree with the Standard Model so they are used to limit the parameter space of the LRS Model. Among them, the muon decay asymmetry experiment [JO86], in which the angular distribution of the electrons from the decay of polarized muons are measured, generated the most stringent limit on the parameters (see Fig. 2.2). Non-zero parameters would modify the values of $t_{1/2}$ and $A\left(\frac{3^+}{2} \rightarrow \frac{3^+}{2}\right)$ described in the previous section so precision measurements of $t_{1/2}$ and $A\left(\frac{3^+}{2} \rightarrow \frac{3^+}{2}\right)$ can be used to search for the right-handed coupling. In fact, the beta-asymmetry measurements on Neutron and ^{19}Ne with a

precision of a few percent have been playing an active role in limiting the parameter space [NA91] (see Fig. 2.2). Also shown in Figure 2.2 is the limit that would be set by future beta-asymmetry measurements on ^{21}Na if the measured $A\left(\frac{3^+}{2} \rightarrow \frac{3^+}{2}\right)$ has the expected value, 0.860, at a precision of 1%. On the other hand, if the measured $A\left(\frac{3^+}{2} \rightarrow \frac{3^+}{2}\right)$ disagree with and is less than the expected value, then it may indicate the existence of right-handed coupling in weak interaction.

2.1.4 Measurements of the Parameter A

Figure 2.3 shows the arrangements of a typical experiment to measure the beta-asymmetry parameter. It consists of two beta detectors, an Upper and a Lower detector, and a sample of polarized nuclei. A can be obtained from equation

$$\frac{N_U(E)-N_L(E)}{N_U(E)+N_L(E)} = APG\frac{v}{c} \quad , \tag{2.8}$$

which is derived from Equation (2.1) by integrating over the finite size of the beta source and beta detectors. Here $N_U(E)$ and $N_L(E)$ are the counting rates of the Upper and Lower detector respectively, and G is the geometric factor, obtained by averaging $\cos(\theta)$ over the finite size of the nuclei source and the detectors.

The main experimental challenge is the production of a polarized beta source with the polarization known precisely. In order to make a new contribution in limiting the parameter space of the LRS Model, the relative error of A has to be around 1%, and so is

the relative error of the polarization. Described below are several ingenious techniques developed for this purpose:

1) ^{60}Co, $A = -1.01 \pm 0.02$. Twenty years after the demonstration of parity violation in the beta decay of ^{60}Co, the beta-asymmetry parameter was re-measured to a high level of precision [CH80]. In this experiment, ^{60}Co atoms are thermally diffused into a foil of ferromagnetic material, which is attached to a dilution refrigerator. About 50% polarization is obtained at 0.02 K of temperature. The polarization is determined by measuring the anisotropy of the gamma emission following the beta decay.

2) Neutron, $A = -0.1146 \pm 0.0019$. This measurement is done with a cold neutron beam. Polarizations greater than 97% can be achieved by reflecting neutrons from a magnetized ferromagnetic mirror. A second polarizer is used to measure the polarization with 0.5% of relative error.

3) ^{19}Ne, $A = -0.0391 \pm 0.0014$. A Stern-Gerlach magnet is used in this experiment to select out a part of a ^{19}Ne atomic beam with one polarization. The selected atomic beam is fed into a cell where beta decay is measured. Since the atomic electron shells are closed, the nuclear polarization is protected from fast degradation due to wall collisions. The initial polarization is assumed to be complete, and 1% of relative error on average polarization arises from collisional relaxation.

The main sources of errors in a measurement of A can be identified by examining Equation 2.8. They are:

1) Scattering of beta particles. Instead of traveling directly to a detector after being emitted, a beta particle can change direction by scattering from surrounding material,

including the detectors and the source itself. The scattered beta particles introduce errors to the counting rate $N_U(E)$ and $N_L(E)$. This is the most severe when a solid source (^{60}Co) is used.

2) Uncertainty in the polarization of the source. In order to obtain the largest possible signal to noise ratio, the polarization of the source nuclei is preferably to be close to 1 .

3) Geometric factor. The systematic uncertainty in its evaluation is less for a compact beta decay source. In practice, this factor is modified by the spatial distribution of detector efficiency. The systematic error introduced in evaluating this factor is the least for a solid source and more for a gas cell source (^{19}Ne).

2.1.5 Trapped ^{21}Na Atoms as Beta Source

Using the trapped ^{21}Na atoms as beta source would reduce all three errors listed above. First, since the atoms are confined by laser light, beta scattering is reduced to minimum. Arrangements can be made so the closest objects to the source are the beta detectors. Scattering from detectors is inevitable, but this effect can be corrected by examining the response function of the detector. Second, the complications of determining the geometric factor are essentially eliminated with a localized trapped source. Third, although the atoms in a magneto-optical trap are randomly oriented (P=0), two schemes have been suggested to overcome this problem.

The trapped atoms in the MOT can be further loaded into a new polarized atom trap, for example, an Ioffe trap [PR83]. The Ioffe trap is a magnetic field gradient trap and its trap

potential is $-\vec{\mu}\cdot\vec{B}$ with μ the magnetic moment of atoms. The trap consists two current loops and four bars arranged as in Figure 2.4, generating a magnetic field local minimum at the geometric center. Only those atoms in weak field seeking states, i.e. states with $M_F > 0$, can be trapped. Since the depth of an Ioffe trap is shallow, pre-loading procedures are necessary. In preparation, atoms are loaded to a MOT located at the center of the Ioffe trap while the magnetic field of the Ioffe trap is turned off. Then the atoms are cooled in an optical molasses and finally optically pumped to the right state before turning on the Ioffe trap. These techniques have already been demonstrated with cesium atoms [MO90]. Figure 2.4 shows a specific design of an Ioffe trap. If we assume that 100 Amp-turn currents flow through the loops and bars, and atoms are pre-cooled to about 15 cm/sec, then this trap can contain the sample in an ellipsoidal region with a bound of 2 mm from the center in the axial direction and 1 mm from the center in the radial direction. The magnetic field within the ellipsoid is nearly uniform since the axial field of 36 Gauss is much larger than the radial component, which results in the polarization of trapped atoms being >99%. The correction to the effective solid angle of detectors caused by the focusing of beta particles by magnetic field ($< 0.01\%$) is negligible.

Another possible scheme is to recycle trap-cool-polarize processes repeatedly. First, atoms are loaded into a MOT; second, the MOT is turned off and atoms are cooled in an optical molasses to low speed, about 15 cm/sec; third, atoms are polarized to near 100% by optical pumping; and before the atoms fly away, the trap is turned back on and the next cycle begins. Beta counting can be done during the period when atoms are polarized. These schemes are currently being developed in our laboratory.

Another important advantage of this technique is that the source of laser trapped atoms is isotopically pure. The resonance condition of the atom-light interaction ensures that only

atoms of one particular isotope of one particular element are trapped at a given laser frequency. Further improvement can be realized by transporting trapped atoms to a low background counting area several meters away, well shielded from the nuclear reaction region.

2.1.6 The Statistical Error of A

In order to know how many trapped atoms are needed in the asymmetry parameter measurements, data analysis is conducted on simulated data to examine how the number of trapped atoms affects the statistical error of the measured $A\left(\frac{3^+}{2} \rightarrow \frac{3^+}{2}\right)$. The simulation assumes an experimental arrangement as in Figure 2.3. It is also assumed that the average solid angle subtended by each detector towards the trapping center is Ω_T = 0.1 std, the polarization of trapped atoms is complete (P=1), and there is no background beta emission.

The expected numbers of counts are calculated in two steps: First, a beta spectrum is generated as

$$N_1(E) = N_0 \cdot \left[B_1 E\sqrt{E^2 - m^2}(E_1 - E)^2\right]$$
$$N_2(E) = N_0 \cdot \left[B_2 E\sqrt{E^2 - m^2}(E_2 - E)^2\right] \qquad (2.9)$$

where E and m are the energy and mass of beta particles respectively, N_0 is the total number of beta particles emitted in the trap, sub-index 1 and 2 correspond to the two decay channels, $N_1(E)$ is number of beta particles emitted with energy in the range of

$E-\frac{1}{2}\delta$ and $E+\frac{1}{2}\delta$ with d set at 1 keV, B_1 is the normalization factor to ensure the right branching ratio, E_1 is the end point, and N_2, B_2 and E_2 are the corresponding parameters of the other decay channel. The expected numbers of counts registered in the top and bottom beta detectors can then be calculated as

$$N_T(E) = N_1(E)\int_{\Omega_T}\left[1+A_1P\frac{v}{c}\cos(\theta)\right]d\Omega + N_2(E)\int_{\Omega_T}\left[1+A_2P\frac{v}{c}\cos(\theta)\right]d\Omega$$
$$N_B(E) = N_1(E)\int_{\Omega_T}\left[1-A_1P\frac{v}{c}\cos(\theta)\right]d\Omega + N_2(E)\int_{\Omega_T}\left[1-A_2P\frac{v}{c}\cos(\theta)\right]d\Omega \quad , (2.10)$$

where P = 1, $A_1 = A\left(\frac{3^+}{2} \rightarrow \frac{3^+}{2}\right) = 0.860$, and A_2 = -0.600 as predicted by the Standard Model. The simulated experimental data are then generated around the expected values. Two histograms, $N'_T(E)$ and $N'_B(E)$, are generated, assuming they follow Gaussian distributions, with $N_T(E)$ and $N_B(E)$ as expected values respectively, and $\sigma_T(E) = \sqrt{N_T(E)}$, $\sigma_B(E) = \sqrt{N_B(E)}$ as standard deviations.

These two histograms are then fit with functions (2.9) and (2.10) with the two normalization factors (B'_1 and B'_2) and two beta asymmetry parameters (A'_1 and A'_2) as free parameters. The best fitting value of A'_1 is taken as the simulated experimental data and its deviation from the 'true' value (0.860) is calculated. These simulation procedures are conducted one hundred times for each assumed experimental condition.

The simulation results demonstrated that a relative precision of 7.1% on the beta asymmetry parameter of the main decay channel is obtained when 1 x 10^8 trapped atoms decay during counting periods, the average beging $Ave(A_1) = 0.873$ and the standard deviation from the 'true' value being $\sigma(A_1) = 0.061$; a relative precision of 1.7% ($Ave(A_1)$

$= 0.861$, $\sigma(A_1) = 0.015$) is obtained for 1 x 10^9 decaying atoms, and 0.6% ($Ave(A_1) = 0.860$, $\sigma(A_1) = 0.005$) for 1 x 10^{10} decaying atoms (Fig. 2.5).

In order to accumulate 1 x 10^{10} decays in a trap during actual data collection, it takes about 90 hours of active running time if 1 x 10^6 atoms can be filled into the trap. This is a reasonable amount of running time that can be obtained at the 88" cyclotron at Lawrence Berkeley Laboratory.

2.1.7 Other Correlation Effects in Beta Decay

In general, the advantages of using laser trapped atoms as a beta decay source are also valuable when this technique is used for studying other beta decay correlation effects, such as electron-neutrino correlation and "the triple correlation" for time-reversal-invariance test.

The electron-neutrino correlation is the angular correlation of the beta momentum and the neutrino momentum. A precise determination of this correlation can be used to test the Standard Model of V-A coupling in weak interaction. In particular, this correlation is sensitive to scalar coupling of charged weak current [AD93]. It can also be used to measure the nuclear form factors of the decaying nucleus. Instead of detecting the invisible neutrino, the correlation is studied by measuring the momentum distribution of the recoil ion. In this case, the parent nuclei need not to be polarized so the atoms trapped in a MOT can be directly used as a beta source. Using trapped atoms as a source can avoid a serious problem in detecting recoil ions, since the energy of a recoil ion is usually so low (about 0.1 keV for ^{21}Na) that even the thinnest wall will stop it. A detailed

description of the theoretical implications and experimental studies of the beta-neutrino correlation can be found in [AD93] and its references.

Testing time reversal invariance by studying the triple correlation between the spin of the parent nucleus, the momentum of the recoil ion and the momentum of the beta particle, $J \cdot (P_e \times P_N)$, can also be improved with trapped atoms as beta source. To search for this effect, the parent nuclei have to be polarized, and the beta particle and the recoil ion are detected in delayed coincidence by counters installed in a plane perpendicular to the spin direction of the parent nuclei [BA77].

2.2 Parity Non-Conservation in Radioactive Atoms

2.2.1 The Atomic PNC Effects

The possibility of detecting weak neutral currents in atomic physics through parity non-conservation (PNC) effects was first proposed by Bouchiat and Bouchiat in 1974 [BO74]. Since then, this tiny effect has been observed on several elements, including cesium [NO88] , bismuth [MA91], lead [ME93] and thallium [PE84]. The result for cesium is the best, reaching a precision of 2%.

This type of effect arises from Z° exchange between an orbital electron and the atomic nucleus [CO83]. The observable can be described by two effective Hamiltonian terms, H_1 and H_2. H_1 describes the coupling between electronic axial vector current and nucleonic vector current; H_2 describes the coupling between electronic vector current and nucleonic axial vector current. H_1 can be formulated as

$$H_1 = \frac{G_F}{2\sqrt{2}} Q_w \gamma^5 \rho(\vec{r}) \quad , \tag{2.11}$$

here G_F is the Fermi coupling constant; $\rho(\vec{r})$ is the nucleon density at the position of the electron; $Q_W = Z(1-4\sin^2\theta_W) - N$ is the weak charge of the nucleus; and θ_W is the Weinberg angle. H_1 is approximately proportional to the number of nucleons. This is due to the fact that nucleons contribute coherently to the vector current of the nucleus.

On the other hand, the axial vector current of the nucleus is only proportional to the spin of the nucleus, so contributions from paired nucleons cancel each other. Comparing with H_1, H_2 is a factor of $Z(1-4\sin^2\theta_W)^{-1}$ less and its effect is too small to be detected with current experimental techniques.

Because of its low energy nature, the observable Q_W is insensitive to the radiative corrections that depend on the unknown masses of the Higgs particle and the top quark, so any deviation of the measured Q_W from the prediction of the Standard Model is likely to indicate new physics instead of uncertainties in the masses of missing particles [ST92]. For this reason, the experiments on cesium have produced improtant results in testing the Standard Model. In a recent analysis [MA90], it is shown that the cesium result contradicts certain technicolor models and improvements on both experimental measurement and theoretical interpretation are called for constraining the physics beyond the Standard Model.

2.2.2 Current Experiments

There have been two different ways to measure the PNC effect. The cesium and thallium results were obtained with the Stark interference method. In the experiments on cesium, an atomic beam crosses a laser beam of resonant frequency in a region with electric and magnetic field. The PNC interaction in the atoms mixes two states of different parity and causes the intensity of the fluorescence to be dependent on a pseudo-scalar $\mathbf{J}\cdot(\mathbf{E}\times\mathbf{B})$, where **J** is the polarization direction of the circularly polarized light. The bismuth and lead results were obtained with the optical rotation method. A linearly polarized light beam of near resonant frequency is sent through a vapor cell and the PNC interaction in the atoms causes the rotation of the polarization direction of the light. In both cases, high atomic density is needed because the light frequency is tuned on resonance of a weak M1 transition in order to enhance the ratio of the PNC signal over the parity conserving signal. For example, in the cesium experiment, an atomic beam provides 1×10^{15} atoms $cm^{-2}\,sec^{-1}$ in the detection region; and in the lead experiment, vapor pressure is raised to higher than 10^{-1} Torr.

The experimental precision has reached 1% on lead, and 2% on cesium and bismuth. However, theoretical interpretation lagged behind on lead and bismuth (about 10% precision), mainly due to the uncertainties in electron wave function. The electron wave functions of alkali elements, like cesium, are easier to calculate since there is only one unpaired electron in the atom. So the result obtained with cesium's only stable isotope,

$$Q_W\left({}^{133}_{55}Cs\right) = -71.04 \pm 1.58(\mathrm{exp}) \pm 0.88(theo) \quad ,$$

remains as the lonely star.

2.2.3 Measuring PNC Effects in Trapped Radioactive Atoms

A number of research groups are pursuing trapping of radioactive Cs isotopes and Fr isotopes to improve the determination of the PNC effects in atoms. Because these atoms are radioactive, there are not enough atoms to employ the conventional methods discussed in the last section. Atom trapping may provide an atom conserving method for doing this kind of experiments.

There are three reasons to measure PNC effects in different Cs isotopes: (1) To reduce the uncertainty in theoretical calculation due to the uncertainty in electron wave function; (2) to observe nuclear spin dependent PNC effect, which is a probe to a new PNC effect, anapole moment in atomic nuclei; (3) the difference in Q_W of different isotopes provides information to test models beyond the Standard Model, e.g. the general technicolor model, from a new dimension.

Because of the Z^3 dependence of PNC effect on nucleus, it is advantageous to choose heavier atoms as the measuring object. Francium, with the similar electron structure as cesium, is a natural candidate. None of the isotopes of Fr is stable, making experiments with trapped atoms an attractive approach.

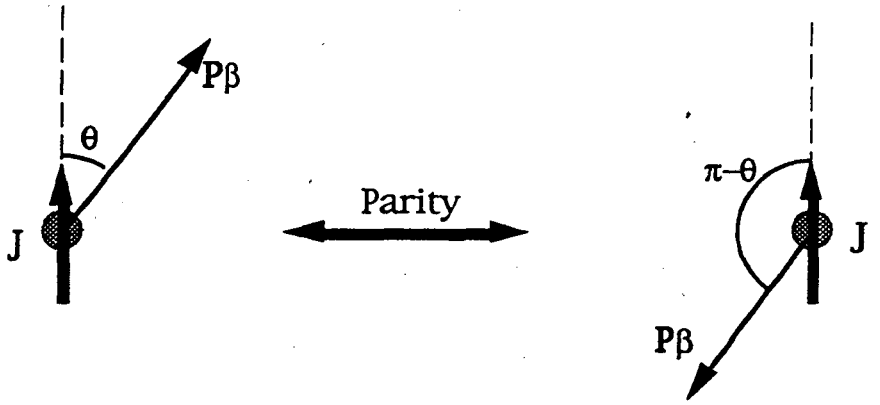

Figure 2.1 Two processes that can be converted to each other under spatial inversion. **J** is the spin of the nucleus, $\mathbf{P}_\beta$ is the momentum of the beta particle.

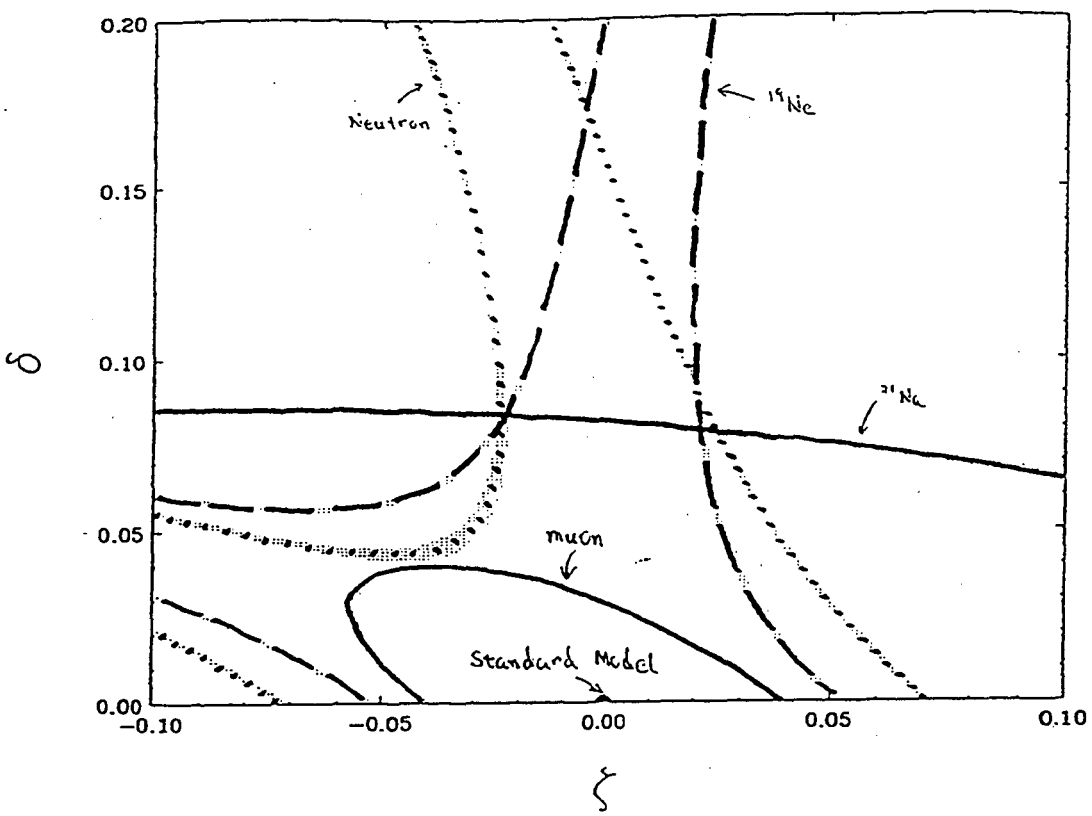

Figure 2.2 Experimental limits of 90% confidence level on the mixing angle and the mass-square ratio of the Left-Right Symmetric Model. The allowed regions are those which include $\delta = 0$, $\zeta = 0$. The limit by ^{21}Na measurements is only expected if the measured beta-asymmetry parameter is A_T=0.781 with a precision of 1%.

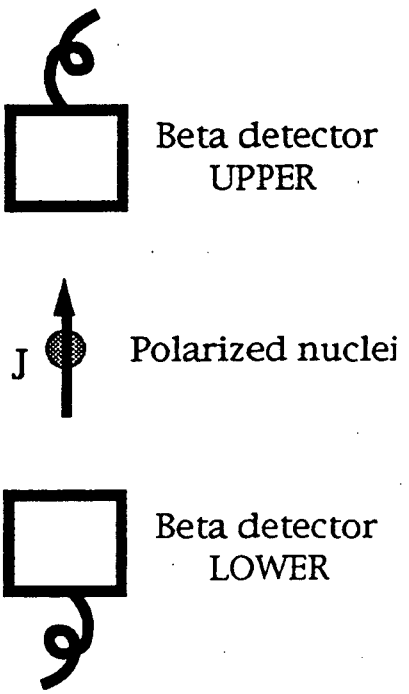

Figure 2.3 A setup for beta-asymmetry measurement.

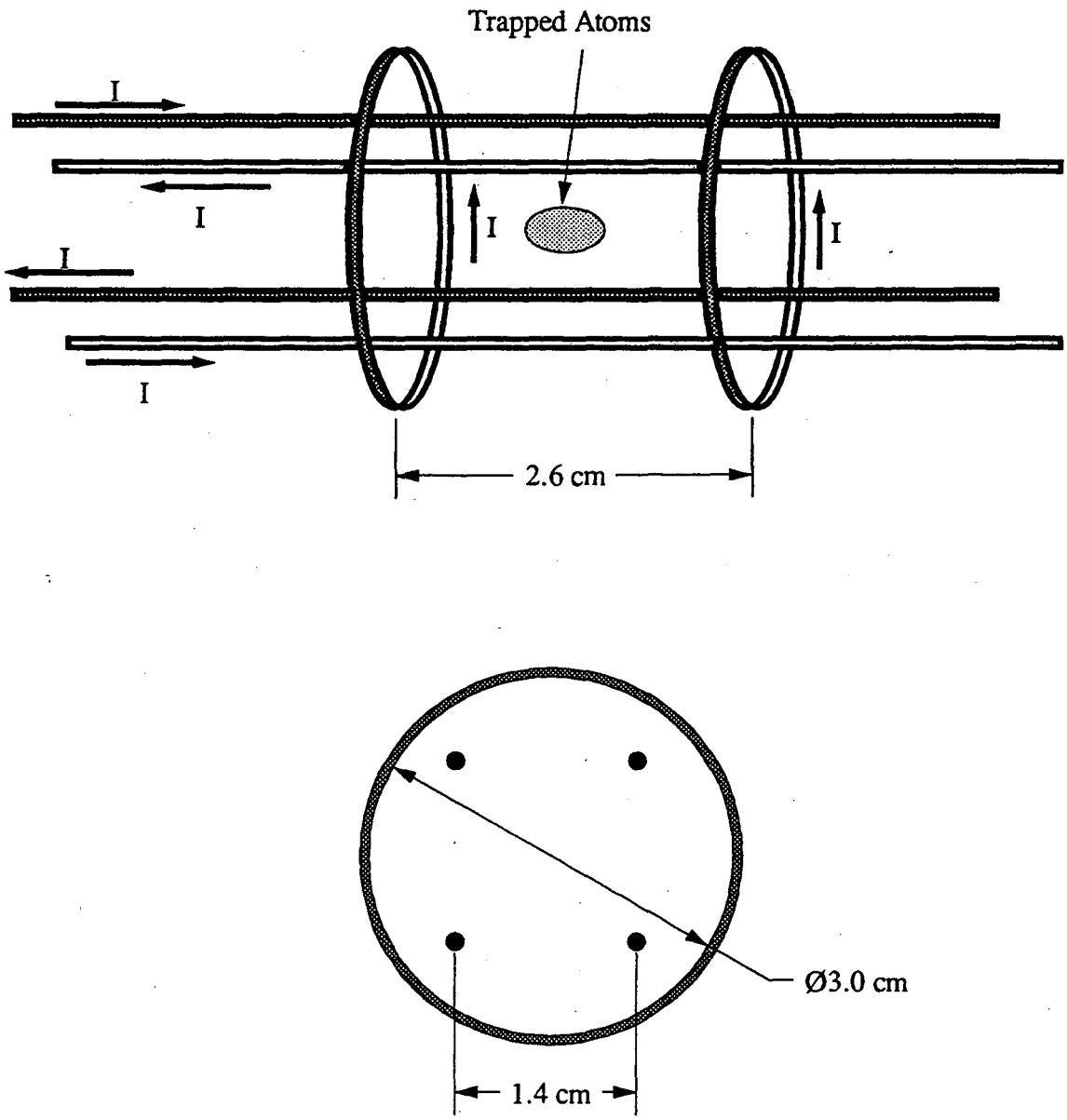

Figure 2.4 An Ioffe trap.

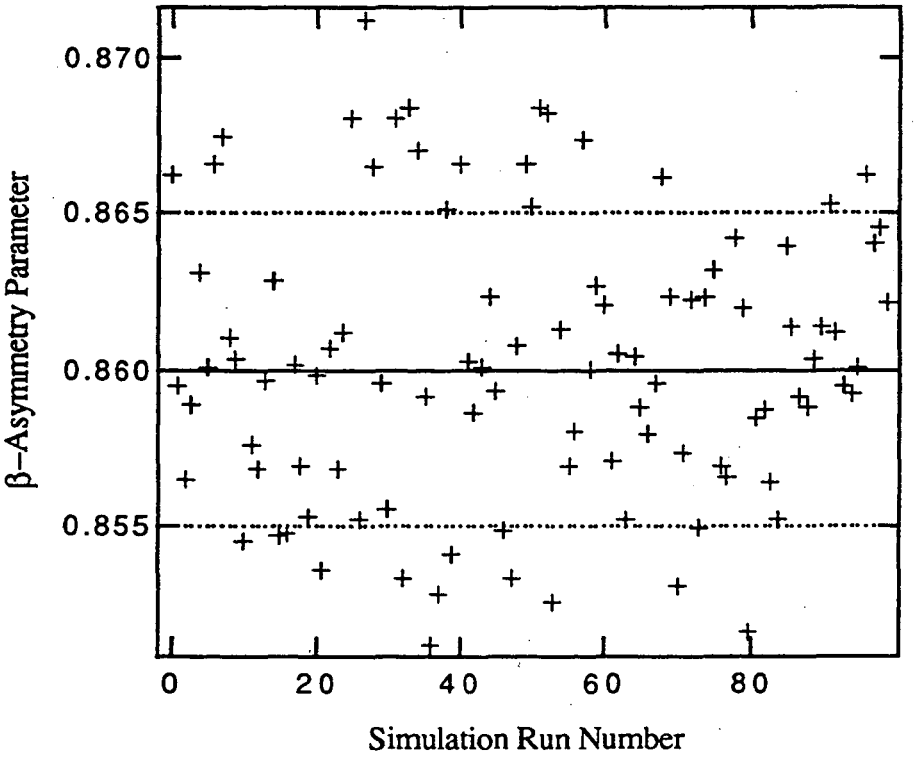

Figure 2.5 The beta-asymmetry parameters obtained from 100 simulation runs. Each cross marker indicates the best fitted value for a simulation run; the solid line indicates the 'true' value (0.860), based on which the raw data are generated; the dotted lines indicate the range of one standard deviation of the sample. It is assumed in each run that 1 x 10^{10} atoms decay in the trap.

Chapter III

Techniques of Laser Manipulation of Neutral Atoms

Introduced in this chapter are three basic techniques of laser manipulation --- transverse cooling, slowing and trapping. Each of them is essential in our experiments of trapping radioactive atoms. Although the examples given here are on ^{23}Na atoms only, these techniques can be applied to many other elements and their isotopes. Detailed description on these subjects can be found in [JO89].

3.1 Light Force on Atoms

When a laser beam is incident to an atom with the laser frequency tuned close to resonance of a transition of the atom, three types of transitions occur: (1) absorption -- an atom in a ground state absorbs a photon, leaving the atom in an excited state; (2) stimulated emission -- an atom in an excited state in a laser field emits a photon in the direction of the laser beam and decays to a ground state; (3) spontaneous emission -- an atom in an excited state interacting with the vacuum fluctuating field emits a photon in random direction and decays to a ground state.

In this geometry, after absorption and then stimulated emission, an atom gains no momentum because the emitted photon is in the same direction of the photon absorbed. On the other hand, an atom can change momentum if it absorbs a photon and decays spontaneously. The momentum change from spontaneous emission is zero on average because the emitted photon direction is random. Averaging over absorption and spontaneous emission cycles, the momentum change by a photon in the laser beam is:

$$\left\langle \Delta \vec{P}_{atom} \right\rangle = \vec{P}_{photon} = \frac{h}{\lambda}\hat{k} \quad , \tag{3.1}$$

where λ is the wavelength and $\hat{k}$ is the direction of the laser light. For example, a sodium atom gets a velocity change of 3 cm/sec from one cycle when the laser wavelength is tuned to D_2 line at 589 nm.

In order to maintain the force, the atomic transition has to be "closed", i.e. the excited atom must decay back to the same ground states from where it can be re-excited by the laser light. A transition that satisfies this requirement is called a "cycling transition". The magnitude of the force on the atom depends on how rapidly the photon absorption and spontaneous emission process is cycled. The mean period for a single cycle is

$$\tau_{cycle} = 2\tau_0\left[1+\frac{I_{sat}}{I}\left(1+4\frac{\Delta^2}{\Gamma^2}\right)\right] \quad , \tag{3.2}$$

where τ_0 is the natural mean lifetime of the excited states; I_{sat}, the "saturation intensity", reflects the transition strength; I is the laser light intensity; Δ is the laser frequency "detuning", $\Delta = \omega_L - \omega_0$, with w_L as the laser frequency and ω_0 as the resonant frequency of the transition; and Γ is the linewidth. A numerical example is listed in Appendix A.

Notice that $\tau_{cycle} \rightarrow 2\tau_0$ for high light intensity. The limit imposes a maximum acceleration that an atom can obtain from light force:

$$a_{max} = \frac{1}{2\tau_0} \cdot \frac{h}{\lambda} \cdot \frac{1}{m} \quad , \tag{3.3}$$

with m being the mass of the atom. For example, if light is tuned to the D_2 line, transition $3S_{1/2}$ F=2 to $3P_{3/2}$ F'=3 (i.e. from the $3S_{1/2}$ F=2 ground state hyperfine level to the $3P_{3/2}$ F'=3 excited state hyperfine level) of ^{23}Na, the maximum acceleration is 9×10^5 m/s^2 !

Although the transition in the last example, "F=2 to F'=3", is the one that is widely used to manipulate sodium atoms, in practice it is effectively an imperfect cycling transition because of the finite linewidth of light-atom interaction. It is possible to excite the atom to the neighboring F'=2 states and then the atom spontaneously decays to F=1 ground states, unaffected by further interactions with the light tuned to the resonance of the transition F=2 to F'=3. Even when the light intensity is low and its frequency is tuned right on resonance ($\Delta = 0$ MHz) of F=2 to F'=3, leaking to F=1 state can still happen after about 300 "good" cycles. To avoid pumping atoms to F=1 states, light with frequency on resonance of transition F=1 to F'=2 is mixed in with the primary light. This second frequency is often called the "sideband" or "repumping" frequency. It is essential in order to provide a continuous force on sodium atoms.

3.2 Transverse Cooling

Let's look at a simple example to demonstrate the light force on atoms. Fig 3.1a shows an atomic beam deflected by crossing a perpendicular laser beam. Atoms can be accelerated

transversely with light frequency tuned on resonance. However the atoms quickly shift away from resonance because of the Doppler shift and the acceleration subsequently stops. For the sodium D2 line, 6 m/s corresponds to a Doppler shift of one natural linewidth (Γ = 10 MHz). The force on a two-level atom with velocity along the light direction is given by the expression:

$$F = \frac{h}{\lambda} \cdot \frac{1}{2\tau_0} \cdot \frac{I}{I + I_{sat}\left[1 + 4\frac{(\Delta - kv)^2}{\Gamma^2}\right]} \quad , \tag{3.4}$$

here v is the velocity along the light direction; and k is the wave-vector of the light beam.

Consider the situation when the light frequency is tuned to 10 MHz below the resonance. The atoms with a transverse velocity pointing against the light propagation direction at 6 m/s are brought into resonance with the light by Doppler shift so they are decelerated by the strong light force; the atoms with no transverse velocity feel weaker force since the light frequency is 10 MHz away from resonance; and the atoms with a transverse velocity moving along with the light feel even less force. As a result, the spread of the transverse velocity distribution of the atoms is reduced, which is called "cooling". The effective "temperature" of an ensemble of atoms is defined as

$$\frac{1}{2}K_B T = \frac{1}{2}m\langle v^2 \rangle \quad . \tag{3.5}$$

Furthermore, the force described by equation (3.4) can be expanded for small kv/Γ and I/I_{sat} as

$$F(v) = F(0) - \alpha v + O\left[(kv/\Gamma)^2\right] \quad , \tag{3.6}$$

$$\text{with} \quad \alpha = 4\frac{\hbar}{\lambda^2}\cdot\frac{(-\Delta)}{\Gamma}\cdot\frac{I/I_{sat}}{\left(1+4\frac{\Delta^2}{\Gamma^2}\right)^2} \quad . \tag{3.7}$$

Notice that when frequency is detuned below resonance, -Δ is positive, so the "damping coefficient" α is also positive. When $\Delta = -\Gamma/2$, a reaches the maximum value

$$\alpha_{max} = \frac{1}{2}\frac{\hbar}{\lambda^2}\frac{I}{I_{sat}} \quad . \tag{3.8}$$

Two counter-propagating laser beams can be used to transversely cool an atomic beam, increasing the on-axis atomic beam intensity (Fig. 3.1b). Figure 3.2 shows the force in the transverse direction as a function of transverse velocity, when the laser beam intensity is $I=I_{sat}$ and the laser frequency is detuned by half of the linewidth, $\Delta = -\Gamma/2$. The damping coefficient in this example is double that of a single beam.

While this cooling mechanism reduces the velocity spread of the atoms, a random diffusion force from the momentum changes following random spontaneous emissions "heat" the atoms. The final temperature reflects an equilibrium between these two competing processes. There is a lower temperature limit for this type of cooling, named the Doppler limit,

$$K_B T_{Doppler} = \frac{1}{2}\hbar\Gamma \quad . \tag{3.9}$$

For sodium, with $\Gamma = 2\pi$ x 10 MHz, the Doppler limit is 240 mK, corresponding to 0.3 m/s of average transverse speed.

3.3 Longitudinal Slowing of an Atomic Beam

Slowing of an atomic beam can be accomplished by sending a laser beam counter-propagating to the atomic beam. The longitudinal velocity of sodium atoms effusing out of an oven follows the Maxwell-Boltzmann distribution. When the oven is at 200°C, the most probable velocity is about 600 m/s, given by $v_p = 1.22\sqrt{2K_BT/M}$. Since each photon kick changes an atom's velocity by 3 cm/s, it takes about 2×10^4 photons to bring the atom to stop. There is an impressively huge deceleration, about 10^6 m/s^2 from the light force. Atoms can be brought from the speed of a jet airplane to rest in a distance of less than one meter.

There is an important practical problem in slowing an atomic beam with laser light. A single frequency laser beam can not stay in resonance with the atoms during the entire deceleration process because there is a corresponding change in the Doppler shift. The photon absorption linewidth $\Gamma\sqrt{1 + I/I_{sat}}$ corresponds to only tens of meters per second of velocity range within which the slowing force is effective. Two standard techniques have been effective to avoid this problem, the "chirping" method and the "Zeeman-tuning" method.

In the chirping method [ER85], the laser frequency is swept to compensate for the changing Doppler shift. At the start of a chirping cycle, the laser frequency is low and in resonance with a group of atoms with a high velocity v_h. As the velocity of this atom group is lowered to v_h-δv, the laser frequency is increased to stay in resonance. Meanwhile, another group of atoms whose original velocity is v_h-δv get in resonance with the light and are decelerated too. After the laser frequency sweeps through a range of velocity, the velocity distribution of the beam is compressed to a narrow velocity space

range. There is an upper limit on the sweeping rate, which is determined by the maximum acceleration that the light can provide,

$$a = \frac{h}{m\lambda} \cdot \frac{1}{\tau_{cycle}} = \frac{a_{max}}{1 + \frac{I_{sat}}{I}} \quad . \tag{3.10}$$

In each cycle, the laser beam decelerates the atoms that satisfy all three conditions: (1) the atoms' original velocity is lower than v_h; (2) the atoms enter the slowing path before the laser frequency is scanned to their resonant frequency; (3) the atoms exit the slowing path after the end of the chirping cycle. The chirping method generates a pulsed slow atomic beam. Atoms with various initial longitudinal velocities are slowed to the same final velocity at the same time but at different locations along the beam trajectory.

In the Zeeman-tuning slowing method [PH82], the laser frequency is fixed while the atomic level is changed by Zeeman shift to compensate for the Doppler shift. The changing magnetic field is generated by a tapered solenoid (Fig 3.3). For the transition F=2, M_F=+2 to F=3, M_F=+3 (and its corresponding state at finite magnetic field), its energy separation

$$E = E_0 + \mu_B B \tag{3.11}$$

increases when the atoms are polarized along the direction of the magnetic field (Fig 3.4), here μ_B=1.4 MHz/Gauss is the Bohr magneton. At any position inside the solenoid, if the velocity of an atom satisfies the resonance condition,

$$kv = \mu_B B \quad , \tag{3.12}$$

it begins to be decelerated by the light, and is continuously decelerated all the way to the end of the solenoid. Similar to the case of the chirping method, there is a maximum magnetic field gradient determined by the maximum deceleration that can be provided by the laser beam,

$$\left(\frac{\mu_B}{k}\right)^2 \cdot B\left(\frac{dB}{dZ}\right)_{max} = \frac{a_{max}}{1+\frac{I_{sat}}{I}} \qquad (3.13)$$

The maximum field strength at the high end determines a cutoff velocity, above which the atoms are not affected by the laser beam. Below this cutoff velocity, atoms with various initial longitudinal velocities are slowed to the same final velocity at the same place. The resulting slow beam is continuous.

In a situation when slow atoms are loaded into a trap, it is advantageous to slow atoms to a final velocity at a single place where the trap can be set up. In the chirping method, atoms are slowed to a final velocity at different places along the beam trajectory. When a trap is set up at the end of the beamline, slowed atoms have to drift into the trap at a small longitudinal velocity. Only a small fraction of them can cross the trapping area due to beam divergence. So the Zeeman-tuning method can provide more slow atoms to a trap than the chirping method, but the stray magnetic field at the end of the solenoid can be a problem for many experiments.

3.4 The Magneto-Optical Trap

A description of a magneto-optical trap (MOT) with a numerical example was already given in Section 1.2. Figure 3.5 is the usual diagram used to explain the MOT. It shows a one dimensional trap. The simple atom has two levels, a J=0 ground level and a J=1 excited level. A weak inhomogeneous magnetic field is applied. The magnitude of the field is zero at the origin, increasing linearly with distance from the center. The magnetic field direction is along the z-axis and points oppositely for plus and minus z. As a result of the Zeeman effect, the excited level splits into three energy levels. Two laser beams, with different circular polarization, are directed oppositely along the z-axis. The frequency is detuned below the zero field resonant frequency.

Consider an atom at $-z_0$. The energy level of the state J=1, m_j=+1 is shifted down, so the transition (J=0, m_j=0) to (1,+1) is in resonance with the laser frequency. The transition (0,0) to (1,-1) is shifted out of resonance. As a result, the atom absorbs σ+ light more strongly than it absorbs σ- light, and the atom gets pushed toward the origin by the σ+ light. For an atom at $+z_0$, σ- light is favored and the force is again toward the origin. Thus the arrangement can act as an atom trap. For an atom at the origin, the excited states are degenerate and not shifted so the light force from the two beams cancel. However, since the laser frequency is detuned below the resonance, the light continues to cool the atoms that are trapped. Laser cooling provides the stability that is essential to this process.

This one dimensional model can be generalized to 3-D as illustrated in Figure 1.1.

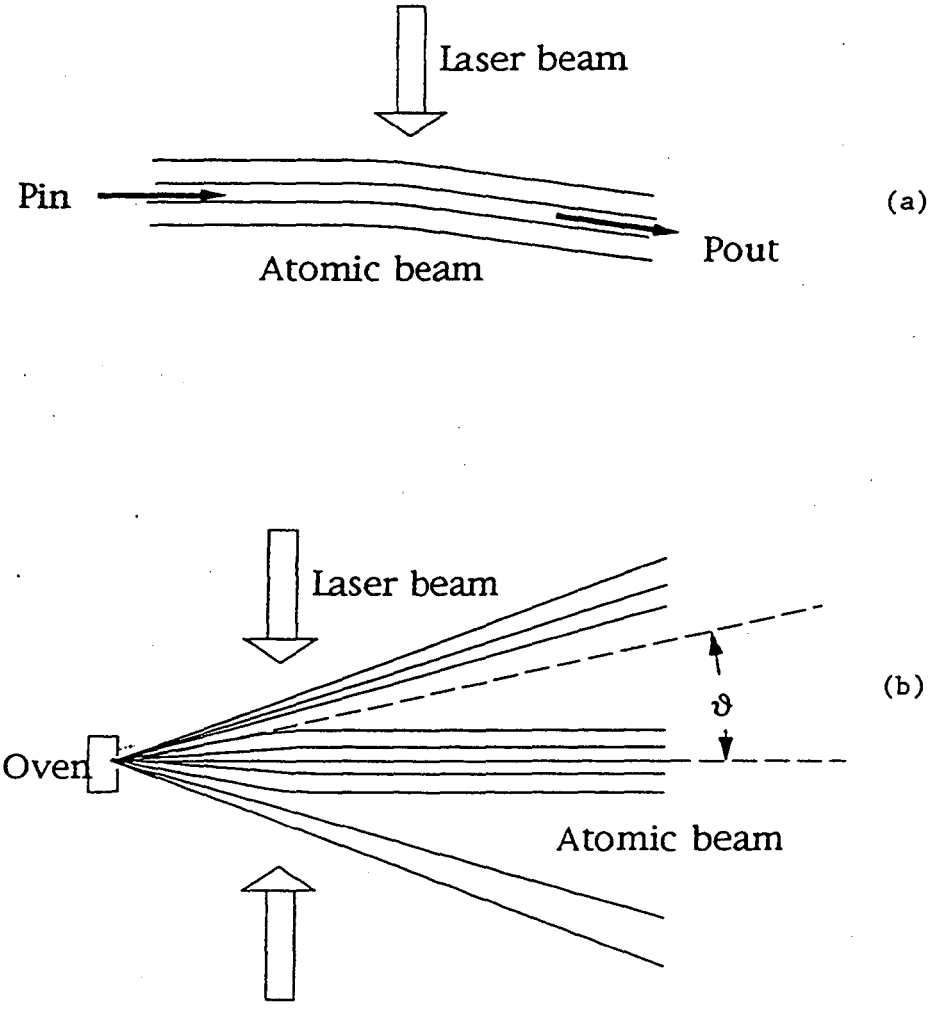

Figure 3.1 (a) Bending an atomic beam with light force; (b) Transverse cooling. The on-axis atomic beam intensity is increased. Only those atoms with transverse velocity within the capture velocity range are cooled.

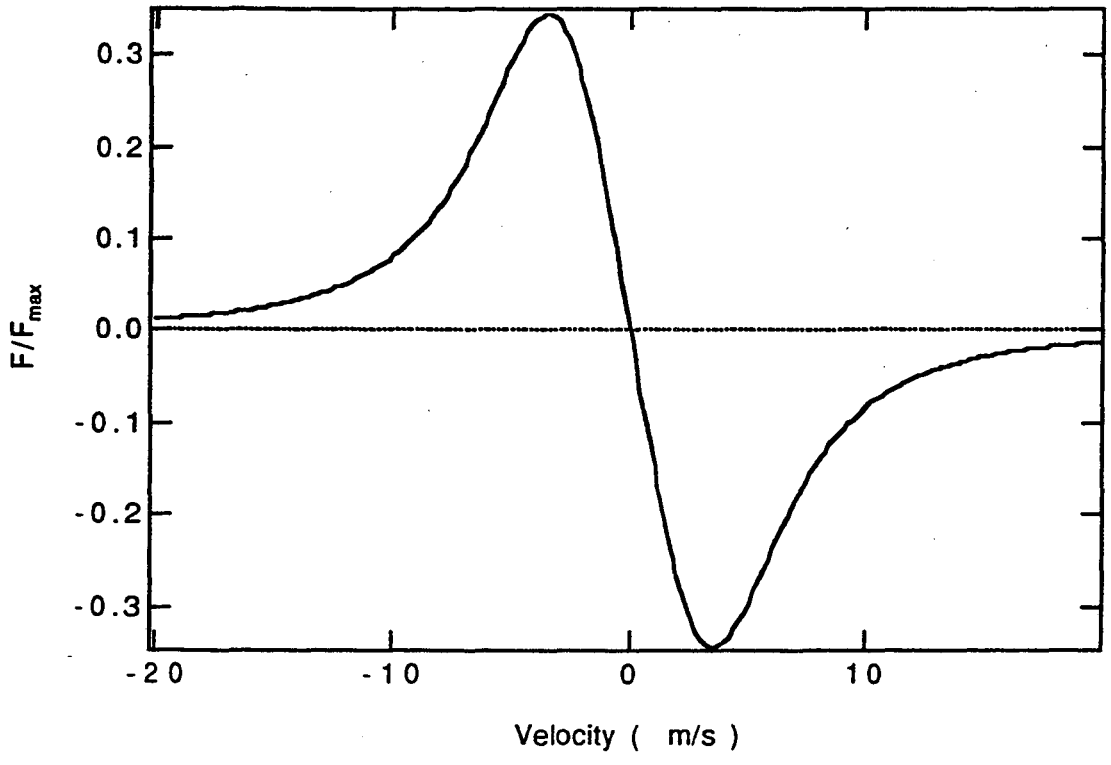

Figure 3.2 The transverse cooling force applied by a pair of counter-propagating laser beam (Fig. 3.1b). For each beam, $I = I_{sat}$, $\Delta = -\Gamma/2$, $F_{max} = \frac{h}{\lambda} \cdot \frac{1}{2\tau_0}$.

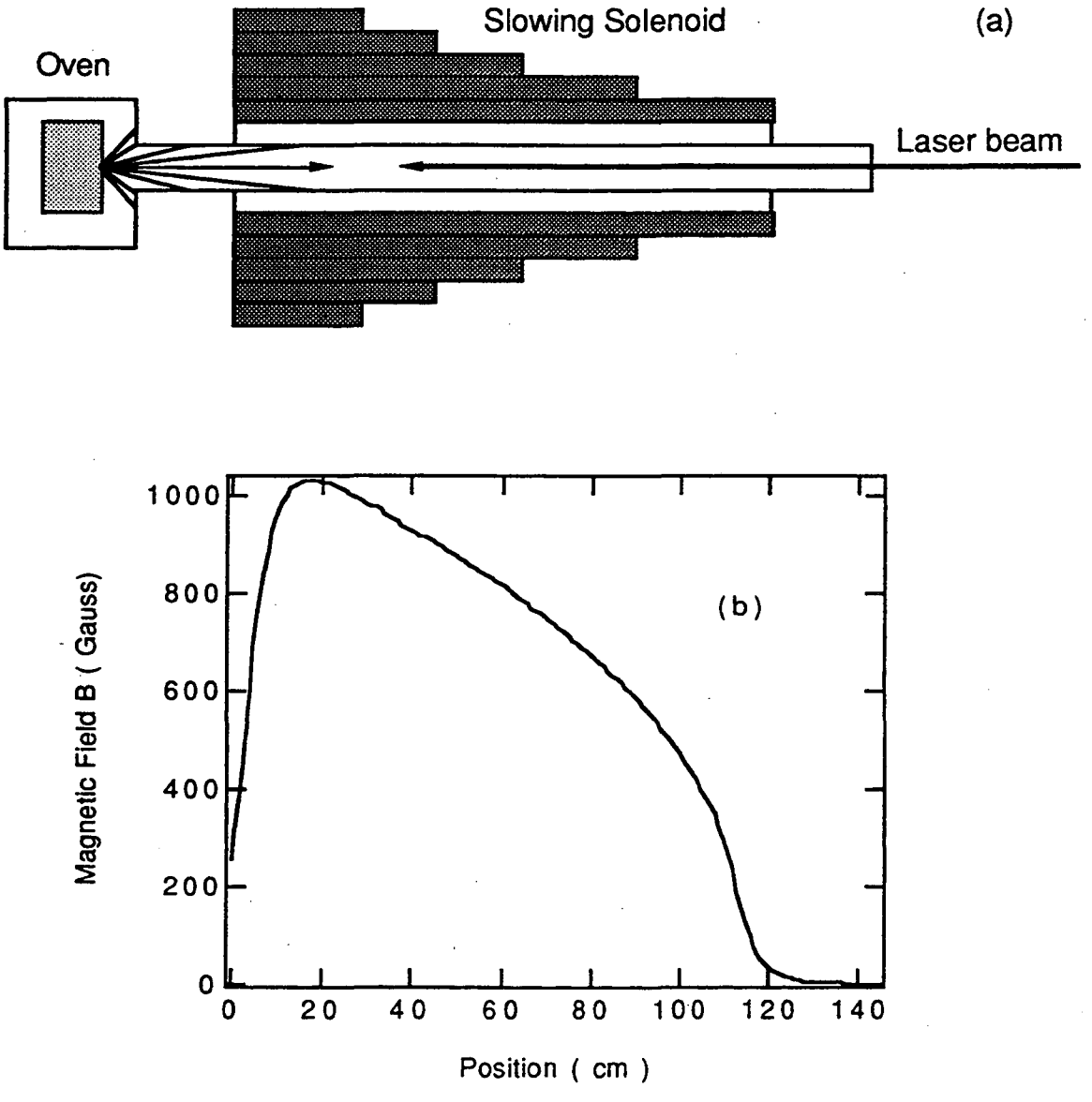

Figure 3.3 (a) Zeeman-tuning slowing method. A cross-section of the slowing solenoid is shown. (b) The longitudinal magnetic field strength along the slowing path. The maximum field strength is 1030 Gauss. Sodium atoms with velocity lower than 850 m/s are slowed.

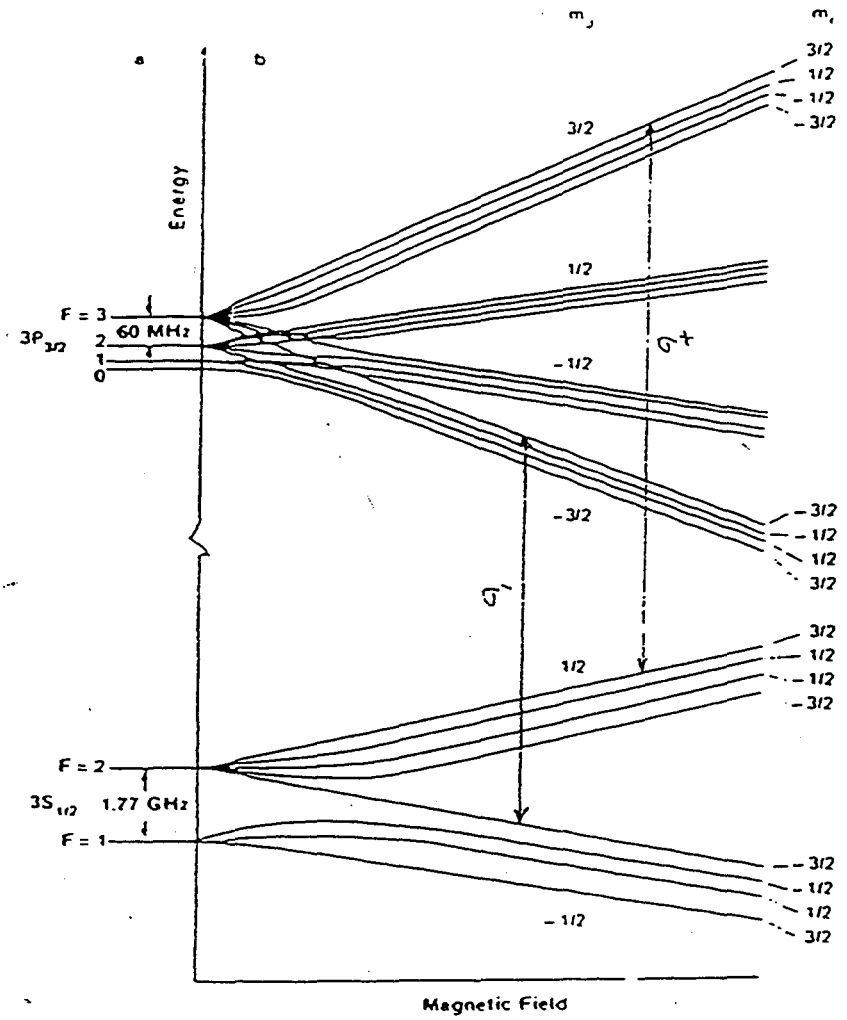

Figure 3.4 The energy levels of Na in magnetic field. The conventional Zeeman-tuning method uses the σ+ transition marked in the diagram. The reversed field Zeeman-tuning method, to be discussed in Section 4.3, uses the σ- transition.

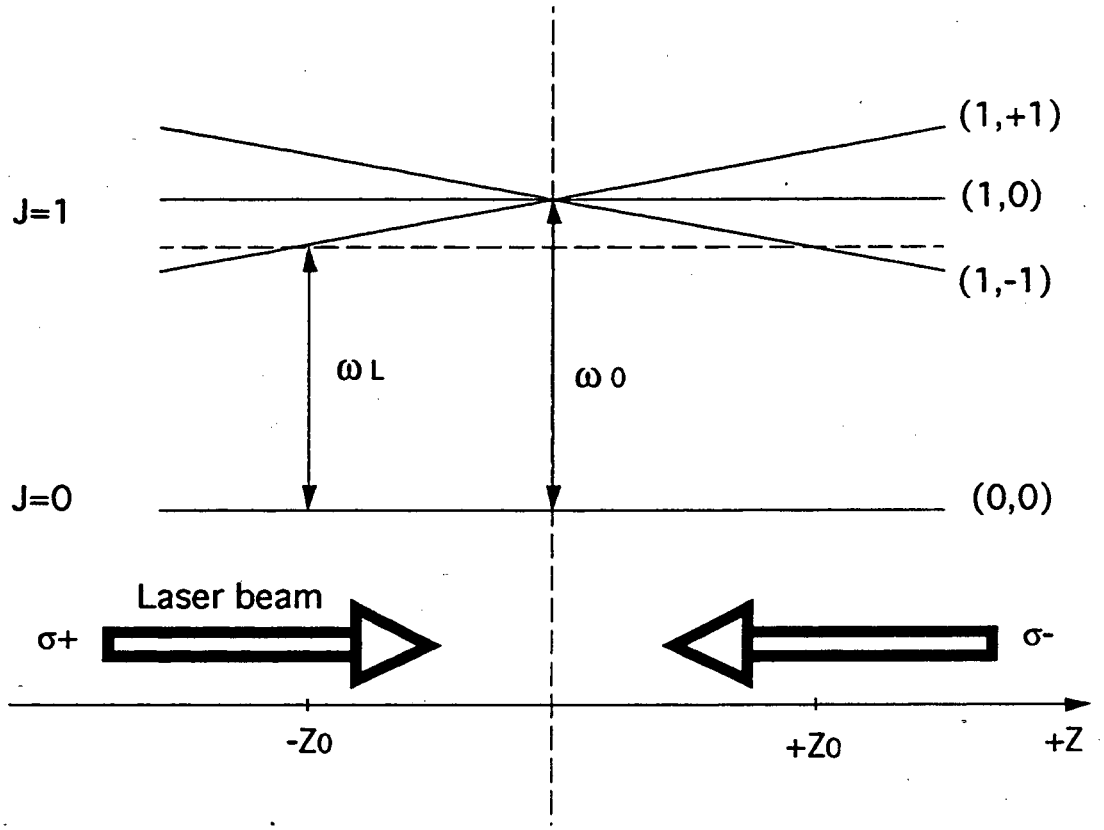

Figure 3.5 An illustration of the magneto-optical trap in one dimension. The excited states are split due to the Zeeman shift in the in-homogeneous magnetic field. ω_L is the laser frequency, ω_0 is the resonant frequency of the transition at z=0.

Chapter IV

Various Trap Loading Schemes

As mentioned in Section 1.3, the principal challenge associated with trapping short-lived radioactive atoms is the short supply of these atoms. Developing efficient methods for loading atom traps is critical. Here I'll survey a number of established and developing techniques for improving the loading efficiency of magneto-optical traps.

4.1 Loading a MOT with atomic vapor

One approach is to load from atomic vapor. A demonstration of this technique with stable cesium atoms was reported recently [ST94].

In this method, a MOT is formed inside a closed volume that contains low density vapor of the atoms which one desires to trap. In such a cell, atoms follow the Maxwell-Boltzmann velocity distribution,

$$\frac{dN}{dv} \propto v^2 \exp\left(-v^2/v_p^2\right) \quad . \tag{4.1}$$

Here v is the velocity of atoms and v_p is the most probable velocity in a volume of gas. v_p can be calculated as $v_p = \sqrt{2k_BT/m}$. Here k_B is the Boltzmann constant, T is the temperature and m is the mass of the atom. At room temperature for cesium atoms, v_p = 190m/s. Because of the finite trap region and Doppler effect, only those atoms with low enough velocity ($v<v_c$) in the tail of the Maxwell-Boltzmann distribution are collected into the trap. Here v_c, called capture velocity, typically ranges from 10 m/s to 30 m/s, depending on the parameters of a specific MOT (see Section 9.4). The supply of low velocity atoms is replenished by velocity redistribution through collisions with cell walls. However, thermalization by wall collisions is problematic because atoms that strike the walls have a finite sticking time. In a cell with stable atoms, all surfaces are coated by atoms and a constant vapor pressure is maintained at equilibrium by adsorption and desorption of atoms from the walls. This condition does not hold at the typically low density of short lived radioactive atoms, because the supply is limited and stable vapor pressure is never achieved. In order to avoid losing atoms to the walls, a special layer of material is coated onto the walls to reduce the sticking time.

In the demonstration done with stable Cs atoms [ST94], a Pyrex glass cell was coated with a layer of a silicon-based hydrocarbon polymer, octadecyltrichlorosilane, which reduced the sticking time from 2 msec on uncoated walls to 4 m sec with coating. Furthermore, in order to increase the trap loading speed, a Ti:Sa laser was used to provide three retro-reflected high power laser beams, 1.8 cm in diameter and 40 mW/cm^2 in intensity which is 15 times the saturation intensity for the D2 $6S_{1/2}$, F=4 to $6P_{3/2}$, F=5 transition.

The measurement of trap loading efficiency involves a simple sequence: Initially, the cell is filled with cesium vapor and 10^9 atoms are trapped in the MOT inside the cell; then the cesium source is valved off and the background vapor is pumped away; next, the cell is

completely sealed and the 10^9 trapped atoms are released by blocking the trapping laser beams; after 150 msec, atoms are completely thermalized at room temperature after bumping into walls for about 500 times, and the MOT is turned back on and the number of atoms recaptured is measured. Another sequence is played for background check, in which case the initial loading of 10^9 atoms into the MOT is skipped and the effects on recapture from background cesium atoms is examined. After background subtraction, the experimenters reported [ST94] that a maximum of 6% of the initially released 10^9 atoms are recaptured after 0.9 sec of loading. The cell was completely sealed during the loading period to prevent losing atoms to other regions. This caused the background pressure to rise and limited the loading time.

4.2 Trap Loading with a Slow Atomic Beam

One way to avoid the complications associated with sticking probabilities is to load directly from an atomic beam. Unlike in a cell, here atoms are not recycled and the atoms in the beam pass the trap region only once. Because the capture velocity (see section 4.1) of a MOT is usually below 30 m/s, the atoms in a thermal beam must be slowed before they can be efficiently loaded into the MOT.

Both chirping and Zeeman-tuning slowing (see section 3.3) have shortcomings in producing atoms slow enough to be loaded into a MOT. Zeeman-tuning slowing can produce a continuous beam of slow atoms within the Zeeman tuning solenoid, but as the magnetic field drops to zero at the end of the solenoid, atoms tend to stop at that point and be pushed back by the slowing laser beam. The extraction of slow atoms from the solenoid is extremely inefficient at the low speed required for trapping [PR85].

This difficulty is caused by the fact that the laser light does not simply decelerate those atoms with the correct Doppler shift. Because of the finite frequency width $\Gamma\sqrt{1+I/I_{sat}}$ in the atom-light interaction, off resonance atoms are also decelerated. This problem is more serious when a low speed atomic beam is desired for two reasons: (1) it takes a longer time for a slower atom to travel from the end of the slowing solenoid to the trap where there is a higher probability of off-resonance scattering along the way; (2) a small deceleration for a higher speed atom has less effect.

A slow atomic beam also diverges faster. In the case of sodium atoms being slowed down from 1000 m/s, each atom scatters about 3×10^4 photons. Although the initial transverse velocity can be cooled down to 1 m/s by transverse cooling (see section 3.2), the transverse velocity caused by random scattering of photons during the slowing process builds up to about 5 m/s, which can cause significant atomic beam divergence when the longitudinal velocity of atoms is reduced to a comparable level.

In early efforts of producing a slow sodium atomic beam [PR82, PR85], the slowing laser beam had to be shut off momentarily to allow the slow atoms to drift out of the solenoid. In this way, the experimenters were able to obtain a slow atomic beam of 40 m/s with a flux of 4×10^8 $cm^{-2}sec^{-1}$, about 2×10^{-5} times of the original atomic beam.

In the next two sections we discuss alternative methods to solve this technical problem.

4.3 Reversed Field Zeeman Tuning Slowing

One approach adopted in reference [BA91] is to reverse the gradient in the slowing magnet. Here atoms move the slowest at the high field end of the solenoid. With the

magnetic field direction as the quantization axis, σ- polarized light is appropriate for slowing.

With sodium atoms, the laser frequency is detuned from the resonance of F=2, M_F=-2 to F'=3, $M_{F'}$=-3 at the maximum magnetic field point. As shown in Fig 3.4, the energy separation between F=2, M_F=-2 to F'=3, $M_{F'}$=-3 decreases as the field increases, because of the Zeeman effect compensating for the changing Doppler shift as atoms slow down. The mechanism is similar to σ+ slowing except for the effected Zeeman level. However, the atoms wind up with low velocity in a high field region. Because the magnetic field decreases abruptly at the end of the solenoid, the atoms fall out of resonance quickly. The large Zeeman shifts make the off-resonance scattering negligible.

There is a technical problem when this technique is applied to load a MOT. A sodium atom slowed from thermal speed scatters about 30,000 photons and gains about 5 m/s in transverse direction. This causes atomic beam diverging, especially for the slow atomic beam. Because of the high magnetic field (about 0.1T) at the end of the solenoid, the MOT has to be placed at least 20 cm away from the end. In order to load a MOT, the atoms have to be slower than the capture velocity (see section 4.1), typically 20 m/s, which allows only 1% of the slowed atoms to enter a cross-section of 1 cm^2 at the trap center

In an experiment [BA91] with rubidium, an atomic beam of 40 m/s with a flux of 2 x 10^{10} $cm^{-2}sec^{-1}$ was obtained using this technique. Although the original atomic beam intensity in this experiment was not measured, the slow atomic beam intensity is 50 times as much as that discussed in Section 4.2 for a decreasing solenoidal field.

4.4 Addition of an Extraction Coil

It was first demonstrated [SH89] by Fujio Shimizu et al. that there is an advantage in setting up a MOT at the end of a decreasing field Zeeman tuning solenoid. A bucking coil combined with the solenoid field provides the quadrupole field for a MOT (Fig 4.1).

By combining the slowing gradient field with the trap quadrupole field the effect of atomic beam divergence is reduced. When slowing a sodium atomic beam, the light frequency is tuned in resonance with D2 line $3S_{1/2}$ F=2 M_F=+2 to $3P_{3/2}$ F'=3 M_F=+3 transition and the light at saturation intensity (6 mW/cm^2, see section 3.1) can stop a sodium atom from initial speed of 50 m/s in about 2 mm. This stopping distance can also be limited by the magnetic field gradient. For a gradient of 20 Gauss/cm, this stopping distance is about 3 cm, which is still short enough to avoid much of the atomic beam divergence. Furthermore as an atom is slowed down and about to be turned around by the slowing laser beam, it enters the trapping region and the trapping laser beams hold it in the trap. Shimizu used a four-beam trap, with the slowing laser beam as one of the four (see figure 4.1). In practice, it is difficult to bring the big tapered solenoid close to a trapping chamber, but a uniform field solenoid (so called 'extraction coil', see figure 4.1), positioned between the big tapered solenoid and the trap, is used to provide the final stage of slowing.

This technique was employed by Shimizu et. al. [SH90] to trap meta-stable neon atoms. However, the loading efficiency, defined as the ratio of the number of the atoms that are loaded into the trap to the number of the atoms that reach the trap region, was not measured in their experiments.

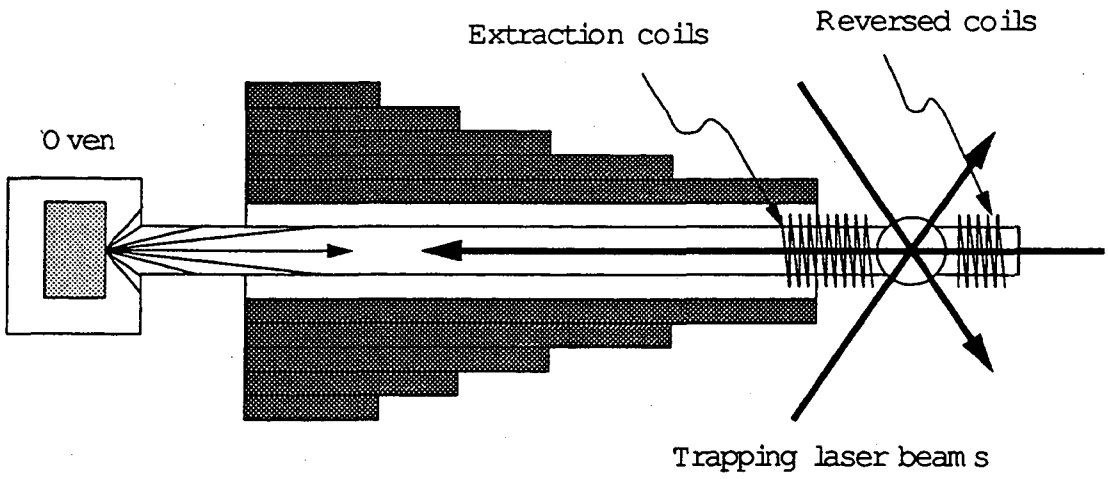

Figure 4.1 A MOT at the end of the slowing path.

Chapter V

Laser System for a Simple Magneto-Optical Trap

5.1 Lasers

Our light source is a Coherent 899-21 dye laser pumped by a Coherent Innova-300 Argon ion laser. With 6W of pumping light, the dye laser can output about 800 mW of light at wavelength 589 nm and with a frequency width of 1 MHz.

During single mode operation, the laser frequency is locked to a temperature stabilized Fabrey-Perot interferometer. However, the variation of room temperature and room pressure still causes frequency drift because the spacing between the mirrors of the FP interferometer is affected. The drift rate varies over a wide range depending on how "well" the dye laser is tuned; 2 MHz/100 sec is typical.

When properly tuned in TEM00 spatial mode , the dye laser produces a 1 mm diameter beam with a divergence of 1.2 mrad.

5.2 Saturation Spectroscopy

For a magneto-optical trap, the laser frequency must be detuned a few linewidths from the trapping transition. In the case of ^{23}Na trapped with the F=2 to F'=3 transition of D_2 line, the transition linewidth is 10 MHz, and the laser frequency must be within the range of 5 - 25 MHz detuned below resonance. In order to obtain stable experimental results, the laser frequency must be stabilized within a few MHz. Typically, the natural linewidth of an E1 transition is around 10 MHz, but an ordinary absorption spectrum (figure 5.1(b)) shows a Doppler broadened peak with a linewidth of about 1 GHz. In order to meet the laser frequency locking requirements, a Doppler free resonance absorption signal is used as a feedback for adjusting and locking the laser frequency. A standard method of saturation spectroscopy is used in our experiments to provide this feedback.

Figure 5.1(a) shows the basic setup for saturation spectroscopy. Two counter-propagating laser beams, a "signal" and a "pump" beam, pass through an absorption cell filled with atomic vapor. The absorption of the signal beam is monitored. Since the two beams are counter-propagating, assuming the signal and pump laser have the same frequency, each interacts with its own velocity group of atoms that have the corresponding Doppler shift when the laser frequency is off resonance. However, when the laser frequency is on resonance, these two velocity groups of atoms overlap, and the pump beam pumps a fraction of atoms in this velocity group out of the ground level, causing less absorption from the signal beam. Therefore, the saturation spectrum (figure 5.1(c)) shows a narrow "dip" on resonance above the Doppler broadened background signal. The linewidth of the dip is close to the natural linewidth. In practice, the background signal can be eliminated by using techniques of either AM modulation in which case the pump beam is chopped, or FM modulation in which case the laser frequency is modulated. In a saturation spectrum of multi-transitions, there is an

additional cross peak for every pair of resonance peaks. The cross peak is located in between the pair with equal distance to each. A detailed description of saturation spectroscopy along with other marvelous spectroscopic techniques can be found in reference [CO77].

In our setup (see Figure 5.2), the absorption cell is filled with ^{23}Na atoms and heated to about 140°C. To make the absorption cell, first a Pyrex glass cell attached with a sealed sodium ampoule is pumped down to about 1 x 10^{-6} Torr. This step gets rid of air that can react with sodium. Then the ampoule seal is broken and sodium can be 'chased' into the cell by heating along its path. Then the argon gas in the ampoule is then pumped away to avoid pressure broadening. Finally, the cell is pulled off.

A signal beam of 30 mW and a counter-propagating pump beam of 100 μW traverse the cell. The beams are 1 mm in diameter. The total intensity of the two beams should be less than the saturation intensity to reduce power broadening. The saturation intensity is 13 mW/cm^2 for the transition of F=2 to F'=3 of the D2 line.

5.3 Laser Frequency Locking

We lock the laser frequency with a "frequency modulation locking" technique. In order to modulate the laser frequency, a laser beam passes through a TeO_2 crystal in an AOM (acousto-optic modulator), the beam is bounced off a grating formed by a traveling acoustic wave in the crystal and the laser frequency is Doppler shifted by an amount equal to the frequency of the acoustic wave. Figure 5.3 shows the flow diagram of the FM locking.

First, a sine wave signal is sent to the analog frequency control of the AOM, which modulates the output laser frequency with an amplitude of 1 MHz. The same sine wave is also sent to a lock-in amplifier as a reference signal.

Second, the oscillating saturation absorption signal is sent into the lock-in amplifier for de-modulation. The output signal of the lock-in amplifier shown in Figure 5.4 is the first-order derivative of the absorption signal. With the correct polarity, the locking output signal is negative when the laser frequency is detuned to the high frequency side of a resonance peak and positive when detuned to the lower side.

The output signal from the lock-in amplifier is sent into the EXTERNAL SCAN input on the dye laser controller. The laser frequency tracks this input, moving up when the input is positive and down when negative.

This simple feedback loop reduces the frequency drift from 2 MHz/100 sec to 0.2 MHz/100 sec.

5.4 Laser Table Layout

Figure 5.5 shows the arrangements of various optical components on the laser table for our experiments.

1) The dye laser produces about 800 mW of light, with vertical linear polarization.

2) A Fresnel beam sampler removes a reference laser beam of about 10 mW from the main laser beam. This reference beam is used for frequency locking as described above.

3) The main beam passes through an EOM (electro-optic modulator), where a fraction of the light is shifted by about 1.7 GHz. The ratio of the intensities of light on a sideband to carrier is kept at 1:4. The central component of the EOM is a 1 mm x 1 mm x 25 mm $LiTaO_3$ crystal rod. Its two end surfaces (1 x 1 mm) are coated with anti-reflection films. An oscillating electric field in the transverse direction modulates the index of refraction of the crystal, which generates phase modulation on the laser beam passing through the crystal along the longitudinal axis. The resulting wave-function can be written as

$$\begin{aligned} E(t) &= E_0 \sin(\omega_0 t + \eta \cdot \sin\omega_m t) \\ &= E_0 \sum_{-\infty}^{\infty} J_n(\eta) \cdot \sin(\omega_0 + n\omega_m)t \end{aligned} \quad , \tag{5.1}$$

where ω_0 is the laser frequency before entering the crystal, ω_m is the modulation frequency, J_n are Bessel functions, and η is a coupling coefficient determined by the laser frequency, properties of the crystal and the electric field strength. In practice, sizable power can be distributed to 1st and 2nd order sidebands only. The design of this kind of EOM is described in detail in reference [KE87].

4) After the EOM, another reference beam (about 10 mW) is picked out and fed into a wavemeter and a spectrum analyzer. The wavemeter we use is Wavemeter Jr. made by Burleigh Instruments. Its accuracy is 1 part in 10,000 and precision is 1 part in 100,000. It is used for finding the Na D_2 Line. The spectrum analyzer displays the frequency spectrum of the laser light. It also monitors the laser frequency mode and power distribution on the sidebands.

5) The main laser beam goes through a telescope which expands the 1-2 mm diameter beam to 1 cm diameter. At the focal point between two convex lenses of the telescope, a 10 μm diameter pin-hole cleans up the spatial modes of the laser. The output laser beam has a Gaussian intensity profile with 1 cm $1/e^2$ diameter. In later stages of our experiments we use even bigger beams obtained with a second telescope which expand up to 3 cm diameter.

6) To this point the laser light remains vertically polarized. Finally it is split into three beams of equal power, and sent to the trapping area next to the laser table.

5.5 Laser Beam Setup for a Magneto-Optical Trap (MOT)

A three dimensional MOT requires at least four trapping beams [SH91], but the six-beam version is easier to configure and has better stability. A six beam trap consists of three orthogonal pairs. Before entering the vacuum chamber through optical windows, each beam passes through a quarter-wave plate converting linearly polarized light into circularly polarized light. The axis of the quarter-wave plates are adjusted to ensure the proper circular polarization required for a MOT (see section 3.4). Each beam is retro-reflected and the circular polarization is reversed with another quarter-waveplate, providing the remaining three beams required for the MOT.

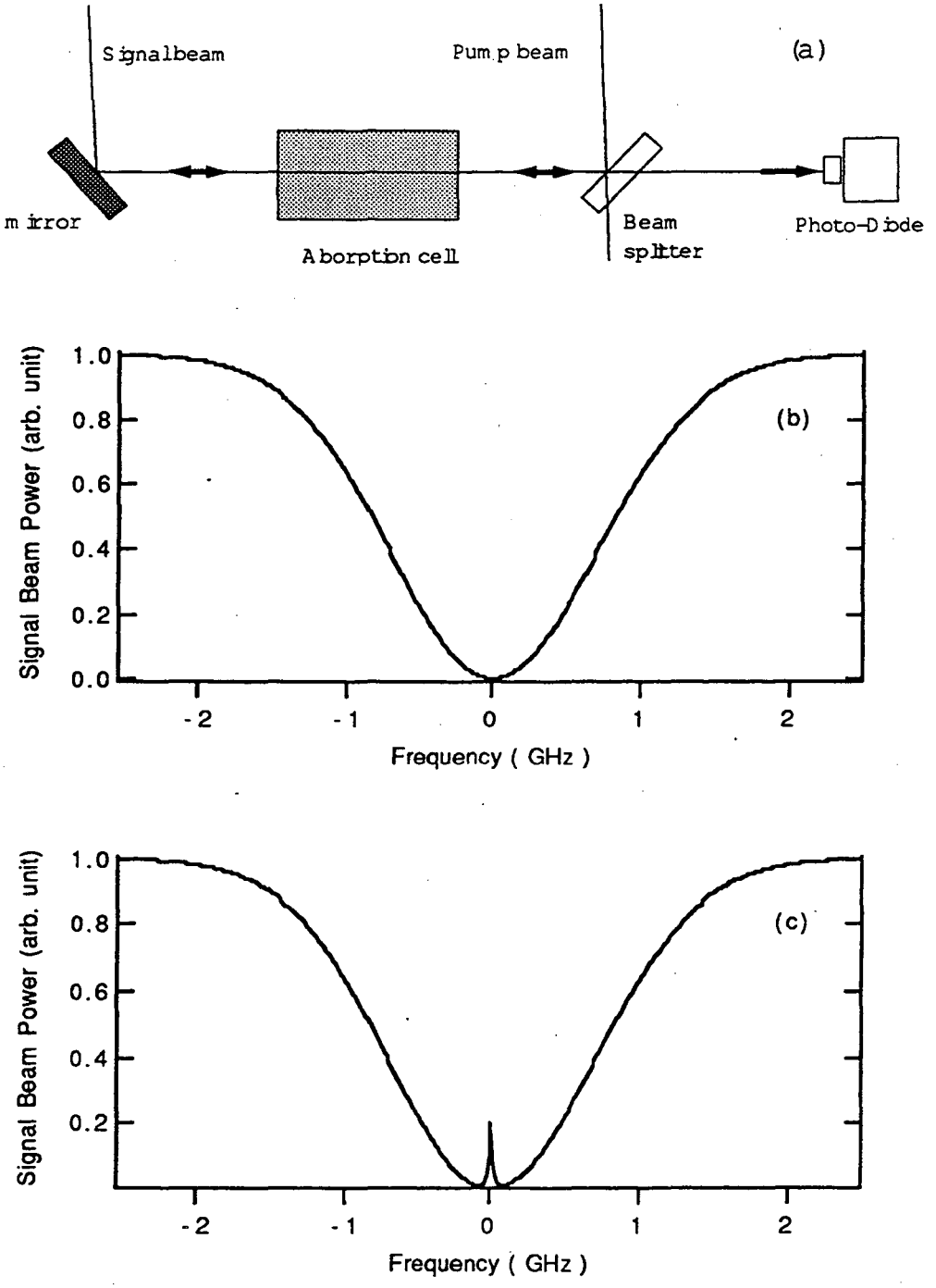

Figure 5.1 (a) Basic setup for saturation spectroscopy; (b) an ordinary absorption spectrum shows a Doppler broadened absorption peak; (c) a saturation spectrum shows a narrow dip on resonance.

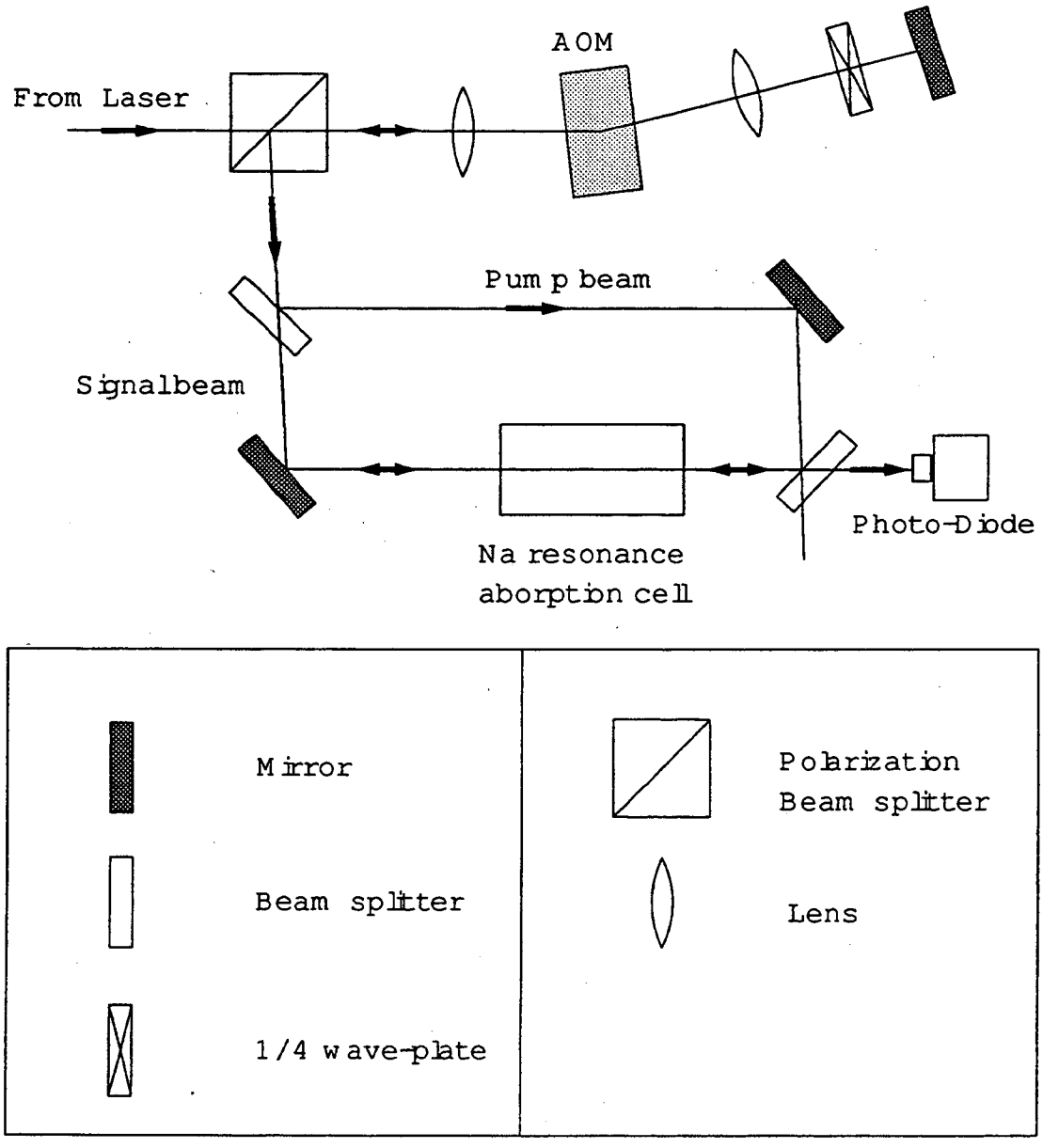

Figure 5.2 Arrangement of saturation spectroscopy feedback. The laser beam passes through the AOM twice to improve the laser beam pointing stability during the frequency modulation.

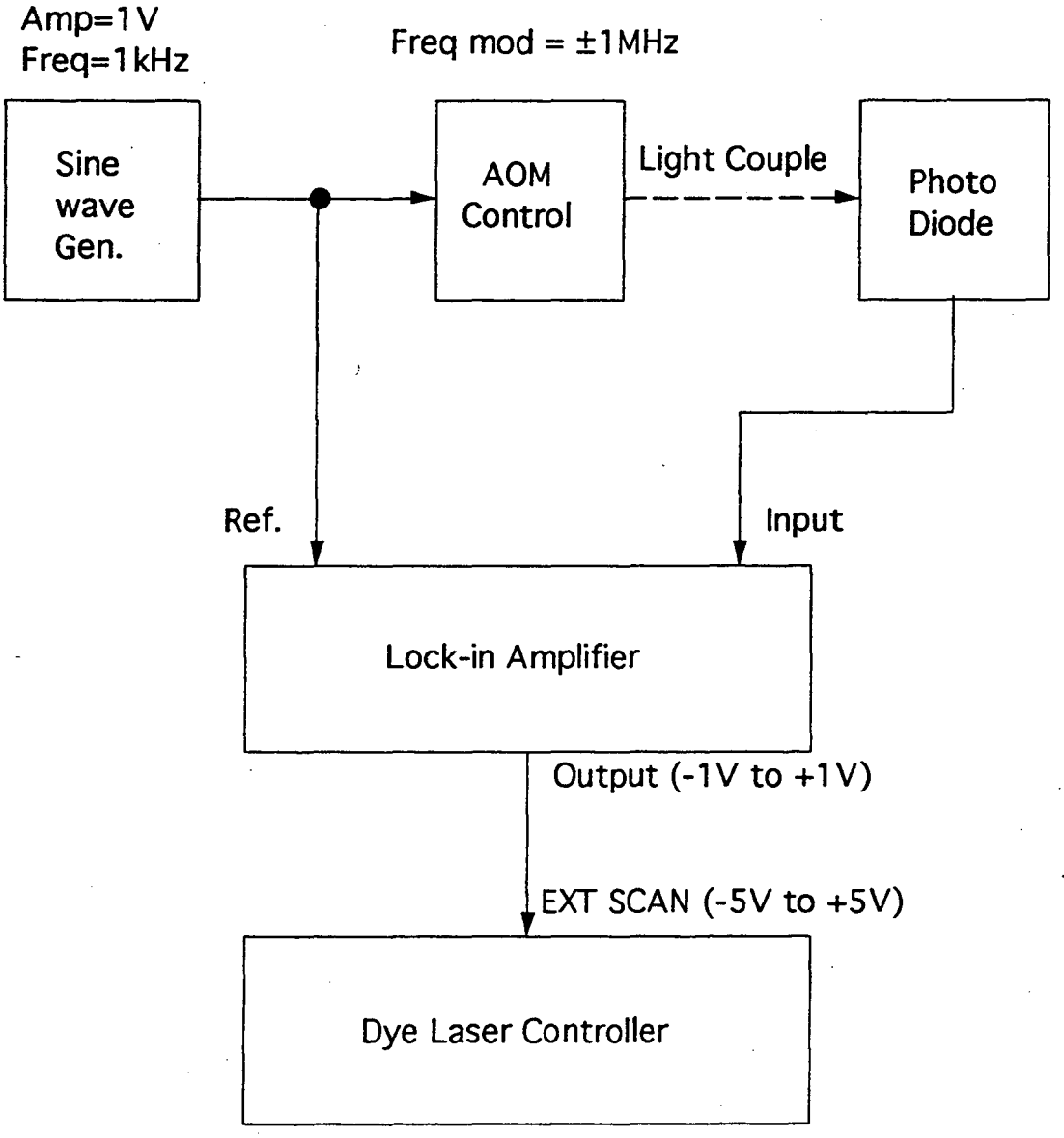

Figure 5.3 Flow chart of the FM locking for the laser.

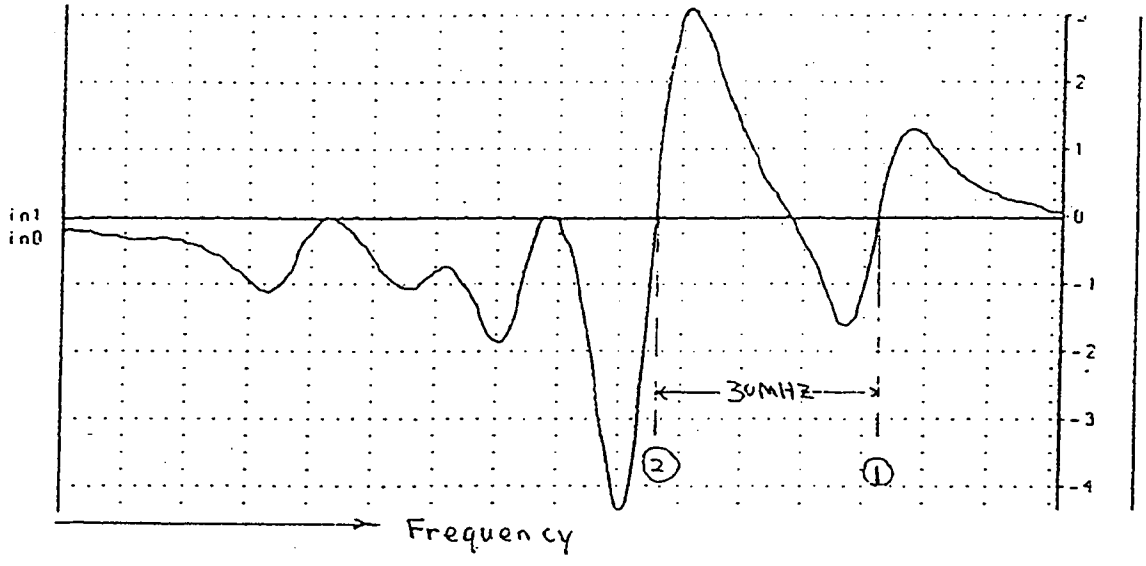

Figure 5.4 A frequency modulated saturation spectrum of the $3S_{1/2}$ F=2 to $3P_{3/2}$ transitions. Cross point (1) is transition F=2 to F'=3, cross point (2) is the cross of transition F=2 to F'=3 and transition F=2 to F'=2, the frequency distance between these two points is 30 MHz.

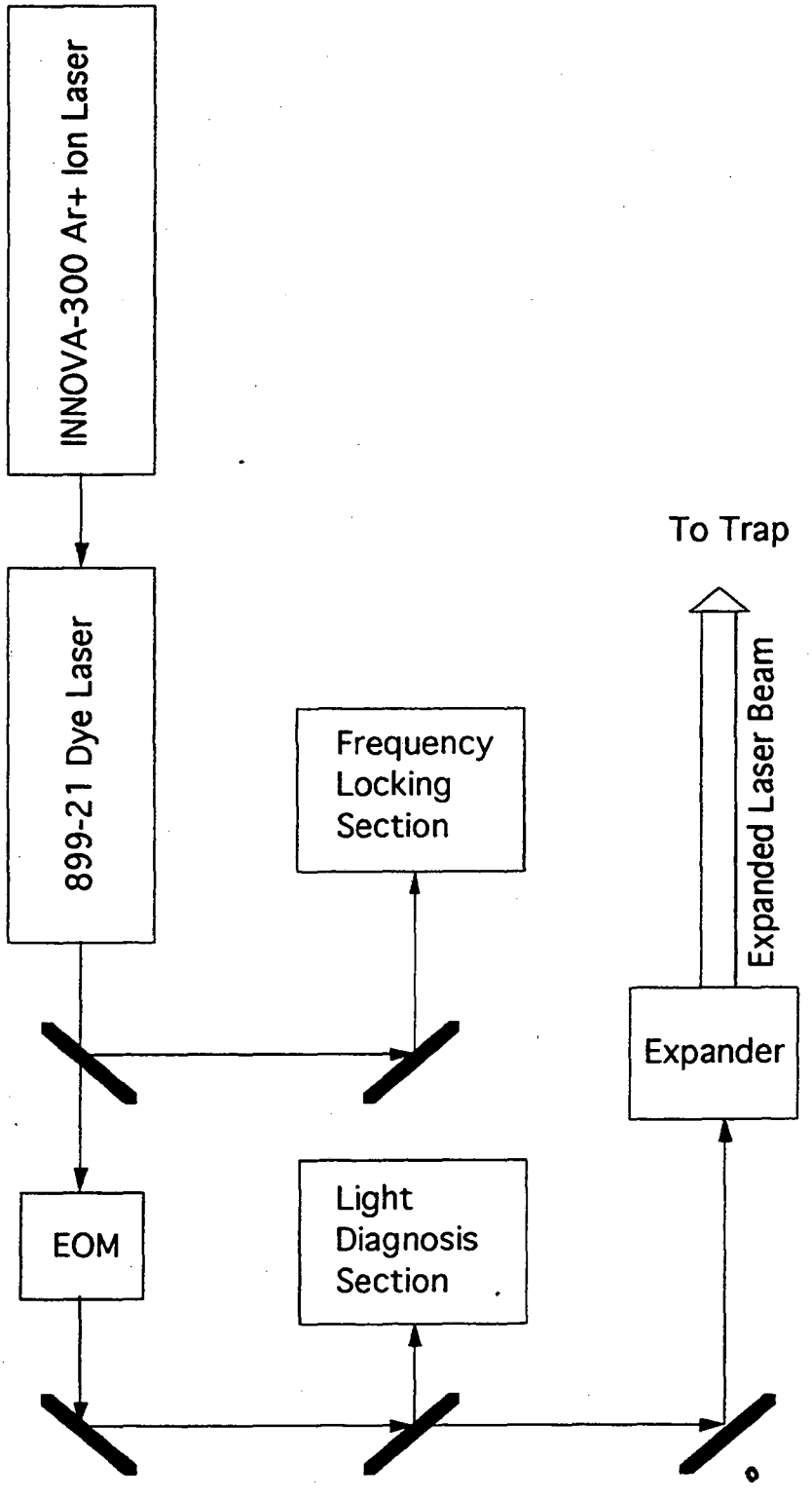

Figure 5.5 Arrangements of components on the laser table.

Chapter VI

A Magneto-Optical Trap with High Loading Efficiency

Development of a MOT with high loading efficiency is essential for the radioactive atom trapping experiments. Two similar apparatuses were set up, one on-line and one off-line. In this chapter, I will discuss the details of our off-line apparatus for testing and development with stable sodium atoms. The modifications on the on-line apparatus made to trap ^{21}Na atoms will be discussed in Chapter VIII .

6.1 Off-Line Apparatus

6.1.1 Sodium Oven

The sodium oven was designed to run at temperature below 500°C. In experimental runs, adequate atomic beam flux was obtained with oven temperature below 200°C.

The central part of the oven assembly is a rod of stainless steel mounted on a 4.5" Conflat flange. There is a cavity on the vacuum side of the rod where the sodium metal chips are loaded. A 1.33" small Conflat flange with a 0.33 mm (13 mil) diameter and 0.33 mm (13 mil) deep hole in the center seals the cavity. Four cartridge heaters are inserted from the air side of the rod, surrounding the cavity to ensure uniform heating on the oven.

At 200°C, the vapor pressure of sodium inside the oven is 2×10^{-4} torr. Assuming Na-Na collisional cross-section to be 100 $Å^2$, the mean free path of a sodium atom in the oven is 0.2 m, calculated according to the following equation [RA56],

$$\lambda = \frac{1}{n\sigma\sqrt{2}} = 7.321 \times 10^{-20} \frac{T}{p\sigma} \text{cm} \quad . \tag{6.1}$$

Here l is mean free path, n is the atomic density of the gas sample and σ is the collisional cross-section. In the second part of the equation, T is the temperature in °K, p is pressure in Torr and σ is in cm^2. Since the obtained mean free path greatly exceeds the exit channel length, the atomic beam is collimated by an exit hole with a solid angle of 2 std, compared to the solid angle 3×10^{-4} std subtended by the trapping region.

6.1.2 High Vacuum Region

The arrangements of the beam-line is shown in Fig 6.1

The oven is mounted onto a 6" UHV cube (15.24 cm x 15.24 cm x 15.24 cm, a Huntington vacuum product, VF-400-6) where the transverse cooling is conducted. Four view ports with clear aperture diameter of 9.85 cm (3.88") are mounted to the cube on the four sides surrounding the atomic beam axis.

A "4-way cross" (an MDC vacuum product, 405020) follows the cube. A 170 L/s turbo pump attached to the cross provides the initial stage of differential pumping. Vacuum pressure in this chamber is measured by a Bayard-Alpert ionization gauge. Vacuum

pressure is about 2 x 10^{-8} Torr under normal running condition. There is a collimator installed in the center of the cross. Its 1/4" hole limits the atomic beam flux going down stream, which provides the opportunity for differential pumping. An all-metal through-valve (a Huntington vacuum product, MS-150) mounted after the cross along the atomic beam-line isolates the trapping chamber when the oven is serviced or during occasional electrical interruptions.

6.1.3 Slow-Down Region

A tube of 1.2 m length and 3.3 cm inner diameter connects the valve to the trapping chamber. This tube fits inside the bore of the slowing solenoid. It provides low gas conductance, about 5 L/s, for the next stage of differential pumping.

The design for the slowing solenoid was provided by William Phillips' group, who developed the Zeeman tuned slowing technique. Following this design, 1.3 mm diameter solid copper wire with insulating sheath is wound around a 7.6 cm diameter tube and is all sealed in a cylindrical container. Freon from a closed cycle water cooled loop flows through the container to cool the magnet wire. Freon was chosen as cooling agent because it is a chemically inert coolant that does not support electrolysis. The vacuum tube does not touch the solenoid so it can be baked without heating the solenoid.

6.1.4 Trapping Region Vacuum Chamber

The trapping chamber shown in Fig 6.1 has eleven ports. It consists of a vertical 10.2 cm (4") diameter tube with a 6" Conflat flange on each end. Eight ports with 2.75" flanges are distributed on the same height with 45° between any adjacent two ports. A 500 L/s VacIon pump with a liquid nitrogen cold trap inside is connected to the chamber. The vacuum pressure in the chamber is measured by the ion pump. Under normal running conditions when the liquid nitrogen trap is filled, the pressure can go below 4.1×10^{-10} Torr, the lowest reading that the ion pump controller provides.

6.2 Magnetic Field

The measured longitudinal magnetic field profile is plotted in Figure 6.2. The slowing solenoid consists of two parts separately controllable: a uniform solenoid and a tapered solenoid.

In our experiments, the slowing laser beam has an intensity of 20 mW/cm^2 with 2/3 of the power on the carrier and 1/6 of the power on each of its two sidebands. It is observed that increasing the light intensity further does not increase the trap loading efficiency since saturation intensity for D2 (F=2, M_F=+2) to (F'=3, M_F=+3) transition is only 6 mW/cm^2. From Equation 3.10, this slowing laser beam can produce a maximum deceleration of 6.9×10^7 cm/sec^2.

Plotted in Figure 6.2 is the longitudinal magnetic field setting on the slowing solenoid used in our experiments to obtain the maximum number of trapped atoms. The criteria

shown in equation 3.13 on the magnetic field for Zeeman tuned slowing is satisfied at every point along the atomic path. The maximum field is 1100 Gauss, corresponding to a cutoff speed of 850 m/s. It can be calculated according to equation 3.13 that the maximum deceleration set by this magnetic field is 5.9×10^2 cm/sec^2, less than the maximum deceleration provided by the slowing laser light intensity.

The extraction coils, as first described in Section 4.4, are installed at the low field end of the slowing solenoid. They form a uniform field solenoid, formed by winding 4 layers of magnet wires directly on the vacuum tube with a diameter of 3.81 cm (1.5"). To avoid any sharp dip or peak in the magnetic field at the joint of the slowing solenoid and extraction solenoid, the extraction coil is inserted into the slowing solenoid for about 2.5 cm (1"). On the other end, the extraction coil stops at the vertical wall of the trapping chamber. The field inside the extraction coil is about 150 Gauss, corresponding to atomic speed of about 140 m/s. In practice, we separated the extraction coil into three segments, 7.6 cm, 1.5 cm and 3.8 cm long respectively. This arrangement is somewhat arbitrary, mainly determined by where the chamber port join the vacuum tube. Each segment of the extraction coils has an independent current control so that the field can be fine tuned for smoothness.

One pair of Quadrupole coils are wound directly on the trapping chamber as shown in Figure 6.1. The coils are 12 cm in diameter and separated by 6 cm in Helmholtz geometry. The current in the two coils flow in opposite direction to provide the quadrupole field that a MOT requires. The field gradient near the center is about 20 Gauss/cm. The decreasing field from chamber wall to the trap at the center also provides the field needed in slowing.

The slowing solenoid, the Extraction coils and the Quadrupole coils combine to provide the continuously decreasing field for slowing. The basic strategy is to blend the trapping fields and slowing fields into a single system.

Since there are stray fields from all the coils listed above, we add a system of longitudinal and transverse trim coils to insure that the center of the quadrupole field (where B = 0) coincides with the center of the trapping chamber and the intersection point of the trapping laser beams.

6.3 Laser Beam Setup

Two optical systems were used during these experiments with 1 cm and 3 cm diameter trapping laser beams respectively.

For the 1 cm diameter laser beam system, the laser beam is split into four beams after spatial filtering and expansion by passing through a telescope. Each has about 20 mW of power with 2/3 of power on the carrier and 1/6 of power on each of the two sidebands. Figure 6.3 shows the geometrical arrangements of the four laser beams. One is the slowing beam counter-propagating the atomic beam and focused onto the oven orifice, while the remaining three are retro-reflected as in a six beam MOT.

For the 3 cm diameter laser beam system, the laser beam from the telescope is further expanded and then split into two beams only, one for slowing and one for trapping. Each has about 120 mW with the same power distribution over various frequency bands as in the 1 cm case. With limited laser power, the trapping beam has to be recycled through all

three orthogonal paths and retro-reflected. This makes beam directional tuning more difficult.

6.4 Light Detection Devices

Trapped atoms constantly absorb and emit photons. The orange fluorescent light can easily be seen by the naked eyè. To quantify the number of atoms in the trap, we measure the fluorescence by a calibrated PIN Silicon photo-diode (a Thorlab product, DET1-SI) and a calibrated charge coupled device (CCD) camera (see Fig 6.1).

Both devices were calibrated with a Newport power meter Model 840 with a power probe 818-SL, with a NIST traceable accuracy of ±3%.

6.4.1 Photo-diode

The PIN photo-diode outputs a DC current signal which is linearly dependent on the light power incident its 2 mm x 2 mm acceptance area. With a termination resistor, the current signal is converted into a voltage signal. The calibration data is shown in Figure 6.4. Within the calibrated range of 20 nW to 800 nW, the data agree with a straight line fit within 5%.

We use the photo-diode to measure the total number of trapped atoms. A trap is compact, the largest being about 1 cm in diameter. It can easily be imaged onto the photo-diode's

acceptance area. The photo-diode provides a real-time measurement which yields important feedback when tuning laser beam directions or laser frequency. It is also used for studying the decay and build up of trapped atoms. The limited sensitivity to light of this system of photo-diode and lens makes it practical only for measuring a trap with more than 10,000 atoms.

6.4.2 CCD camera

An atomic fluorescence image taken by a CCD camera is sent to a computer (Macintosh II) to study its geometry and brightness. The geometrical resolution of the image is 50 mm at current geometrical arrangement. There are totally 256 layers of brightness. Figure 6.5 shows the calibration data. Within the calibrated range of 9 pW to 370 pW, the data agrees with a linear fit within 10%.

The CCD camera is used to study atomic beams as well as traps. It is extremely sensitive to light. In a test of its sensitivity, a trap of 4×10^5 atoms (measured by the photo-diode) is imaged onto the CCD camera with a 1000 times attenuation neutral density filter in front of the lenses. This assured us that a trap with as few as 400 atoms can be studied with our CCD camera system. However, real-time measurement and response was not set up on our CCD system.

The photo-diode and the CCD camera were compared by studying the same image at the same time, and the results agree within 20%.

6.5 Atomic beam flux

In order to measure the total thermal atomic beam flux through the trapping region, we use the vertical retro-reflected laser beam. The trapping and slowing magnetic fields are turned off. The laser beam is 1 cm in diameter and 40 mW total power including the retro-reflected beam, with 1/6 of the power on each of its two sidebands. The laser frequency is tuned to the resonance with D2 F=2 to F'=3 transition. The sideband is 1712 MHz away from the carrier, on resonance with F=1 to F'=2 transition. The laser beams are circularly polarized and the polarization is reversed when the laser beam is retro-reflected, resulting in a superposition of $\sigma+$ and $\sigma-$ state. Fluorescence from the intersection of the laser beam and the atomic beam is detected by the CCD camera and analyzed for atomic beam intensity.

The number of atoms in the observation region is calculated from the measured fluorescence light with a "two-level" atom model that considers only one "averaged" transition with an oscillator strength obtained by averaging over all transitions between ground and excited level with equal weight. In the two-level atom model for sodium, the "averaged" transition of D2 F=2 to F'=3 transition has an oscillator strength of 28 (see Appendix B) and a saturation intensity of 13 mW/cm^2. This model is expected to work well with trapped atoms in a MOT because of the nearly isotropic light condition. However, only one vertical laser beam is used in the case of atomic flux measurements and the light condition is clearly anisotropic, which causes an uneven population distribution over the Zeeman sub-states of ground and excited level by optical pumping. Thus the results of the two-level atom model were compared with the results calculated with an "Equilibrium" atom model that assumes the population distribution over all Zeeman sub-states of ground and excited level is under equilibrium with the light at the same position through optical pumping interaction. These two models describe two ideal

cases at two extremes that bracket the real situation, and their results give us a sense of the reliability of our data. The difference of the results obtained from these two models arises from two factors:

1) In the two-level atom model, the level population is taken to be evenly distributed over the five Zeeman substates of the F=2 ground level. However, in the Equilibrium atom model, more atoms are found in $M_F = +2$ and -2 states because of optical pumping by $\sigma+$ and $\sigma-$ light. Since the oscillator strengths of transitions (F=2, $M_F = +2$) to (F'=3, $M_{F'} = +3$) and (F=2, $M_F = -2$) to (F'=3, $M_{F'} = -3$) are both equal to 60 (see Appendix B), about twice as big as the average, this results in a larger fraction of atoms in the excited level and a smaller inferred beam flux. However, the difference for our experimental conditions is only 5%.

2) In the two-level atom model, fluorescence is assumed to be distributed isotropically. In the equilibrium atom model, the spatial distribution of spontaneous photon emissions in electric dipole transitions is taken into account and it is anisotropic due to the anisotropy in the pumping of $\sigma+$ and $\sigma-$ light. Under our experimental condition, more photons are emitted in the direction of the laser beam and less light goes into the CCD camera, so larger atomic beam flux is inferred by the equilibrium atom model. This difference is about 10% under our experimental condition.

In comparison with the two-level atom model on the results of the atomic beam flux, the Equilibrium atom model gives 5% less due to the population distribution factor but 10% more due to the spatial distribution factor, so 5% more in total after combining these two factors.

6.6 Number of Trapped Atoms

The image of the trapped atoms is focused onto the photo-diode by a lens. The lens has a clear aperture of 1.9 cm in diameter, its focal length is 3.8 cm, and it is installed outside of the trapping chamber 10.1 cm away from the trap.

The numbers of trapped atoms were calculated with the two-level atom model. Because the trapping light that consists of six beams coming from six directions is more isotropic than in the case of atomic beam flux measurements, the difference between the two-level atom model and the equilibrium atom model should be less than 5%. The difference is neglected since it is much less than the 13% systematic error in the fluorescence light measurements.

6.7 Trap Loading Time

The number of trapped atoms reaches an equilibrium under the balance of loading and loss processes. Here we define the loading time as the time it takes to load a number of atoms (1-1/e) times the number under equilibrium.

Equation 6.2 describes the evolution of the number of trapped atoms during a loading period.

$$\frac{dN}{dt} = L - \alpha N - \beta N^2 \quad , \tag{6.2}$$

here the loading rate, L, is assumed constant since the atomic beam and laser light conditions change little during this period. The first loss term, $-\alpha N$, is due to the collisions between trapped atoms and thermal background atoms or molecules. When vacuum pressure is at 4×10^{-10} Torr, $\alpha = 0.15$ sec^{-1}. The second term, $-\beta N^2$, is due to the exorergic collisions between pairs of trapped atoms. The loss due to the collisions between trapped atoms and atoms in the beam is neglected here. Even at an atomic beam flux of 1×10^{10} sec^{-1}cm^{-2}, the atomic density in the beam is only 1.5×10^5 cm^{-3}, two orders of magnitude less than the background atomic density. In general, when atomic beam flux is high and 10^9 atoms are loaded, loss is dominated by the second loss term and loading time is short, about 0.5 sec; when atomic beam flux is low and 10^5 atoms are loaded, the first loss term dominates and the loading time is about 7 sec. The detail loss mechanisms will be examined in Chapter X.

To measure the loading time, the MOT is turned on as atoms are loaded into the trap. The evolving fluorescence signal recorded by the photo-diode is sent to a Macintosh computer in real time, where the signal as a function of time is recorded by "Superscope" (a digital oscilloscope simulator for Macintosh computers by GW instruments). The loading time is determined after the number of trapped atoms reaches equilibrium.

Figure 6.6 shows the measured number of trapped atoms as the function of the atomic beam flux. The number of trapped atoms increases slower than the atomic beam flux does because the loading time is reduced when the number of trapped atoms is larger and the second loss term becomes dominant (see Chapter 10).

6.8 Trap Loading Efficiency

Trap loading efficiency is defined as the ratio of the number of the atoms that are captured by the trap to the number of the atoms in an atomic beam that passes the trapping region.

$$\varepsilon = \frac{N}{T_l \cdot F} \quad , \tag{6.3}$$

here ε is the loading Efficiency, N is the number of Trapped Atoms, T_l is the loading time and F is the atomic beam flux. Note that in this definition of the efficiency, atomic beam flux is the flux of the thermal atomic beam, not the slowed beam.

Figure 6.7 shows a number of measurements of the efficiency for various oven temperatures. The average efficiency is 19%. Considering the maximum speed of atoms that can be slowed with current setting of the high field of the slowing solenoid, and assuming no loss during slowing process, about 82% of atoms are slowed under oven temperature of 50°C and about 69% of atoms are slowed under oven temperature of 150°C. If the un-slowed part of the atomic beam is not taken into account, the loading efficiency is about 25% to 30%.

6.9 Transverse Cooling

Transverse cooling (see Section 3.2) does not change loading efficiency, but increases the on-axis atomic beam flux instead. Overall, it increases the number of trapped atoms with the same oven output.

Transverse cooling is best done near the oven exit hole before the atomic beam expands to a size larger than the laser beams. In our experiments, the interaction region is in the vacuum cube where the oven is mounted, about 5.1 cm away from the oven exit hole. The trapping region is 150 cm away from the oven exit, making the solid angle by a MOT formed with 1 cm diameter trapping laser beams towards the oven exit hole 4.4 x 10^{-5} std. Without transverse cooling, only the atoms inside this solid angle reach the trapping region. With transverse cooling, more atoms, inside a larger solid angle, can be directed towards the trapping region. Here a numerical example of this effect is presented. The transverse cooling laser beam has 1 cm of diameter and 100 mW of power, detuned 20 MHz below resonance. With laser intensity being 7.7 times the saturation intensity, the laser linewidth is power broadened to $\Gamma\sqrt{1+I/I_{sat}} = 29\text{MHz}$.

The capture velocity of transverse cooling, corresponding to a Doppler shift of a half of linewidth, is 9 m/s. This characteristic velocity is used to estimate the velocity capture range of transverse cooling. Roughly, in this example, only atoms with a transverse velocity less than 9 m/s will be cooled down to the Doppler limit (0.3 m/s, see Section 3.2) and directed to the trapping region. At an oven temperature of 200°C, the average velocity of atoms in the beam is 780 m/s. We can estimate that atoms inside a forward solid angle of about 5.3 x 10^{-4} std are transversely cooled, increasing the on-axis flux by a factor of 12.

In practice, it is observed that this factor of increase of flux does not directly translate into the factor of increase on the number of trapped atoms because the loading time is reduced as flux increases. A typical measurement shows that a trap of 5.0 x 10^{6} atoms is increased to 7.5 x 10^{7} atoms by transverse cooling.

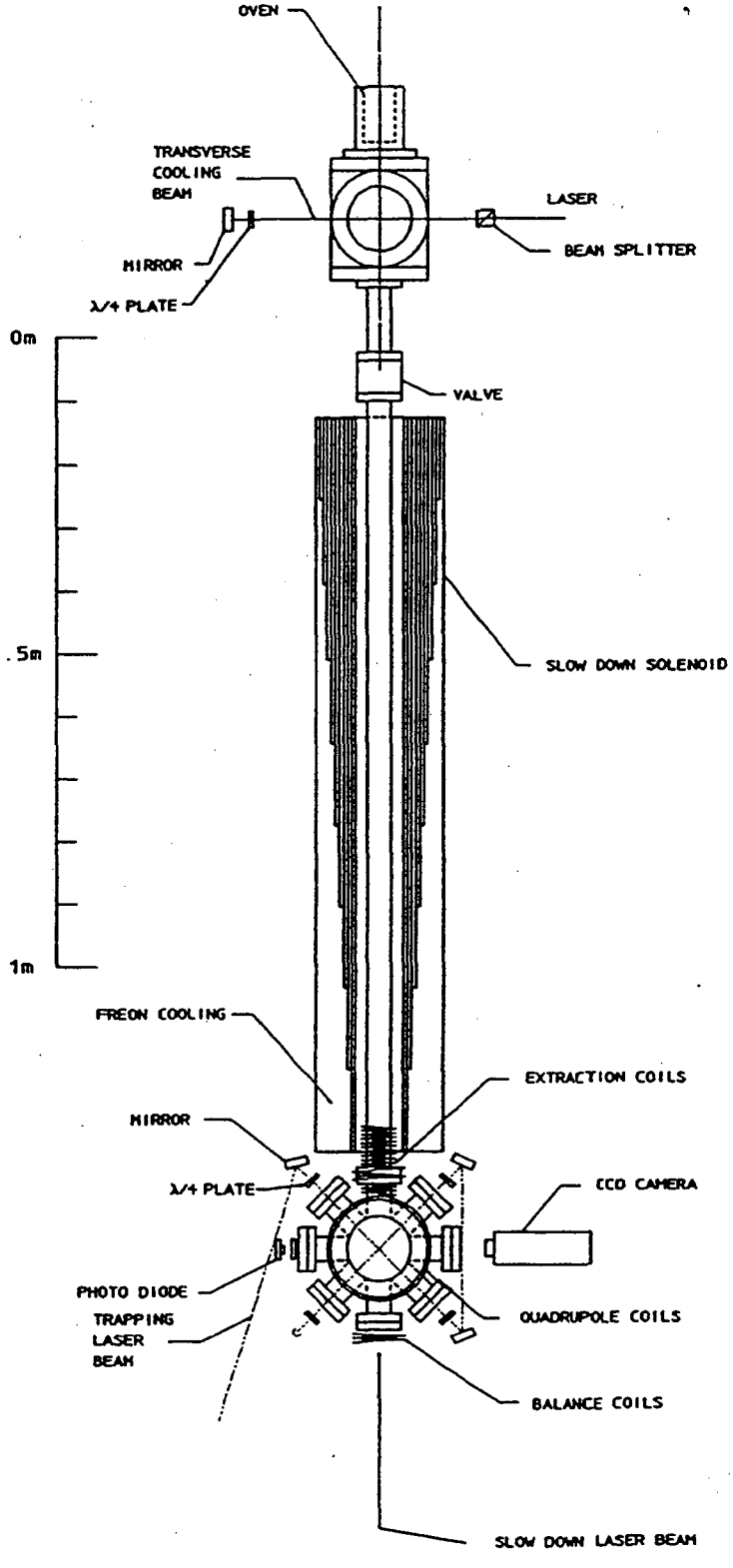

Figure 6.1 Schematic diagram of the apparatus.

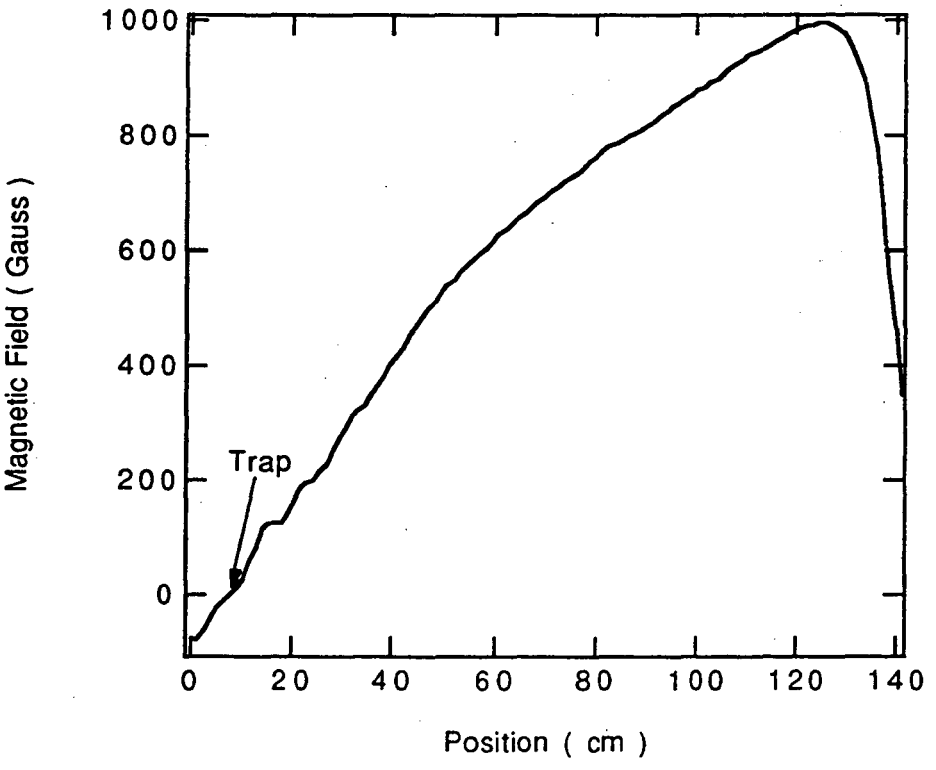

Figure 6.2 The measured longitudinal magnetic field strength along the atomic beam path.

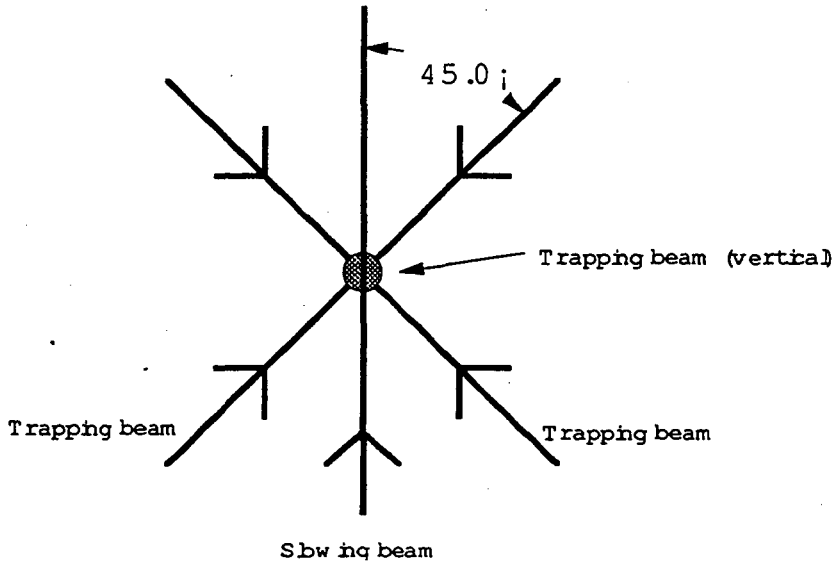

Figure 6.3 The geometrical arrangement of the laser beams.

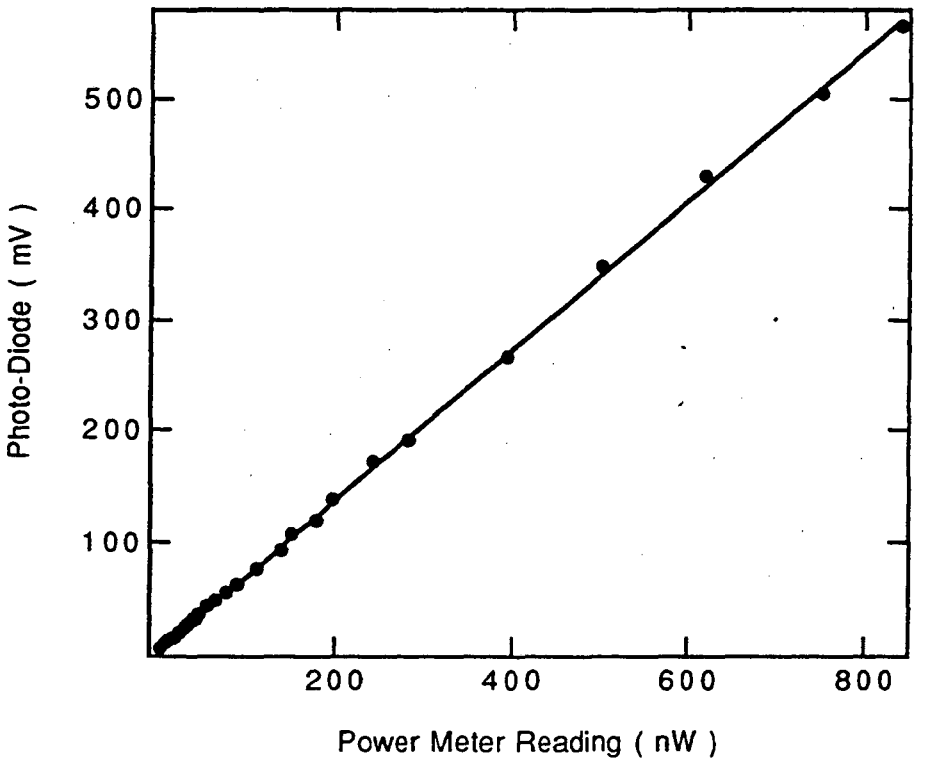

Figure 6.4 The calibration of the photo-diode with a Newport power meter.

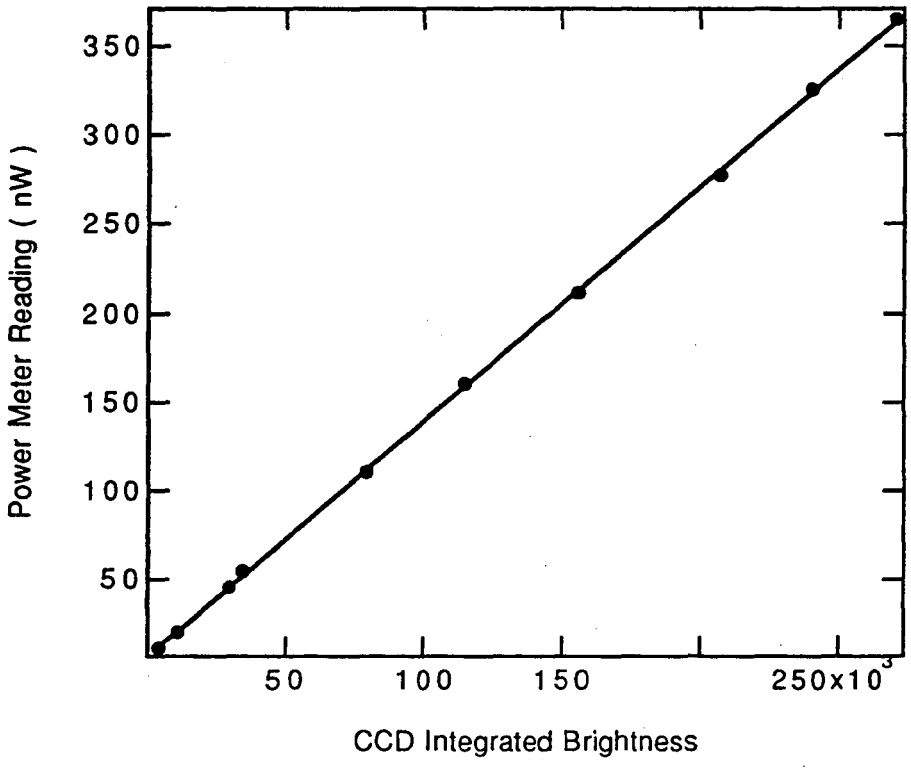

Figure 6.5 The calibration of the CCD camera with a Newport power meter.

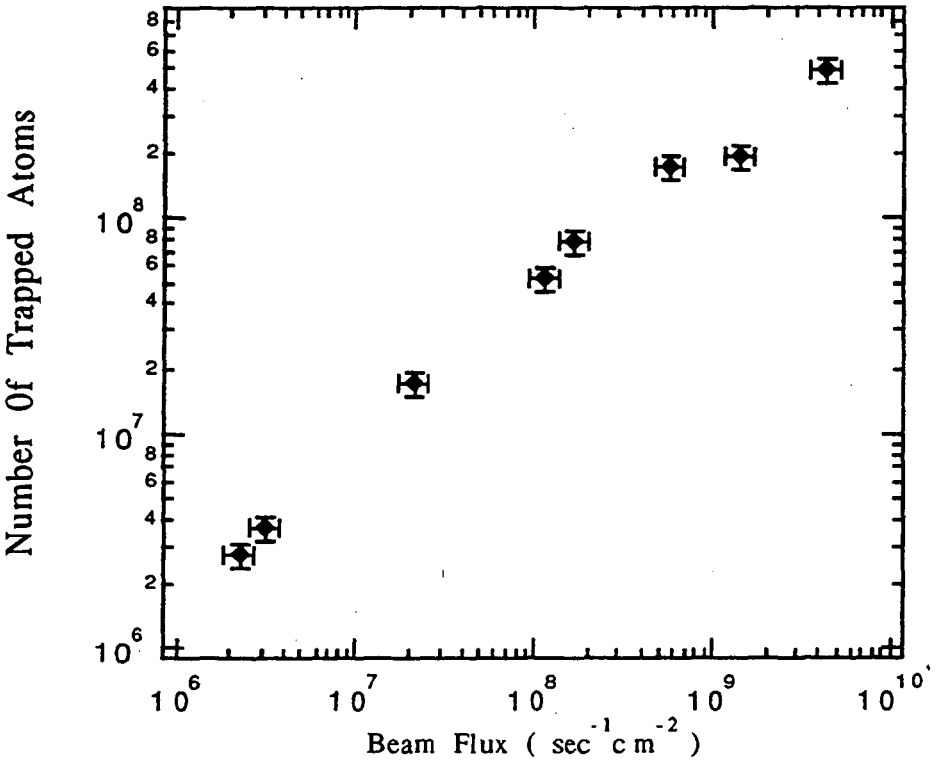

Figure 6.6 Number of trapped atoms vs. Atomic beam flux. The relative error on the number of trapped atoms is 13%, on the beam flux is 20%. Note the logarithmic scale. The ratio of Number over Flux decreases as Flux increases, due to the shorter loading time at higher flux.

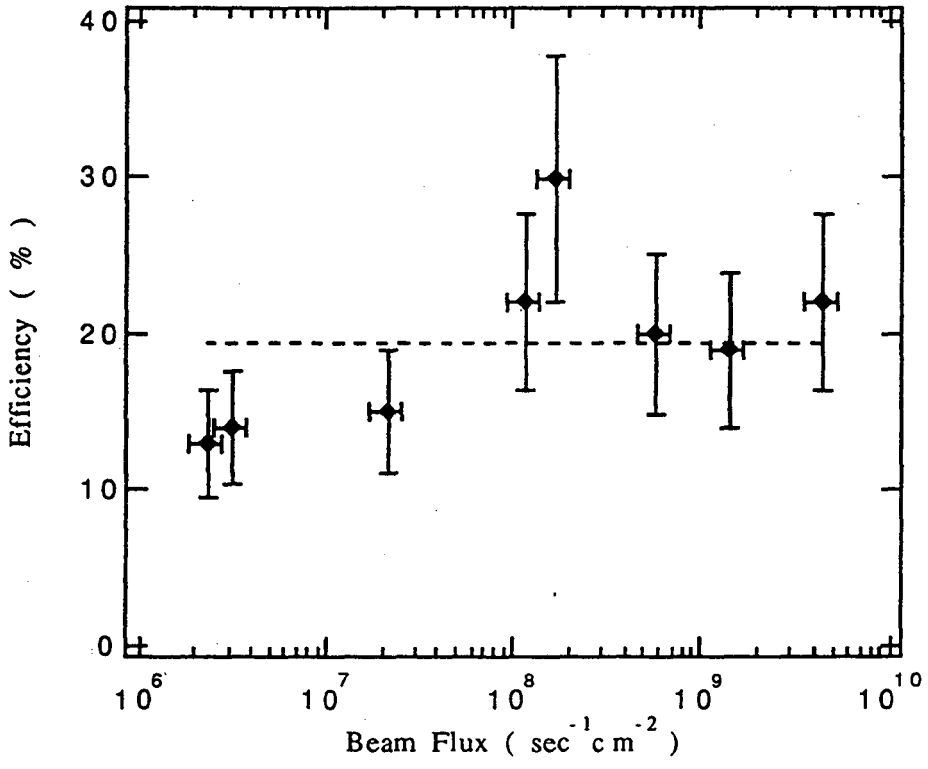

Figure 6.7 Trap loading efficiency with various atomic beam flux. The averaged efficiency is (19.4±1.8)%, marked by the horizontal broken line. The relative error on each efficiency datum is 26%, on the beam flux is 20%.

Chapter VII

Making of a ^{21}Na Atomic Beam

The half-life of ^{21}Na nucleus is only 22.47 seconds and our experiments must be done on-line with an accelerator. In this chapter, I will first introduce two early experiments that made ^{21}Na atomic beams, then discuss making and detecting ^{21}Na atoms in our experiments.

7.1 Early Experiments

There have been two previous experiments in which beams of ^{21}Na were used. The spectroscopic data obtained by these experiments are essential to our laser manipulation experiments.

7.1.1 The Princeton Experiments [AM65]

^{21}Na atomic beam was first made by O. Ames et al. in their experiments that measured the ground-state hyperfine splitting. In their experiments the target material is

magnesium powder, the ^{21}Na being produced by the reaction ^{24}Mg(p,α)^{21}Na. A proton beam with energy of about 18 MeV was used and a typical beam intensity was 0.075 mA.

Magnesium powder was loaded into an oven that was kept at about 450°C, close but below Mg's melting point of 651°C. The oven consisted of a main body, a cover plate and a tungsten foil sandwiched in between. The proton beam could easily go through the thin foil and reach Mg, while atoms could only come out through the exit hole.

After ^{21}Na nuclei were produced, some of them migrated out of the Mg powder and found their way out through the exit hole of the oven. ^{21}Na beam intensity was measured by inserting a copper "flag" directly in front of the oven hole. Some of the atoms that hit the flag stuck on to it. The flag was pulled out after exposure and the radiation is counted.

The typical production rate was about 6×10^7 per sec in the oven and about 1.4×10^7 ^{21}Na atoms per sec left the exit hole.

By using the magnetic resonance method, they determined the nuclear spin of ^{21}Na, I = 3/2, and its ground-state hyperfine splitting, $\Delta f = 1906.466 \pm 0.021$ MHz. From that they calculated the magnetic moment of ^{21}Na $\mu = +2.38612 \pm 0.00010$ (nuclear magneton).

7.1.2 The CERN Experiments [TO81, TO82]

In these experiments, the D2 line hyperfine structure of ^{21,25,26,27}Na were measured by laser spectroscopy. The isotope shift for each isotope listed above was determined. The information about ^{21}Na is listed in Appendix A.

This was done at CERN with the Proton Synchrotron. A proton beam of 20 GeV bombarded a target made of Silicon evaporated on graphite slabs. Na isotopes were products of spallation reactions. In this way, many different isotopes could be produced. Furthermore, a beam of pure isotopes could be selected out by ion mass separator.

The hyperfine splitting of the excited levels were measured using optical pumping and magnetic resonance technique.

7.2 Nuclear Reactions

Our method of producing ^{21}Na atoms is similar to the Princeton experiments, although the detailed design is different.

The main reaction is ^{24}Mg(p,α)^{21}Na. Figure 7.1 [GR77] shows the cross-section as a function of proton center-of-mass energy (E_p^{CM}), 0.92 times the proton energy (E_p) in lab frame, $E_p^{CM} = 0.92 \times E_p$. According to these measurements, the cross-section drops to 10 mbarn at Ep = 11 MeV, about an order of magnitude lower than the value at Ep = 14 MeV. Although the cross-section was only measured for proton energies below 14 MeV, we chose to use the 25 MeV proton beam under the assumption that the cross-section number does not drop abruptly between 14 MeV and 25 MeV. The benefit of using higher energy protons is that they can penetrate deeper into magnesium so that higher yield of ^{21}Na is expected. The range of protons in magnesium metal is 4.4 mm at 24 MeV of proton energy (protons lose 1 MeV of energy by passing through the oven window, see Section 7.3), 1.7 mm at 14 MeV, and 1.1 mm at 11 MeV. The useful range,

within which the ^{21}Na production is significant, is 3.3 mm for 25 MeV protons and 0.6 mm for 14 MeV protons, so 5.5 times more ^{21}Na production is expected for 25 MeV protons.

The magnesium we used was chemically processed with a purity of 99.9%, obtained from Johnson Matthey Catalog Company. According to natural abundance, it consists of three stable isotopes of Mg, 78.99% of ^{24}Mg, 10% of ^{25}Mg and 11.01% of ^{26}Mg. This complicated the production process. Many unstable isotopes were produced along with ^{21}Na. They are listed in Table 7.1

Table 7.1 A list of radioactive reaction products in the oven.

Product	Radia--tion Type	Half-life	Reaction	Thre--shold (MeV)	Critical Energy (MeV)	Produc--tion Rate (1/sec)
21Na	β+	22.47 s	24Mg(p,a)21Na	6.9	12.8	1.6e9
			25Mg(p,an)21Na	14.2	20.1	
22Na	β+	2.6 yr	25Mg(p, a)22Na	3.1	9.0	3.1e8
			26Mg(p, an)22Na	14.2	20.1	
24Na	β-	15.03 h	25Mg(p, 2p)24Na	12.1	19.9	8.2e7
24mNa	β-	20.21 ms	25Mg(p, 2p)24mNa	12.5	20.3	7.1e7
25Na	β-	60. s	26Mg(p, 2p)25Na	14.1	21.9	4.6e7
23Mg	β+	11.33 s	24Mg(p, d)23Mg	14.3	18.2	1.4e9
			24Mg(p, pn)23Mg	16.5	20.4	
24Al	β+	2.05 s	24Mg(p, n)24Al	14.7	14.7	1.3e9
24mAl	β+	129 ms	24Mg(p, n)24mAl	15.1	15.1	1.2e9
25Al	β+	7.17 s	24Mg(p, γ)25Al	-2.3	3.9	2.5e9
			25Mg(p, n)25Al	5.1	5.1	
			26Mg(p, 2n)25Al	16.1	16.1	
26mAl	β+	6.36 s	25Mg(p, γ)26mAl	-6.1	3.9	5.5e8
			26Mg(p, n)26mAl	5.0	5.0	

Here the critical energy is the larger one between the Coulomb barrier of the entrance channel (3.9 MeV), and the sum of the threshold and the Coulomb barrier of the exit channel. The production rate is an estimated number at our experimental condition, assuming 200 nA of 25 MeV proton beam bombarding an oven loaded with natural

magnesium. Protons lose 1 MeV of energy by passing through the oven window. The magnesium load can be considered a thick target since its effective depth is 3.6 mm, longer than the useful range of any reaction listed above. The cross-section of each reaction is assumed to be 100 mbarn when the proton energy is above the critical energy, and zero when the proton energy falls below. Only a few reactions listed above have measured cross-sections. The cross-section of $^{24}Mg(p,\alpha)^{21}Na$ is measured with energy of proton ranging from threshold to 13 MeV [GR77], the ^{22}Na production rate of proton bombarding natural magnesium is measured from threshold to 100 MeV [ME51], and the cross-section of $^{25}Mg(p,2p)^{24}Na$ is measured (σ = 54 mbarn) at 21.5 MeV [CO55]. The effects induced by the undesired radioactive products on our signals depend on the whole atom transport process, which will be explained in section 7.4.5.

7.3 The ^{21}Na Atomic Beamline

7.3.1 Oven Assembly

We have used four different designs with many small modifications. Here I will describe the final version and some possible improvements.

Figure 7.2 is a photograph of the oven assembly. The critical part is the oven insert, similar to the oven used in reference [AM65]. It consists of: 1) a stainless steel oven body with a cavity for magnesium; 2) a stainless steel flange with a window; 3) and a piece of 0.05 mm (2 mil) thick tungsten foil. The flange seals the foil to the oven body. The energy loss of the proton beam in the tungsten window is 1 MeV.

With the oven at 480°C, the vapor pressure of magnesium is about 5 x 10^{-2} Torr (see figure 7.3), corresponding to a mean free path of 1 mm (see equation 6.1), this applies to both magnesium and sodium atoms since their diameters are about the same. The cylindrical oven orifice is 1.0 mm (40 mil) long and 1.0 mm of diameter, which helps in collimating the atomic beam. According to a calculation in reference [CL29], comparing with an oven with an orifice of the same diameter but much shorter length, the atomic out flow rate is reduced by a factor of 1.4 while the on-axis beam intensity remains the same.

The cavity size is 1.27 cm (1/2", horizontal length) x 0.95 cm (3/8", vertical length) x 1.27 cm (1/2", depth), in which we typically load 0.5 gram of magnesium grains. The incident protons lose about 15 MeV of energy in the magnesium and finally stop in the oven body. This oven insert fits into a copper block that is heated by two cartridge heaters (made by Watlow Electric Heating Technology). The copper block acts as a vacuum feed-through for heat. An isolated tantalum collimator sits in front of the oven insert. The proton beam hitting the collimator is measured while the beam position is adjusted. Outside of the copper block are two layers of stainless steel sheets that serve as heat shields. With their help, only 50 watts are needed to heat the oven up to 500°C. The entire assembly is mounted on a 6" Conflat flange. It can easily be installed and removed from the oven chamber. Two thermocouples, one attached to the oven insert, another to the copper block, monitor the temperatures.

7.3.2 Beamline

Figure 7.4 shows the equipment used to measure the ^{21}Na atomic beam intensity. The oven is located inside Cave01 at the LBL 88" cyclotron. The atomic beamline passes

through a 30.5 cm (12") hole in the 1.27 m (50") thick radiation shielding wall. As shown in figure 7.4, the radioactive atoms are counted outside the cave, where the radiation background is relatively low.

Two turbo pumps, one attached to the oven chamber and the other to the counting chamber, maintain a vacuum of 1×10^{-6} Torr corresponding to a mean free path of 20 m.

7.3.3 Atom Collector

An atom collector is installed at one end of the atomic beamline. Some of the ^{21}Na atoms stick to this 2.5 cm x 2.5 cm x 0.6 cm aluminum plate mounted at 45° to the atomic beam. As ^{21}Na nuclei decay (see Appendix C), half of the positrons go into the plate and annihilate. The thickness of the plate was selected so that almost all the positrons going into the plate are stopped while 511 keV gamma rays are not significantly attenuated.

The sticking probability of atoms on a surface varies from 0.0001 to almost 1, depending on the materials, temperature, surface condition, etc. A general discussion on this problem can be found in reference [RA56]. A collector coated with sulfur was first used in the measurements of ^{21}Na atomic beam intensity. High collection efficiency is expected, since the sticking probability of rubidium atoms on sulfur surface was reported to be near 100% [HO54]. Another advantage of sulfur surface is its consistency [SHU91]. An oxidized sulfur atom forms a gas molecule (SO_2) and leaves the surface so a pure sulfur surface is always maintained. However, its large out-gassing rate makes the sulfur surface collector incompatible with the ultra-high vacuum system. Collectors with an aluminum surface were used in the later atom trapping experiments. We measured

that the sticking probability of sodium on an aluminum surface is 80% of the probability for a sulfur surface. In order to obtain consistent results with aluminum surface collectors, a regular processing procedure is followed: first, the oxidized surface is removed with a sand blaster; then the collector is washed with ethanol and immediately mounted into the vacuum chamber.

7.4 Electronics

Two cylindrical 7.5 cm (diameter) x 10.5 cm (length) NaI(Tl) detectors are mounted 4.1 cm apart as shown in figure 7.3. They monitor the rate of 511 keV gamma ray radiation. From the coincidence rate, we can deduce the number of ^{21}Na atoms on the collector.

Figure 7.4 shows the setup of a standard coincidence counting electronics. The detectors are biased to +2 kV with two Ortec 456 high voltage supplies. The signal from each detector is copied into two identical signals by a linear fan-in-fan-out (LeCroy 428F). One is sent to an ADC (analog to digital converter, Ortec AD811) for energy measurements, the other triggers a NIM logic signal by a discriminator (LeCroy 622) for timing measurements. These two logic signals are sent to a TDC (time to digital converter, LeCroy 2228A) that measures the distribution of the arrival time difference of the two photons. The coincidence of these two logic signals is detected by a logic unit (LeCroy 365AL), and the coincidence rate is counted by a scalar (LeCroy 2251). All these modules are controlled by a computer (Macintosh Quadra 950) through a CAMAC crate controller (MAC-CC Type 392, a product of Bergoz). The acquired data are stored and processed on the computer with K-max (a Sparrow product) software. This acquisition system has a large dead time of 5.5 ms. It is slowed down by live data

transferring between the CAMAC crate controller and the computer during the counting period. This problem will be fixed by installing a list processor with the crate controller. Data can be stored in the list processor during the counting period and transferred to the computer afterwards. The deadtime is expected to be reduced by a factor of 50. For now, the counting rates are deadtime corrected with the following equation,

$$R_{corr} = \frac{R}{1 - R \cdot t_d} \quad . \tag{7.1}$$

Here R is the recorded counting rate, R_{corr} is the deadtime corrected rate and t_d = 5.5 ms is the deadtime. For example, if 100 sec^{-1} of counting rate is measured, then the actual coincidence rate should be 222 sec^{-1}, obtained after correction with equation 7.1.

The time sequence of a typical counting cycle is:

t = 0 sec, cycle starts;

t = 1 sec, proton beam is switched on;

t = 61 sec, proton beam is switched off;

t = 62 sec, counting starts;

t = 162 sec, counting stops.

It is controlled by a timing generator (Kinetic system, model 3655).

The photon counting system is calibrated with a ^{22}Na positron source before every run. The detection efficiency, which is the ratio of coincidence trigger rate over β^+ decay rate on the plate, is 18% in a typical run. In a measurement of background check, the atomic beamline is valved off, in which case no atom from the oven can reach the catch plate, and the coincidence rate is reduced by a factor 20.

A 10 MHz clock signal is obtained from a frequency counter (Hewlett-Packard 5386A). Its aging and temperature shift is less than 50 Hz. The frequency is scaled down to 100 Hz by three succeeding counters (LBL 21X79810-1), which provides the time-base for half-life measurements.

7.5 Results

Table 7.2 gives a numerical example of our ^{21}Na beam intensity measurement.

Table 7.2 A measurement of ^{21}Na atomic beam intensity.

Proton beam energy	25 MeV
Proton beam current	200 nA
^{21}Na nuclear production rate	2×10^{9} sec^{-1}
Oven temperature	500°C
Solid angle of collector from oven	1.4×10^{-4} std
Photon coincidence detection efficiency	18%
Coincidence rate under equilibrium	222 sec^{-1}
Decay rate of ^{21}Na on collector under equilibrium	1×10^{3} sec^{-1}
Rate of ^{21}Na leaving oven	2×10^{7} sec^{-1}

Here the nuclear production rate is estimated with nuclear reaction cross-section. The aluminum collector is used and its sticking probability is assumed to be 80%.

Figure 7.5(a) shows an energy histogram recorded by one of the two photon counters in a coincidence measurement. 40% of the data is in the full energy peak. If the Compton plateau is also included with full energy peak, then 90% of the total events are real 511 keV annihilation photons.

Figure 7.5(b) shows a decay curve of coincidence trigger rate. A fit to an exponential function gives a half-life of 21.53 ± 0.56 sec, compared with the commonly accepted number of 22.47 ± 0.03 sec [LE78]. The shorter half-life can be explained by the possibility of atoms leaving the collector during the counting period. To account for the difference, the average time of atoms staying on the plate would be about 740 sec. Another possible explanation of the shorter observed half-life is that there are some other β^+ emitting atoms on the plate, like those listed in Table 7.1. For example, if ^{23}Mg is the single contaminant to cause this observed difference, then the number of ^{23}Mg atoms on the collector would be 5% of the number of ^{21}Na atoms. Radioactive contamination in the beam does not present a critical problem because laser manipulation of atoms is an isotopically selective process. In the proper arrangement of the laser, only ^{21}Na atoms are trapped.

7.6 Diffusion in the Target

The number of ^{21}Na atoms in the atomic beam depends on the production rate and the transport efficiency. The transport process consists three stages: 1) diffusion to the surface of a grain; 2) surface desorption; 3) diffusion to the oven exit through the gaps among powders. Beta decay can occur at each stage of the process so only a fraction of radioactive atoms reach the collector.

The second and the third stages depend critically on the adsorption time of sodium atoms on a magnesium surface. This is the average time that an atom stays on the surface for each encounter. Its temperature dependence is given by [BO68]

$$\tau = 10^{-13} \cdot \exp\left(\frac{E_a}{k_B T}\right) \text{sec} . \tag{7.2}$$

Here E_a is the surface desorption energy, k_B is the Boltzmann constant and T is the absolute temperature. Although not measured for our specific case, E_a is less than 1 eV in general. Assuming E_a = 1 eV and T = 500°C, our calculation shows that $\tau = 3 \times 10^{-7}$ sec, so the second stage, surface desorption, can be neglected because it occurs in a time much less than the mean lifetime of ^{21}Na. The average time for an atom to pass through a capillary of length L and radius r is given by [BO68]

$$t_{ave} = L^2\left(\frac{1}{4rv} + \frac{\tau}{8r^2}\right) , \tag{7.3}$$

where v is the average velocity of the atom. In order to estimate the time that a ^{21}Na atom takes to diffuse through magnesium powder in our oven, we set L = 6 cm, ten times the physical height of the target, and r = 0.05 mm, about the same size of each grain of magnesium powder. It can be calculated with equation 7.3 that t_{ave} = 0.9 sec at the oven temperature of 500°C. Thus the loss of ^{21}Na atoms during the third stage can be neglected too.

The first stage can be modeled by solving Fick's second diffusion equation [CA78]. Assuming an initial condition (t=0) of n_0 ^{21}Na atoms uniformly distributed inside a

spherical grain, the number of ^{21}Na atoms remaining in the grain as a function of time can be expressed as

$$n(t) = n_0 e^{-\lambda t} \cdot \frac{6}{\pi^2} \sum_{k=1}^{\infty} \frac{\exp\left(-k^2 \sigma \cdot t\right)}{k^2} \quad , \tag{7.4}$$

where $\lambda = 0.0308$ 1/sec is nuclear decay rate and s is a parameter related to the diffusion coefficient D as

$$\sigma = \frac{\pi^2 D}{r^2} \quad , \tag{7.5}$$

with r being the radius of the spherical grain. Reference [LI90] listed measured D coefficients of six elements diffusing in magnesium. At 500°C, the largest D is 3×10^{-9} cm^2/s for silver, the smallest is 3×10^{-13} cm^2/s for uranium while the magnesium self-diffusion coefficient is 1×10^{-9} cm^2/s. Unfortunately, the D coefficient for sodium in magnesium is not measured, but a reasonable estimate can be obtained in the following way.

We take data (see figure 7.7) from runs in which the atomic beam is left on during a counting period after the proton beam is cut off. The decay curve is distorted because of the continuous loading from the oven. This decay curve is fitted with a function derived from equation 7.4:

$$\text{Counts}(t) = W_0 + e^{-\lambda t} \cdot \left[W_1 \cdot \sum_{k=1}^{\infty} \frac{\left(1 - e^{-(k^2\sigma+\lambda)t_1}\right)\left(1 - e^{-k^2\sigma t}\right)}{\left(k^2\sigma + \lambda\right)k^2} + W_2 \right] . \tag{7.6}$$

This function has four free parameters, W_0, W_1, W_2 and s. The fitting results (see figure 7.7) determine that $\sigma = (2.5 \pm 0.6) \times 10^{-6}$ sec^{-1}, corresponding to $\Delta = 6 \times 10^{-12}$ cm^2/s when r = 0.05 mm (see equation 7.5). This result shows that the first stage, diffusion inside each grain of magnesium powder, is the main reason for the delay of ^{21}Na atoms coming out of the oven.

From equation 7.4, the fraction of ^{21}Na atoms that diffuse out of a magnesium grain can be obtained as following:

$$F = \frac{6}{\pi^2} \sum_{k=1}^{\infty} \frac{\sigma}{k^2 \sigma + \lambda} \approx \frac{3}{\pi} \sqrt{\frac{\sigma}{\lambda}} \quad , (\sigma << \lambda) \ . \tag{7.7}$$

Using our estimated value of σ, it can be estimated that about 0.9% of the ^{21}Na atoms diffuse out of the oven, while the rest of them decay during the diffusion process. There are two target modifications that may improve the transport efficiency: 1) Higher oven temperature. For example, if the oven temperature is set at 600°C (note the melting point of magnesium is 650°C), then $\sigma = 5 \times 10^{-5}$ 1/s and F = 4%, about a factor of 4 increase in atomic beam intensity. On the other hand, raising the oven temperature from 500°C to 600°C increases the vapor pressure of magnesium by a factor of 10 (see figure 7.3), which results in 10 times shorter running time for one charge of oven. Currently, one charge of oven (0.5 g) lasts for about 24 hours at 500°C, so higher temperature demands a larger oven. 2) Finer magnesium powder. For example, reducing the radius of a grain by a factor of 4 (i.e. from 4 mil diameter down to 1 mil) increases s by a factor of 16 (equation 7.5) and increases F by a factor of 4 (equation 7.6).

'Sintering' effect may prevent either modifications. This process causes the magnesium grains to join together, resulting in larger grain size. In general, it is observed [AM65,

CA78, SHU91] that this effect becomes more severe as temperature approaches the melting point of the material, or as grain size shrinks. This effect should be investigated in further experiments.

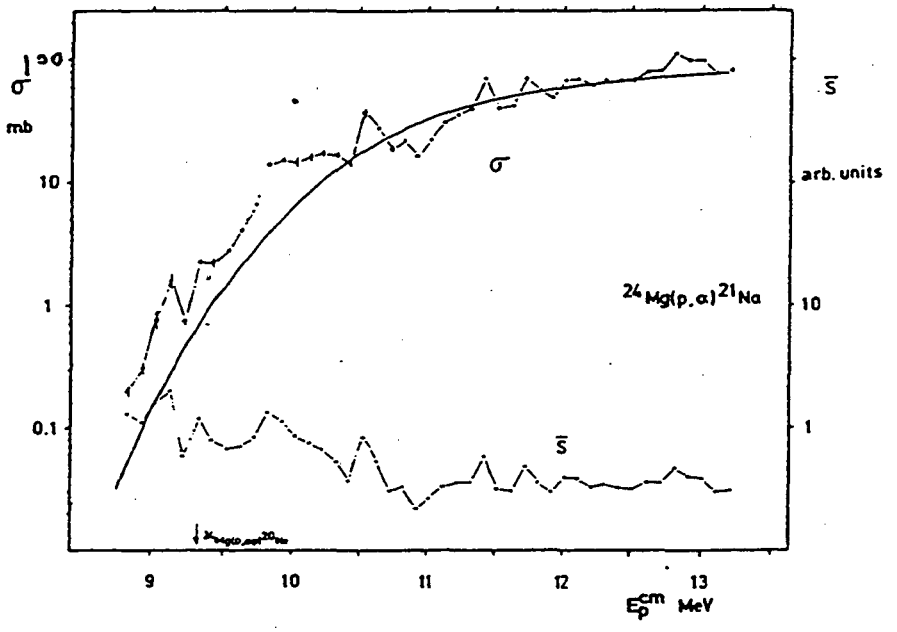

Figure 7.1 Absolute cross section of the reaction $^{24}Mg(p,\alpha.)^{21}Na$. The threshold is at $E^{c.m.}_p = 6.884$ MeV [GR77].

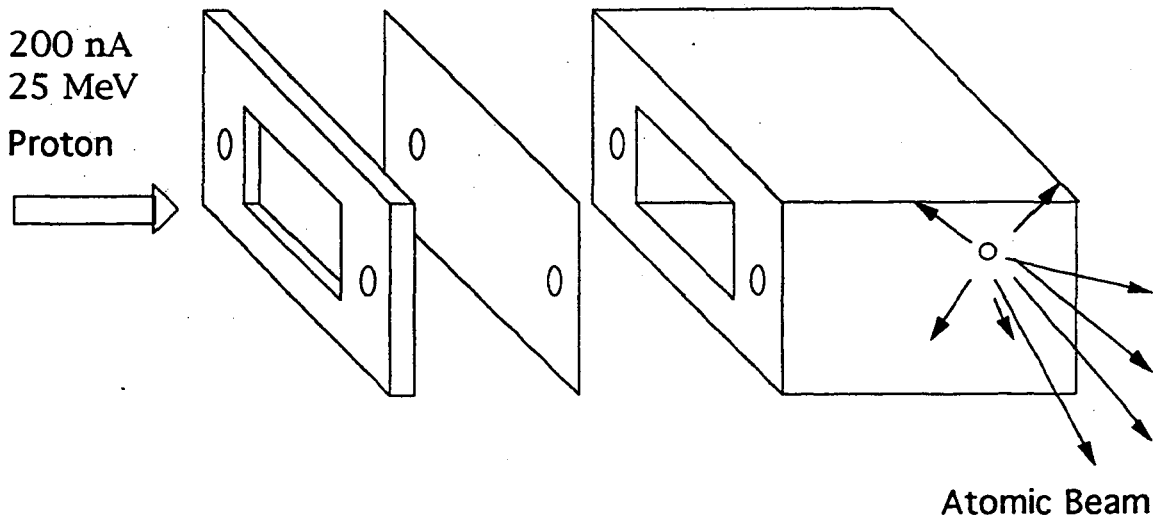

Figure 7.2 The oven assembly.

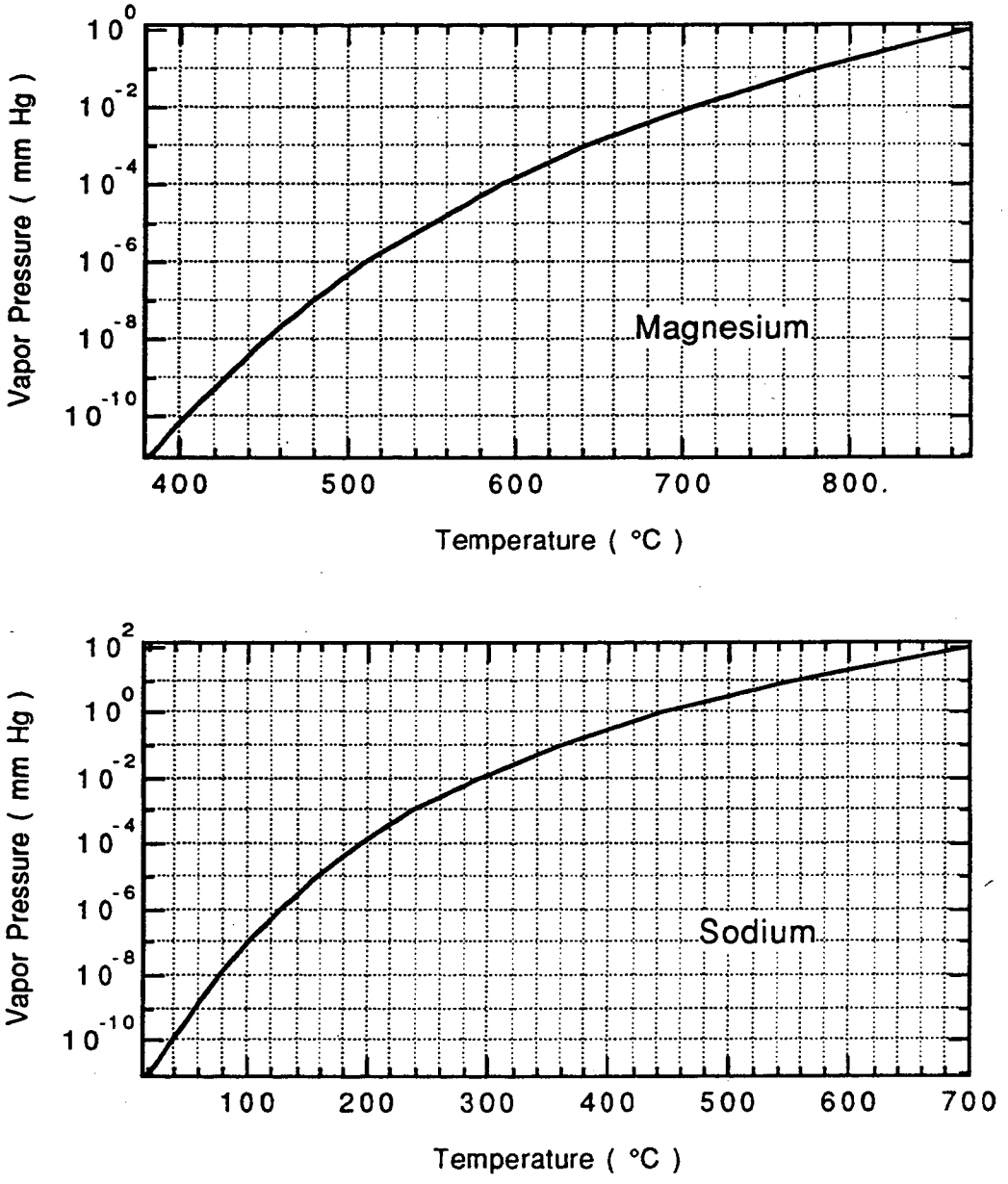

Figure 7.3 Vapor pressures of magnesium and sodium as functions of temperature [WE79].

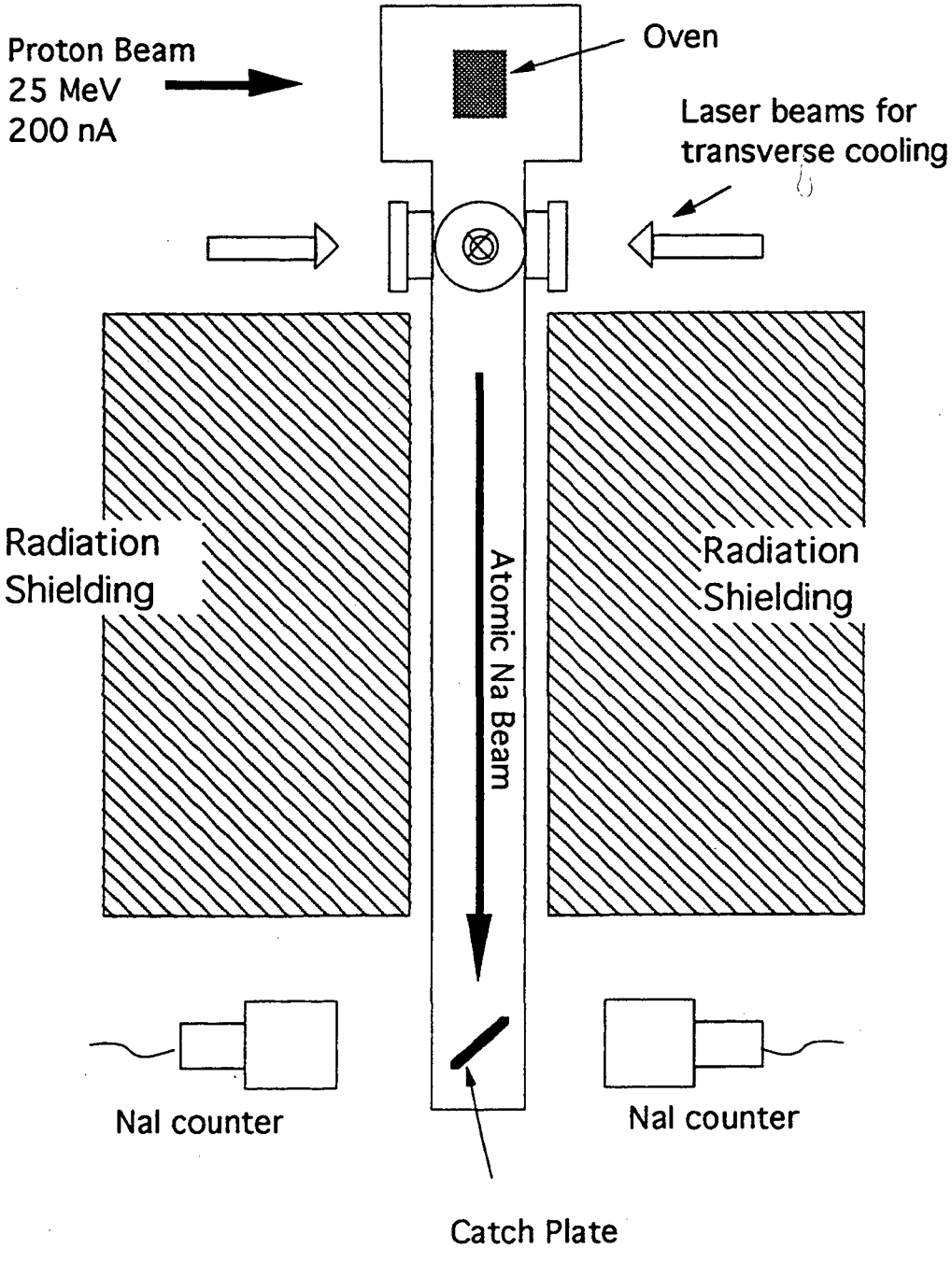

Figure 7.4 Setup for measuring the ^{21}Na atomic beam flux.

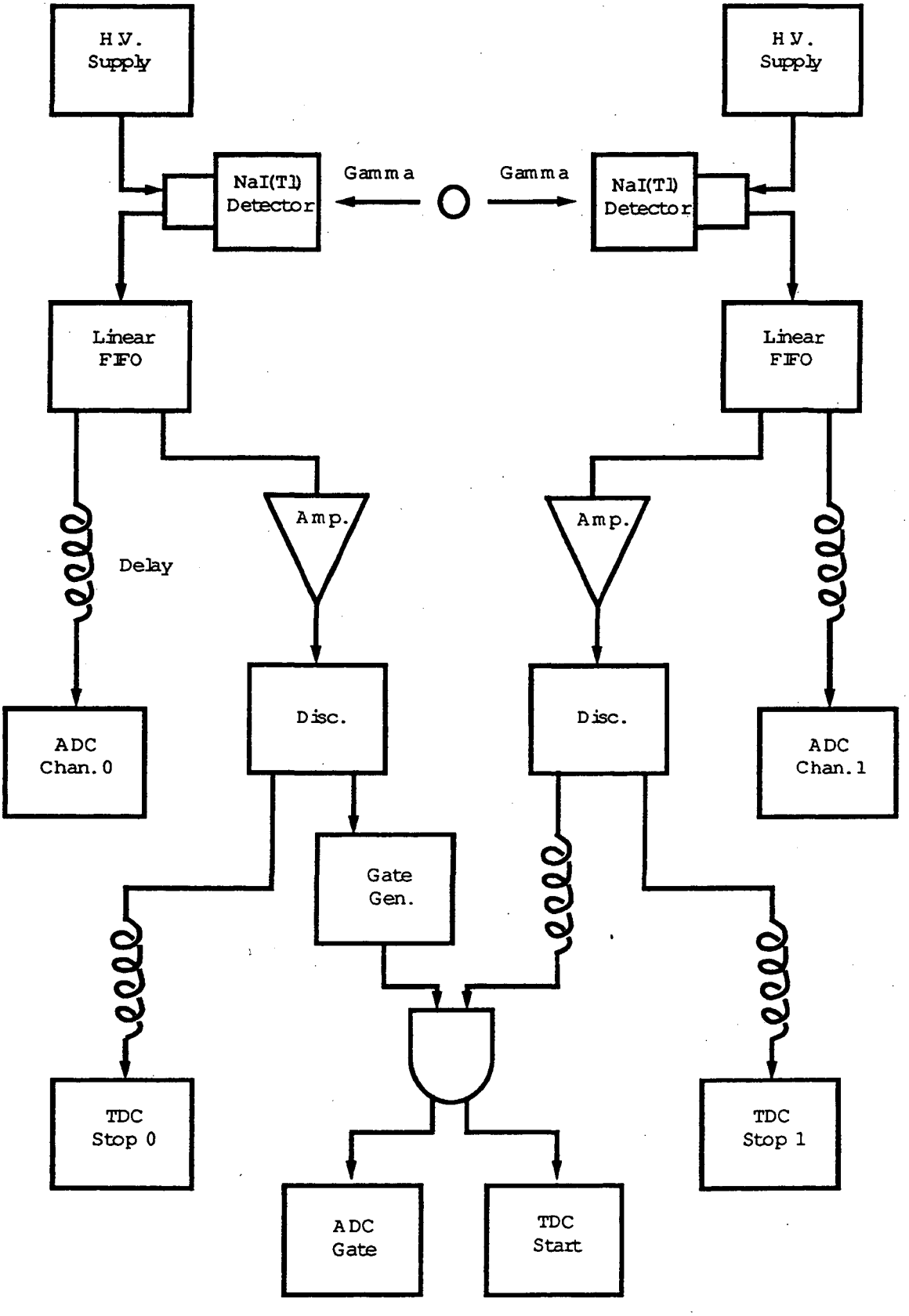

Figure 7.5 Block diagram of the counting electronics.

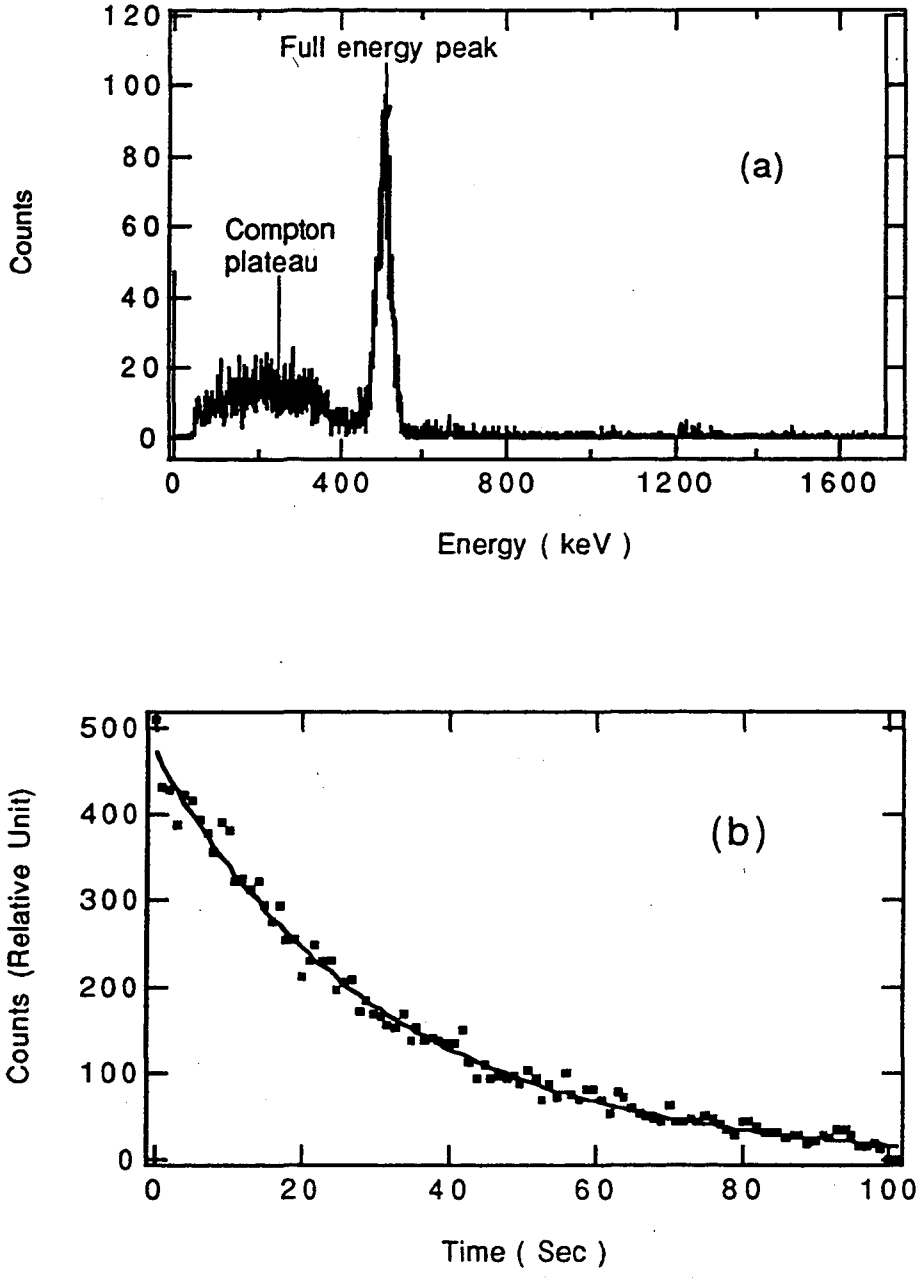

Figure 7.6 (a) A histogram of the signal pulse height from an NaI(Tl) detector during coincidence counting. Events are dominantly 511 keV photons; (b) Trigger rate (deadtime corrected) vs. time shows the decay of ^{21}Na. Fitting this curve gives half-life of 21.53 ± 0.56 sec, slightly less than the known half-life of ^{21}Na.

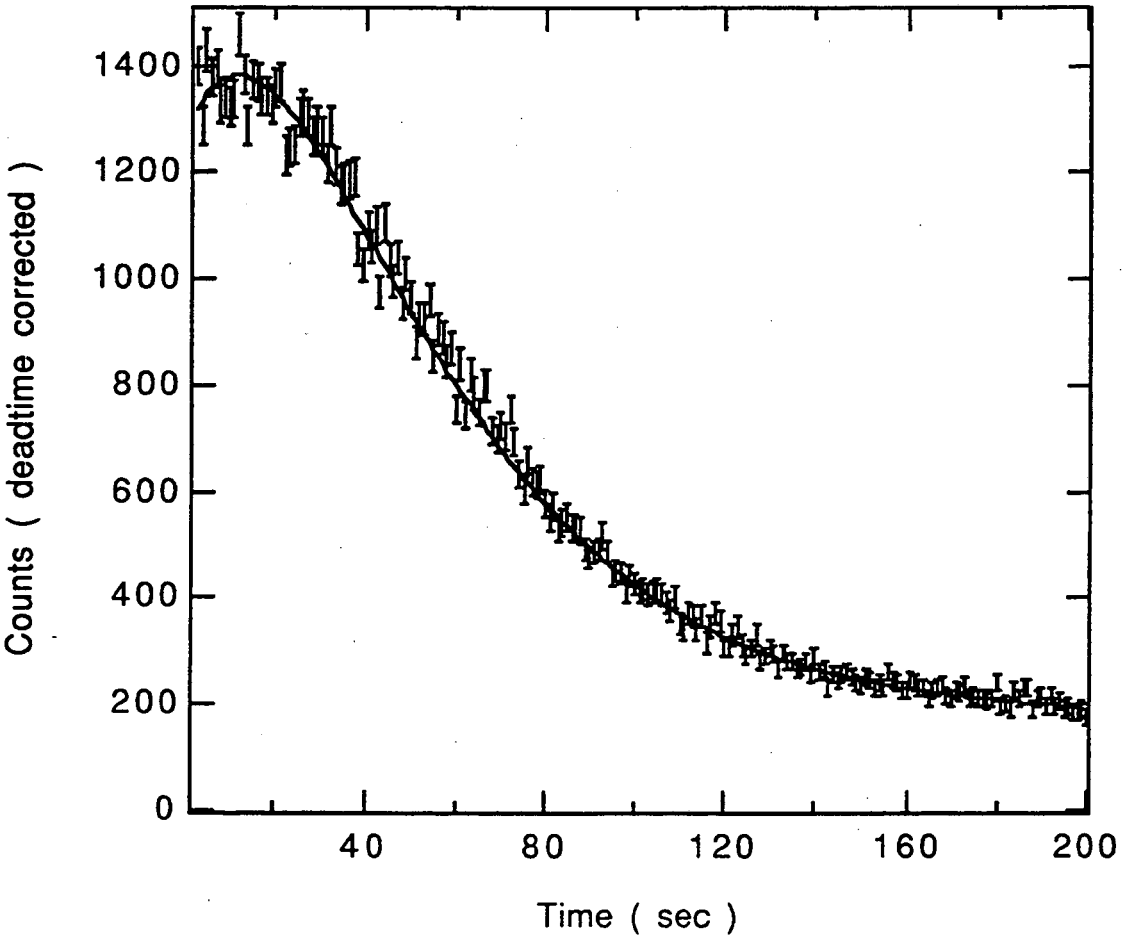

Figure 7.7 Decay rate (sum over 15 cycles) vs. time with the ^{21}Na atomic beam left on during the counting period. Proton beam is switched off at t = 0. A fit to equation 7.6 determines that $\sigma = (2.5 \pm 0.6) \times 10^{-6}$ 1/sec.

Chapter VIII

Trapping of ^{21}Na Atoms

We have already discussed techniques for trapping with high loading efficiency in Chapter VI and the techniques of producing a ^{21}Na atomic beam in Chapter VII. In this Chapter, we will consider how these techniques are combined to realize trapping of ^{21}Na atoms.

8.1 Apparatus

A schematic of the experimental setup is shown in Figure 8.1. Much of the arrangement is similar to the off-line apparatus described in Chapter VI. The main differences are listed below:

1) Oven. The oven loaded with magnesium was described in Section 7.3.1;

2) Ion pump. A 500 L/s Varian VacIon pump is installed right after the transverse cooling cube to improve the first stage of differential pumping;

3) Nuclear radiation shielding. The slowing solenoid fits into the hole on the accelerator radiation shielding wall described in Section 4.4.1. The solenoid itself also serves as additional radiation shielding;

4) Collector plate. A movable collector plate attached to a linear motion feed-through is installed after the trap along the atomic beamline with two NaI(Tl) counters installed on the side. The detection scheme is described in Section 4.4.2 and 4.4.3. Since the collector plate blocks the slowing laser beam, nuclear decay detection and laser trapping are conducted alternatively by moving the collector plate.

8.2 Laser Setup

The laser setup is similar to the one described in Chapter V. A few differences are listed below:

1) Isotope shift. The isotope shift of ^{21}Na is -1.6 GHz from ^{23}Na. In order to trap ^{21}Na atoms while using ^{23}Na atoms as frequency reference, an AOM (acousto-optic modulator) is used to compensate for this difference by shifting the frequency of light for saturation spectroscopy measurements.

2) Sideband frequency shift. Although the electron configuration and nuclear spin of ^{21}Na and ^{23}Na are the same (see Appendix A), the hyperfine separations differ for the two isotopes. A repumping sideband with a frequency shift of 1.8 GHz is generated by an EOM (electro-optic modulator). The ratio of the power in sideband to carrier is 1:4.

3) Optical Fiber. Due to limited available space, our laser room is 50 m (fiber distance) away from the Cave0 area where the trap is set up. Laser light is transferred by 3 μm diameter, single-mode polarization-preserving type optical fibers. About 40% of light can be transmitted. The output light is limited to about 150 mW due to stimulated Brillouin scattering [PA93, SM72]. In the process of stimulated Brillouin scattering, a photon of original frequency f_0 splits into a photon of frequency f_0-f_a and a phonon of frequency f_a. This process can be stimulated by a collision between the photon and a thermally excited phonon. Above a certain threshold of light power, this stimulated process is self-sustaining and the energy converted to phonons rise rapidly, which ultimately limit the laser power that a fiber can transmitted. To overcome this limit, two lines of optical fiber are used, one for transverse cooling, the other for trapping and slowing. Each fiber transmits about 100 mW of power. Since the trapping and slowing light share one optical fiber, each gets only 50 mW of light power. This is about 40% of the power used in the off-line setup described in Chapter VI.

4) Laser Beams. The slowing and trapping beams are expanded to 2.5 cm in diameter. The average intensity at the center of each beam is 12 mW/cm^2.

8.3 Pre-Run Tests

The ^{21}Na atomic beam is too weak to be used for laser beam alignment. Instead, ^{23}Na is loaded into the oven first for laser beam alignment and magnetic field fine tuning in order to reach the highest possible loading efficiency and the largest increase by transverse cooling. After everything is at the optimum condition, ^{23}Na in the oven is replaced by Mg for ^{21}Na production.

In pre-run tests, we obtained 5% of loading efficiency, less than the 20% loading efficiency we obtained on the off-line setup. This low efficiency is due to the inadequate laser power available at the cyclotron setup, noted in the last Section.

During pre-run tests, a 100°C oven produces enough ^{23}Na for alignment of the system. On the other hand, for ^{21}Na, the oven is operated at about 500°C in order to keep the ^{21}Na diffusion rate high (see Section 7.6). The higher oven temperature yields higher velocity atoms and a lower fraction of atoms are slowed due to the cut-off velocity imposed by the slow-down solenoid. In an atomic beam, the velocity distribution follows

$$I(v) = \frac{2I_0}{\alpha^4} v^3 \exp\left(-\frac{v^2}{\alpha^2}\right) , \tag{8.1}$$

where I(v)dv is the atomic beam intensity in a velocity interval between v and v+dv, I_0 is the total beam intensity, and $\alpha = \sqrt{2k_BT/m}$ is a characteristic velocity determined by oven temperature T and atomic mass m. The fraction of atoms with velocities lower than a cutoff velocity v_c is then given by

$$\int_0^{v_c} \frac{I(v)}{I_0} dv = 1 - \left(1 + \frac{v_c^2}{\alpha^2}\right) \exp\left(-\frac{v_c^2}{\alpha^2}\right) . \tag{8.2}$$

The largest magnetic field at one end of our slow-down solenoid is 1000 Gauss, corresponding to a cut-off velocity of 833 m/s (see equation 3.12). From equation 8.2, it can be calculated that 73% of atoms are slowed for ^{23}Na at 100°C, and only 31% are slowed for ^{21}Na at 500°C, so the 5% efficiency for ^{23}Na is reduced to 2% of loading efficiency for ^{21}Na traps.

8.4 Run Results

Figure 8.2 shows a picture of 4×10^3 trapped radioactive ^{21}Na atoms taken by the CCD camera.

We had three runs for trapping ^{21}Na. In one of the runs, only 600 atoms were trapped due to high background pressure (the oven chamber was exposed to air just before the run began). Listed below are results from the other two runs:

1) Peter Parity Run (12/10/93)

Proton current	200 nA
Oven temperature	500°C
^{21}Na atomic beam flux	3×10^3 sec^{-1}
Vacuum pressure	4×10^{-10} Torr
Loading lifetime	8.6 sec
Transverse cooling factor	5.4 times
Number of trapped atoms	3×10^3

2) Russia Run (12/19/93)

Proton current	1000 nA
Oven temperature	500°C
^{21}Na atomic beam flux	2×10^3 sec^{-1}
Vacuum pressure	4×10^{-10} Torr
Loading lifetime	5.5 sec
Transverse cooling factor	16 times
Number of trapped atoms	4×10^3

Here the atomic beam flux is measured by the nuclear decay method discussed in Section 7.4. The transverse cooling factor is the factor of increase in the number of trapped atoms by applying transverse cooling (see Section 6.9). During the pre-run tests of Peter Parity Run, this factor was 5, which agrees with the run result. However, during the pre-run tests of Russia Run, the factor was only 9, less than the run result. This factor varies from run to run due to the difference in laser beam alignment, but the fact that it changed during one run is unusual and hard to explain unless the alignment was disturbed. The ^{21}Na atomic beam flux was found to be 5 times lower in Russia Run than in the earlier PP Run. The proton current was then raised to 1 μ A to increase the atomic yield. The oven was examined after the run and it was found that the orifice was clear but most of the magnesium powder remained. The oven inserts were running at a lower temperature than expected due to a bad thermal contact.

The different loading times in the two runs can be caused by different background pressures. The vacuum pressure measurements in this range has an error of $\pm 1.5 \times 10^{-10}$ Torr. Another possible cause is collisions between trapped atoms and magnesium atoms in the beam. The cross-section of the collisional escape process can be estimated with the equation listed below,

$$\sigma = \frac{1}{\sqrt{2} \cdot n v \tau} \quad , \tag{8.3}$$

where σ is the cross-section, n is the density of the background gas, v is the average velocity of the background atoms and τ is the mean lifetime of a trap. Our measurements show that the lifetime of a trap is 30 sec in a vacuum of 1×10^{-10} Torr, which results in a cross-section of 2×10^{3} Å^{2}. Meanwhile, the oven output of magnesium atoms is determined to be 7×10^{16} sec^{-1} at 500°C (A calculation with the conductance of the oven orifice and magnesium vapor pressure results in an output of 2×10^{17} sec^{-1}), which

corresponds to a magnesium beam intensity of 7×10^{11} $sec^{-1}cm^{-2}$ at the trap. Assuming the collisional escape cross-section between sodium and magnesium atoms to be the same as the one between sodium and background gas atoms (He, H_2, H_2O, O_2, N_2, etc.), we calculated that the mean life-time due to collisions with atoms in the beam is 9 sec. This estimated result shows that the atomic beam is in the range of affecting the trap lifetime and would be a dominant factor if the oven temperature were higher.

Figure 8.3 shows the decay and loading of trapped ^{21}Na atoms taken during Russia Run. Here the transverse cooling is used as an atomic beam valve since it changes the number of trapped atoms by an order of magnitude.

8.5 Future Improvements

These initial results demonstrated the possibility of trapping short-lived radioactive atoms. The number is still two orders of magnitude less than enough to perform the beta-asymmetry measurements (see Section 2.1.6). Several aspects have been discussed among our group to improve the number.

1) More laser light power. The 60% loss of power during light transport will be avoided by eliminating the optical fiber and moving the laser next to the trapping area. A 20% trap loading efficiency has been demonstrated in our test setup with ^{23}Na atoms from a 100°C oven, this corresponds to 8% efficiency for ^{21}Na atoms from a 500°C oven (see Section 8.3), so the number of trapped atoms is expected to increase by a factor of 4 with this arrangement.

2) A new oven design. In addition to a more reliable oven, a more sophisticated oven is needed to absorb a more intense proton beam and to run longer at higher temperature. A design of oven with two cavities at different temperatures is proposed. Sodium atoms can migrate out of magnesium grains in the high temperature region and magnesium can condense in low temperature region to avoid disturbing trapped atoms (see Section 8,4). The improvements and possible problems brought about by higher temperature have been discussed in Section 7.6. An order of magnitude of increase in atomic yield generated by a more intense proton beam (a few micro amps) is likely.

3) Lower background pressure. Cold LN_2 baffles can be set up around the trap to provide more pumping speed. If a vacuum of 2×10^{-11} Torr is achieved in the trapping chamber, the trap loading time can be extended to the nuclear decay lifetime: 30 sec for ^{21}Na. That increases the number of trapped atoms for at least a factor of 3. Note this effect has to be coordinated with an improvement of the oven that reduce the trap loss due to collisions with atoms in the magnesium beams.

4) A more sophisticated transverse cooling scheme. Both reference [SH90] and [HO93] reported results of transverse cooling with curved wave-fronts. A larger capture velocity [see Section 6.9] is demonstrated. Near the oven orifice, atoms inside an initial divergence angle of 0.1 rad are transversely cooled. The current ^{21}Na trap is formed by 2.5 cm diameter laser beams, 210 cm away from the oven orifice. When applied to the ^{21}Na atom trap, a two dimensional cooling of this type is expected to increase the atomic beam intensity at the trap region by about a factor of 70, that is 4 to 5 times better than the currently applied simple transverse cooling scheme.

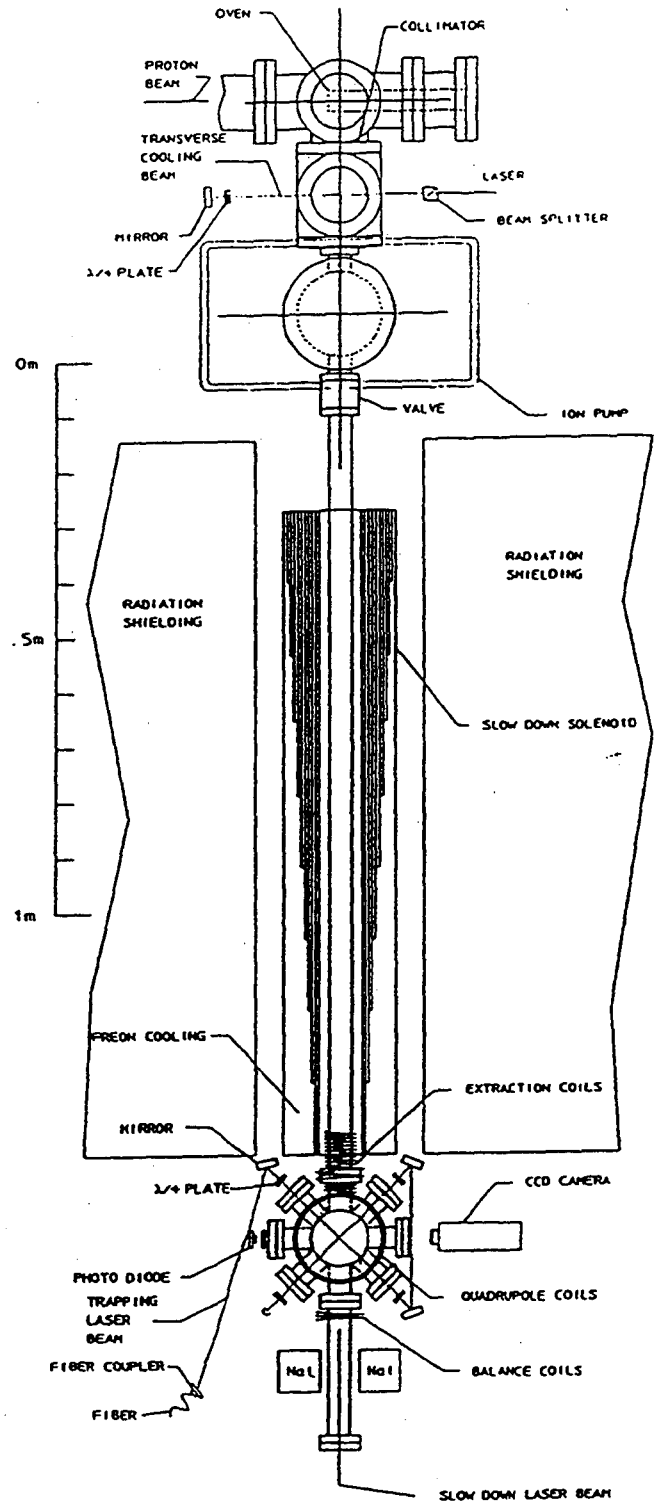

Figure 8.1 Plan view of the apparatus for trapping ^{21}Na atoms.

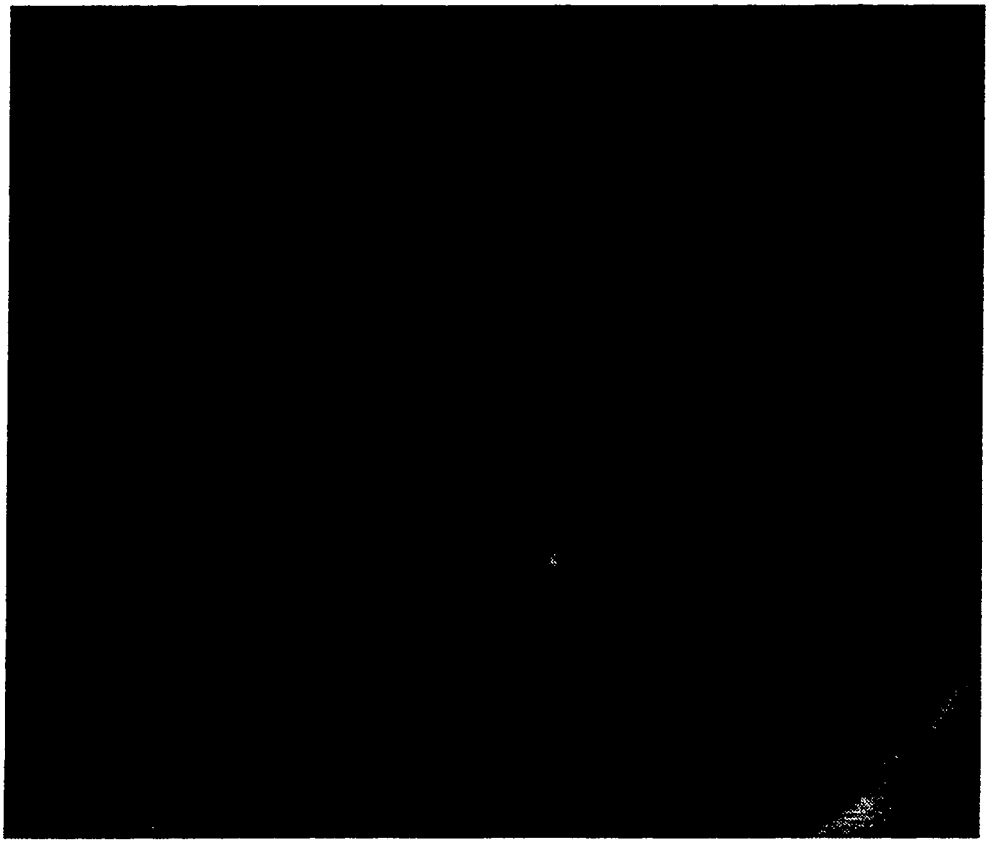

Figure 8.2 One frame recorded by the CCD camera showing the optical fluorescence from 4 x 10^3 trapped ^{21}Na atoms. The bright areas at the lower corners are due to scattered light off a viewport.

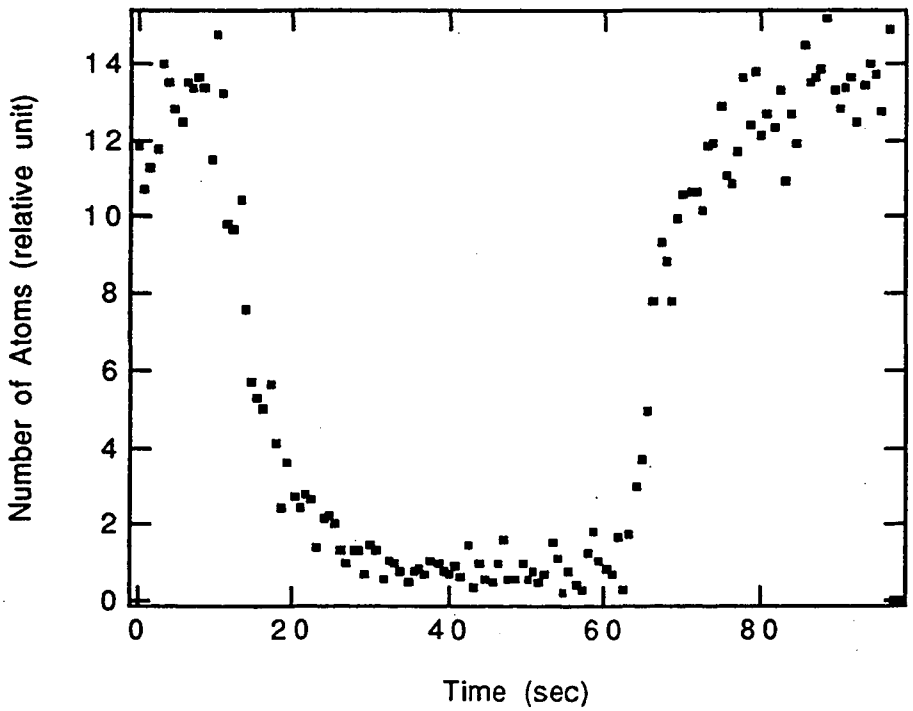

Figure 8.3 Time spectrum of the optical fluorescence from trapped ^{21}Na atoms as the transverse cooling laser beams are turned off and on. The mean loading time is 5.4±0.5 sec and mean decay time is 5.3±0.3 sec.

Chapter IX

Three Types of Magneto-Optical Trap

9.1 Historical Background

In the original paper [RA87] reporting the first MOT of sodium, traps were found with two different laser frequency settings. It was noted that

> "With a fixed 1712.4-MHz optical sideband splitting, the laser frequencies were tuned to the red of the F=2-3 and 1-2 transitions or the F=2-2 and 1-0 transitions. The former tuning produced a much more compact ball of atoms than the latter."

Later on, they were named Type I (2-3,1-2) and Type II (2-2,1-0) trap. In general, Type I and Type II traps have about the same brightness, but the diameter of Type II traps are about twice that of Type I traps under optimum conditions of each type.

In a Type I trap, trapping light is tuned 5 - 20 MHz below the resonance of F=2 to F'=3 transition (see Fig 9.1). This transition is called a cycling transition since an atom in F'=3 state can only spontaneously decay back to F=2 state because the selection rules of E1 transitions require $\Delta F = 0$ or 1 (see Appendix B), which enables single frequency light to interact with the atom continuously. While this transition is closed to spontaneous decay,

it is possible for an atom to be excited to F'=2 state through off-resonance absorption. In fact, the probability of exciting an atom to F'=2 state by a 10 mW/cm^2 laser beam and 15 MHz detuned from F=2 to F'=3 resonance is 10%. Once an atom is at F'=2 state, it can spontaneously decay to the F=1 state of the ground level and cease further interaction with the light. In order to provide continuous trapping force, light at the proper frequency, obtained with a laser sideband, is used to pump the atom back to F=2 state.

Type I trap was well understood and predicted before experimentally demonstrated. On the other hand, the Type II trap was miss-identified [MA93] as we discovered from some simple measurements described in this chapter [SH94].

9.2 The Type II Trap

In order to understand the true nature of the Type II trap, we investigate whether atoms in the Type II trap spend more time in F=1 or F=2 ground level state. This tells us which one, the carrier light or the sideband light, is trapping light, and which one is pumping light. Three methods are used:

1) The usual trap is set up, with sideband light on each trapping beam. A strong single frequency laser beam at the carrier frequency (with no sideband) is directed to the trap. We observe that when the disturbing beam is near the transitions from F=1 to excited level states, Type II trap is destroyed while Type I trap is only slightly disturbed; when the disturbing beam is near the transitions from F=2 to excited level states, Type I trap is destroyed while Type II trap is only slightly disturbed.

2) This procedure (suggested to us by Dr. Mara Prentiss) is based on the fact that trapping light has to be sent into a trap from six directions surrounding the trap, but re-pumping light is not sensitive to direction, a beam in any direction will do. In this experiment, a sideband is generated only on a single counter-propagating pair of beams along one direction. With 1712 MHz side-band splitting, when the carrier frequency is scanned for 150 MHz covering the range from F=1 state to all hyperfine states of the excited level, we observed Type II trap only; and when carrier frequency scan range covered transitions from F=2 state, only Type I trap was observed.

3) This method relies on the fact that trapping light frequency has to be detuned below the trapping transition while pumping light frequency only needs to be close to a pumping transition, both below and above. Figure 9.2 shows the result of four scans of laser frequency conducted with different side-band frequency splitting. The carrier frequency, whose position is indicated in the saturation absorption spectrum, covers the range from F=2 to all hyperfine states in the excited level. Two traps are observed in each scan. The one at lower frequency end is Type II trap, the other one is Type I trap. It is clear that the Type I trap does not change its position among the four scans. The high frequency cutoff is always at 5 MHz below the resonance of F=2 to F'=3. On the other hand, the Type II trap shifts position from scan to scan. This shows that for the Type I traps, the carrier frequency band of the laser is the trapping light; and for the Type II traps, carrier light does the re-pumping work. Furthermore, from calculation (see Fig 9.4), the sideband frequency is always in the range from 40 - 10 MHz below the resonance of F=1 to F'=1 transition when a Type II trap occurs, i.e. from 24 MHz below to 6 MHz above the resonance of F=1 to F=0 transition.

The evidence discussed above points to the explanation that for a Type II trap, the trapping transition is F=1 to F'=1, while the pumping transition can be either F=2 to F'=2

or F=2 to F'=1. Although F=1 to F'=1 is not a cycling transition (see Appendix B), it is "quasi-closed" since when an atom in F'=1 state spontaneously decay, it decays to the F=1 states with 80% probability.

9.3 The Type III Trap

A trap with a different frequency setting was discovered accidentally while we were investigating Type I and II traps. Following convention, we call it Type III (see Fig 9.3).

Figure 9.2 contains two scans of laser frequency with different sideband frequency shifts The Type I trap is in the same place in the two scans, which means that F=2 to F'=3 is the trapping transition. Type II and Type III traps come at different places in each scan. A simple calculation verifies that the positions of these two traps are fixed by the sideband frequency. We found that F=1 to F'=2 is the trapping transition for Type III traps and either F=2 to F'=1 or F=2 to F'=2 can be its re-pumping transition.

From the F'=2 state, an atom has approximately equal chances to spontaneously decay to either the F=1 or F=2 states of the ground level, which increases the demand for re-pumping, reduces the cycling rate on the F=1 to F'=2 trapping transition and causes the trap potential to be shallow. Its number of atoms is an order of magnitude lower than the other two types of traps when a trap of each type is set up to its own optimum condition.

The ability to observe the Type III trap is a consequence of the high loading efficiency of our system. Our setup generated a dense slow atom environment to feed this shallow trap. When a trap is loaded with an inefficient method (e.g. loading from vapor), simply

increasing the number of slow atoms with the total atomic density increased at the same rate makes the trap impossible due to the high collisional loss.

The functions of trapping transition and pumping transition do not have to be exclusive. Pumping transition is denoted as such because its main function is pumping, but it can also provide trapping force, and vise versa.

9.4 Interpretation of the three types of MOT

In an effort to understand the three types of MOT , a one-dimensional model is constructed to calculate the trapping and cooling effects of light. In particularly, the capture velocities of traps with light of various frequencies are calculated.

9.4.1 A simple one-dimensional model

In our one-dimensional model, the atomic motion is confined to the z-axis while the setup of laser beams and magnetic field is the same as illustrated in Figure 1.1. Three pairs of circularly polarized laser beams counter-propagate along x,y,z-axis respectively. The pair of laser beams along z-axis provide force on atoms, while the other two pairs only affect the population distribution over various atomic states and the velocity diffusion processes. Along the z-axis, a magnetic field has positive constant gradient, $B = \frac{dB}{dz} \cdot z, \left(\frac{dB}{dz} > 0\right)$, B=0 at the center (z=0) where atoms are trapped.

Appendix B shows the relevant atomic levels. The ground level ($3S_{1/2}$) has 8 Zeeman states in total and the excited level ($3P_{3/2}$) has 16. Our static model assumes that the atomic population distribution over these 24 states is in equilibrium under the light and magnetic field conditions at the position of the atom. The population distribution can then be calculated with static optical Bloch equations [CO90]. Two more approximations are made to simplify the calculation: first, the phase of each beam in x or y direction is averaged over the length of a wavelength; second, in the density matrix, the terms that describe coherence between two excited level states or two ground level states are neglected. The simplified optical Bloch equations can be written as

$$\sigma_{ee} = \sum_{g}\left(\sigma_{gg} - \sigma_{ee}\right)\cdot\left[\frac{\frac{I}{4I_s}Y_{eg}^2\langle e|g,1,-1\rangle}{\left(\frac{\omega_e-\omega_g-\omega_L-kv}{\Gamma}\right)^2+\frac{1}{4}} + \frac{\frac{I}{4I_s}Y_{eg}^2\langle e|g,1,+1\rangle}{\left(\frac{\omega_e-\omega_g-\omega_L+kv}{\Gamma}\right)^2+\frac{1}{4}} + \frac{\frac{I}{4I_s}Y_{eg}^2\langle e|g,1,0\rangle}{\left(\frac{\omega_e-\omega_g-\omega_L}{\Gamma}\right)^2+\frac{1}{4}}\right], \tag{9.1}$$

$$\sum_{q=-1}^{+1}\sigma_{ee}Y_{eg}^2\langle e|g,1,q\rangle^2=\sum_e(\sigma_{gg}-\sigma_{ee})\cdot\left[\frac{\frac{I}{4I_s}Y_{eg}^2\langle e|g,1,-1\rangle}{\left(\frac{\omega_e-\omega_g-\omega_L-kv}{\Gamma}\right)^2+\frac{1}{4}}+\frac{\frac{I}{4I_s}Y_{eg}^2\langle e|g,1,+1\rangle}{\left(\frac{\omega_e-\omega_g-\omega_L+kv}{\Gamma}\right)^2+\frac{1}{4}}+\frac{\frac{I}{4I_s}Y_{eg}^2\langle e|g,1,0\rangle}{\left(\frac{\omega_e-\omega_g-\omega_L}{\Gamma}\right)^2+\frac{1}{4}}\right], \quad (9.2)$$

with a normalization condition

$$\sum_e\sigma_{ee}+\sum_g\sigma_{gg}=1 \quad . \quad (9.3)$$

In these equations, σ_{ee} and σ_{gg} are the diagonal terms of the density matrix, which represent the population on each state. I is the light intensity of each laser beam, the intensity of light of carrier frequency is used when an F=2 ground level state is involved and the intensity of light of sideband frequency is used when an F=1 ground level state is involved. I_s = 6 mW/cm^2 is the saturation intensity of the F=2, m_F=+2 to F'=3, m_F=+3 transition. Y_{eg}^2 is the relative oscillator strength that is proportional to the square of the reduced matrix $\langle e\|d\|g\rangle^2$, Y_{eg}^2=1 for F=2 to F=3 transitions. ω_e, ω_g, ω_L represent the frequency of the excited state, the ground state and light, respectively. Here kv is the Doppler shift of light frequency, which is 2π x 1.7 MHz for 1 m/s of atomic velocity. Γ = 2π x 10 MHz is the natural linewidth. The population distribution can be calculated by solving these equations numerically.

Each photon absorption or emission changes the momentum of an atom by $\Delta P = \frac{h}{\lambda}$. The force on an atom can be calculated as

$$F = \frac{h\Gamma}{\lambda} \cdot \sum_{e,g} \left(\sigma_{gg} - \sigma_{ee}\right) \cdot \left[\frac{\frac{I}{8I_s} Y_{eg}^2 \langle e|g,1,-1\rangle}{\left(\frac{\omega_e - \omega_g - \omega_L - kv}{\Gamma}\right)^2 + \frac{1}{4}} - \frac{\frac{I}{8I_s} Y_{eg}^2 \langle e|g,1,+1\rangle}{\left(\frac{\omega_e - \omega_g - \omega_L + kv}{\Gamma}\right)^2 + \frac{1}{4}} \right] . \tag{9.4}$$

With a given experimental condition, this force depends both on position and velocity of an atom. Clearly, in order to establish a stable trap at the center, the force near the center has to be in the form of

$$F = -kx - av \quad , k > 0 \text{ and } a > 0 \ , \tag{9.5}$$

which provides cooling as well as trapping mechanism. Figure 9.5 shows a numerical example of the calculated force as a function of position and velocity, a stable trap is expected with the given condition because equation 9.5 is satisfied.

9.4.2 Calculation of the capture velocity

Although equation 9.5 tests whether a stable trap can be formed, it can not be used to calculate the number of atoms that can be loaded into the trap. In order to obtain this

information, reference [MO90] examined the loading and loss mechanisms of traps. Since the atom reservoir outside a trap is at equilibrium, the loading rate, i.e. the number of atoms that are loaded into the trap in unit time, is a constant. On the other hand, the main loss mechanism at low density of trapped atoms ($< 10^9$ 1/cm^3) is due to collisions between trapped atoms and background thermal atoms (see Chapter 10), with the collisional loss rate proportional to the number of trapped atoms. The time evolution of the number is governed by equation:

$$\frac{dn(t)}{dt} = R - \frac{n(t)}{\tau} \quad , \tag{9.6}$$

where R is the constant loading rate, $1/\tau = n_b \sigma v$ is the loss rate where n_b is the density of background thermal atoms, σ is the collisional cross-section and v is the averaged relative velocity. From equation 9.6, we obtain $n(t) = n_s(1 - \exp(-t/\tau))$, with steady-state number $n_s = Rt$. The loading rate R is directly related with a quantity called "capture velocity", v_{cap}. Atoms entering the trap region with velocity less than the capture velocity are captured by the trap, while atoms entering the trap region with higher velocities escape. Therefore, the loading rate R is just the rate of atoms entering the trapping region with velocities lower than v_{cap}, which can be calculated as

$$R = \frac{An}{4} \int_{v=0}^{v_{cap}} v \cdot \rho(v) \cdot 4\pi v^2 dv \quad , \tag{9.7}$$

where A is surface area of the trap region, which can be assumed to be a sphere with the same diameter as the trapping laser beams; n is the atomic density; and r(v) is the normalized velocity distribution in the atomic reservoir. In a cell where atoms follow the Maxwell-Boltzmann distribution, R can be calculated as in the following equation with an approximation for v_{cap} much less than the average velocity of the sample,

$$R \approx \frac{An}{4} \cdot \pi \left(\frac{m}{2\pi k_B T} \right)^{3/2} \cdot v_{cap}^4 \quad , \tag{9.8}$$

where m is the mass of an atom, T is the temperature of the sample. When loading a trap with atoms from a slowed beam, as described in previous chapters, the velocity distribution in the reservoir is more complicated, the average velocity being about 5-10 m/s.

Capture velocities of various light frequencies are calculated with our one dimensional model. Specifically, we applied experimental conditions with which the scans with three types of MOT (Figure 9.3) are obtained. These conditions are listed below:

Laser beam diameter	1.0 cm
Sideband frequency separation	1774 MHz, 1792 MHz
Intensity of light of carrier frequency	10 mW/cm^2
Intensity of light of sideband	10 mW/cm^2
Magnetic field gradient	20 Gauss/cm

This calculation is conducted by numerically simulating the capturing processes. It starts by injecting an atom at the center with a velocity v_{ini}. The acceleration due to the light force can be calculated with Equation 9.4, and the evolution of the position and velocity of the atom is traced at a small time step of 1.6×10^{-6} sec. The criteria for an atom to be captured at (z,v) is listed below:

a) $|v| < 1$ m/s , the velocity is less than 1 m/s;

b) -0.5 cm $< z < +0.5$ cm , the atom is within the trapping region;

c) The force at (z,v) satisfies Equation 9.5.

The capture velocity is equal to the largest possible v_{ini} with which an atom can be captured.

Figure 9.6 shows the calculated capture velocities in two frequency scans with experimental conditions the same as the measured ones shown in Figure 9.3. Notice that Figure 9.3 shows the measured fluorescence power instead of the number of trapped atoms in frequency scans. The relation of these two quantities is shown in the equation below:

$$P_{fluo} = N \cdot f \cdot \Gamma \cdot (\hbar\omega) \cdot \eta \quad , \tag{9.9}$$

where P_{fluo} is the fluorescence power measured by a photo-diode, N is the number of trapped atoms, f is the fraction of population in the excited level, Γ is the natural linewidth, $\hbar\omega$ is the energy of a single photon, and η is the light detection efficiency that includes the solid angle factor. Since Γ, $\hbar\omega$, and η are approximately constant in the scanned frequency range of 200 MHz, the relative change of the number of trapped atoms can be calculated by deviding the fluorescence power by the fraction of population in the excited level, which can be calculated by solving the optical Block equations (Equation 9.1 and 9.2). The resulting number of trapped atoms in the two frequency scans is shown in Figure 9.7.

According to the simulated frequency scan of SF=1792 MHz, a stable MOT (Type IV ?) is expected in the detuning range of -60 MHz to -69 MHz. However, the capture velocity is only 5 m/s, comparing with the 18 m/s for the strong Type I trap, so loading rate is rather low and the signal is expected to be small. Another unobserved feature is the sharp peak at detuning of -79 MHz, this might appear only in one dimensional on-axis models.

The capture conditions of off-axis positions differ from the on-axis ones, and the peak may be washed out.

In conclusion, the simple one dimensional model is partially successful in explaining the observed fluorescence signal from trapped atoms with various laser frequencies. More sophisticated models should include off-axis points [LI92], and ultimately, atomic motion in three dimensions.

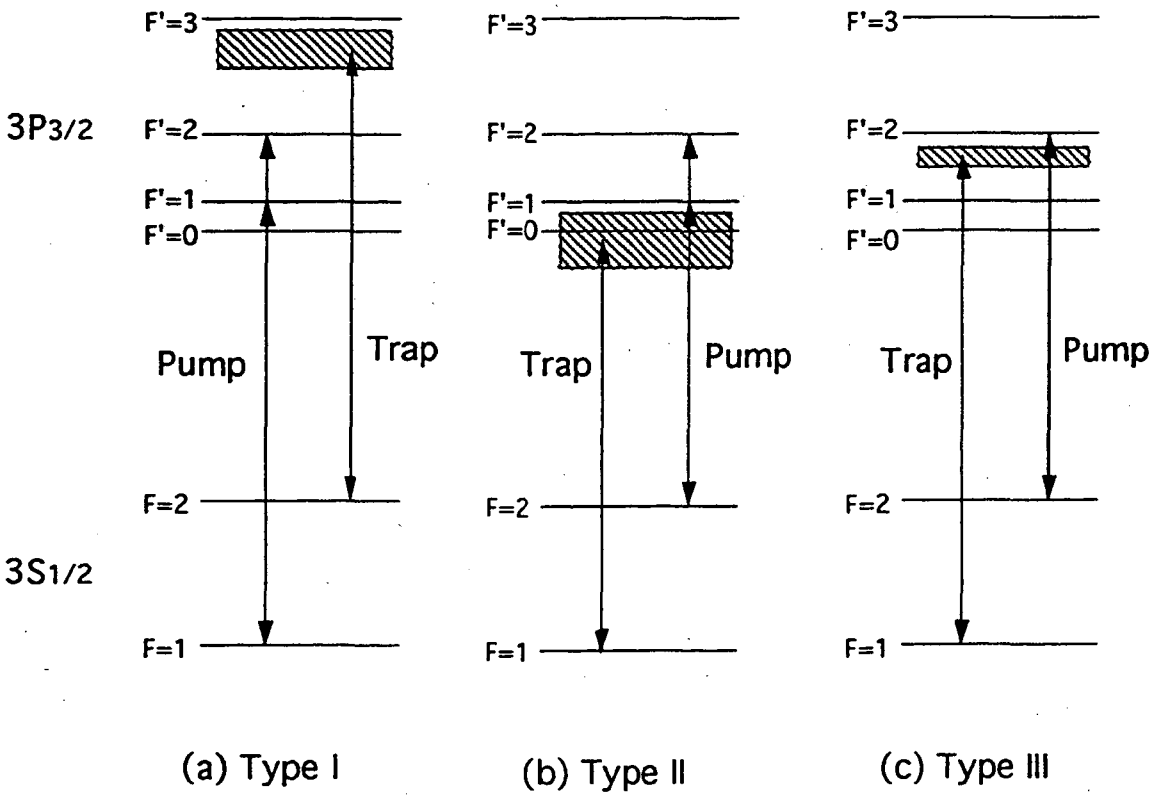

Figure 9.1 Three types of MOT of sodium. Shaded area indicates the tunable range of the trapping light frequency. Trapping and re-pumping transitions for each type of traps are marked in the figure and listed in the table below.

Type of MOT	Trapping Transition	Re-pumping Transition
Type I	F=2 to F'=3	F=1 to F'=1, F=1 to F'=2
Type II	F=1 to F'=1	F=2 to F'=1, F=2 to F'=2
Type III	F=1 to F'=2	F=2 to F'=1, F=2 to F'=2

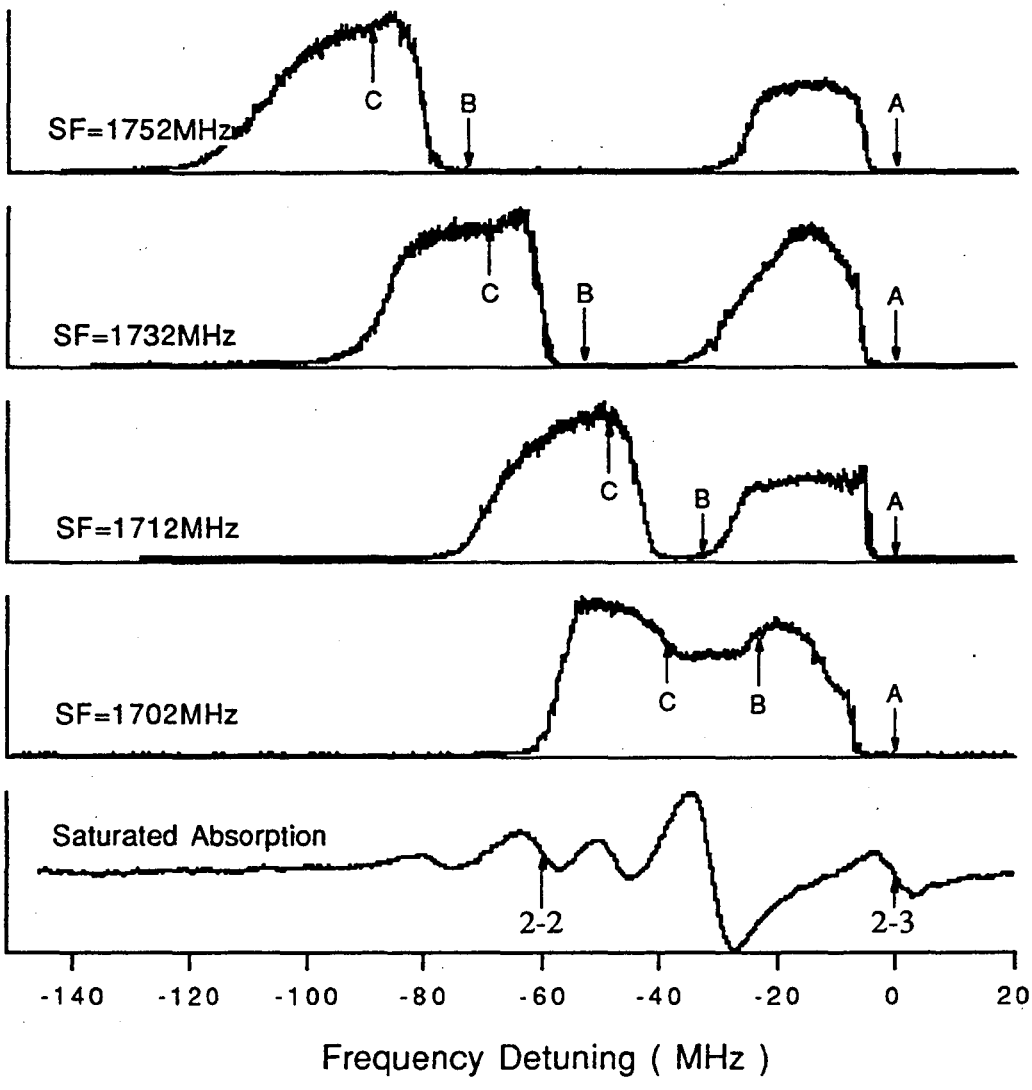

Figure 9.2 Frequency scans of the laser trap fluorescence in the region of resonances from the F = 2 ground level to the various excited state hyperfine sublevels. The four upper traces correspond to different repumping sideband frequencies (SF). The lower trace is the fluorescence signal from a saturated absorption cell. Resonance transition features are indicated by the arrows. The arrows indicated by the letter A is at the F=2 to F'=3 resonance frequency in each scan (A is at the zero detuning point). The letter B indicates the detuning of the carrier frequency from the F=2 to F'=3 transition when sideband is at F=1 to F'=1 resonance in each scan; and C is the corresponding point for the F=1 to F'=0 resonance.

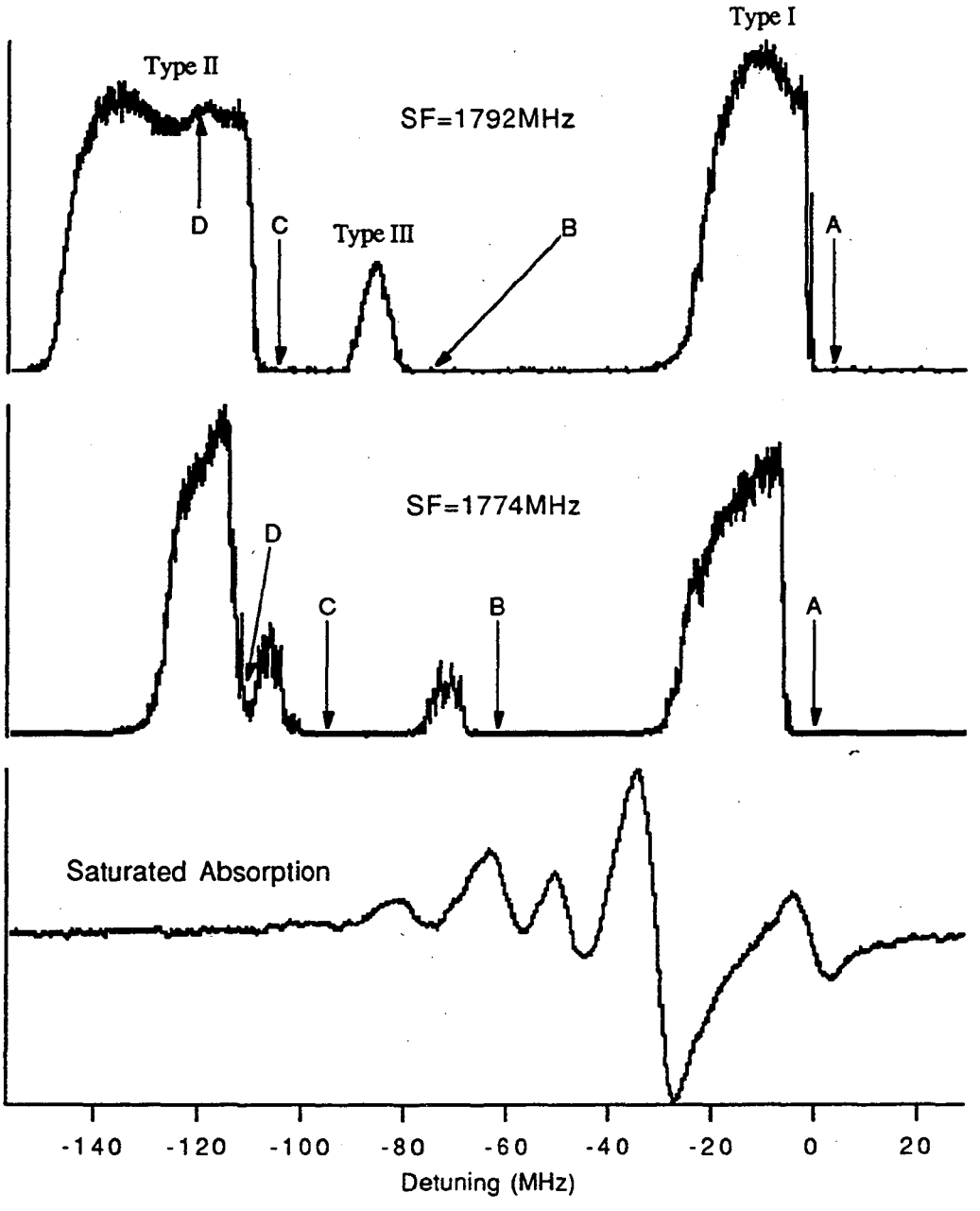

Figure 9.3 Frequency scans of the fluorescence from trapped atoms show three types MOT. The two upper traces correspond to different repumping sideband frequencies (SF). The lower trace is the saturated absorption signal from a sodium cell. The arrows indicated by the letter A is at the F=2 to F'=3 resonance frequency in each scan. The letter B indicates the detuning of the carrier frequency from the F=2 to F'=3 transition when sideband is at F=1 to F'=2 resonance in each scan; C and D are the corresponding points for the F=1 to F'=1 and F=1 to F'=0 resonances respectively.

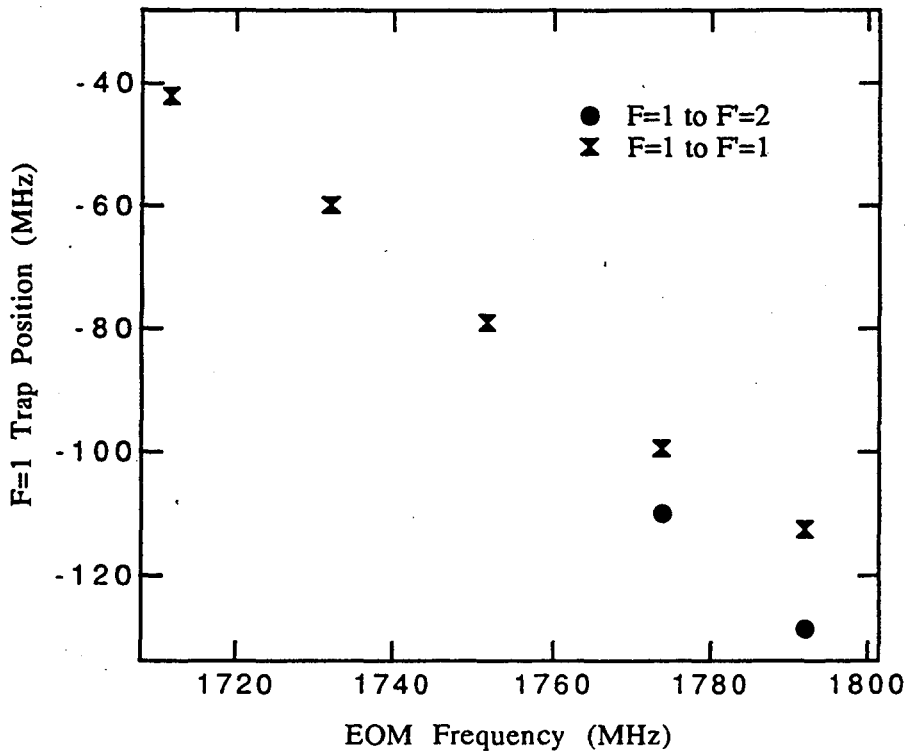

Figure 9.4 The frequency (relative to F=2 to F'=3 transition) at which traps form vs. EOM frequency. The observed dependence on EOM frequency is the evidence that the trapping force for Type II and III traps comes from the laser light of sideband frequency, which indicate the mechanisms shown in Figure 9.1.

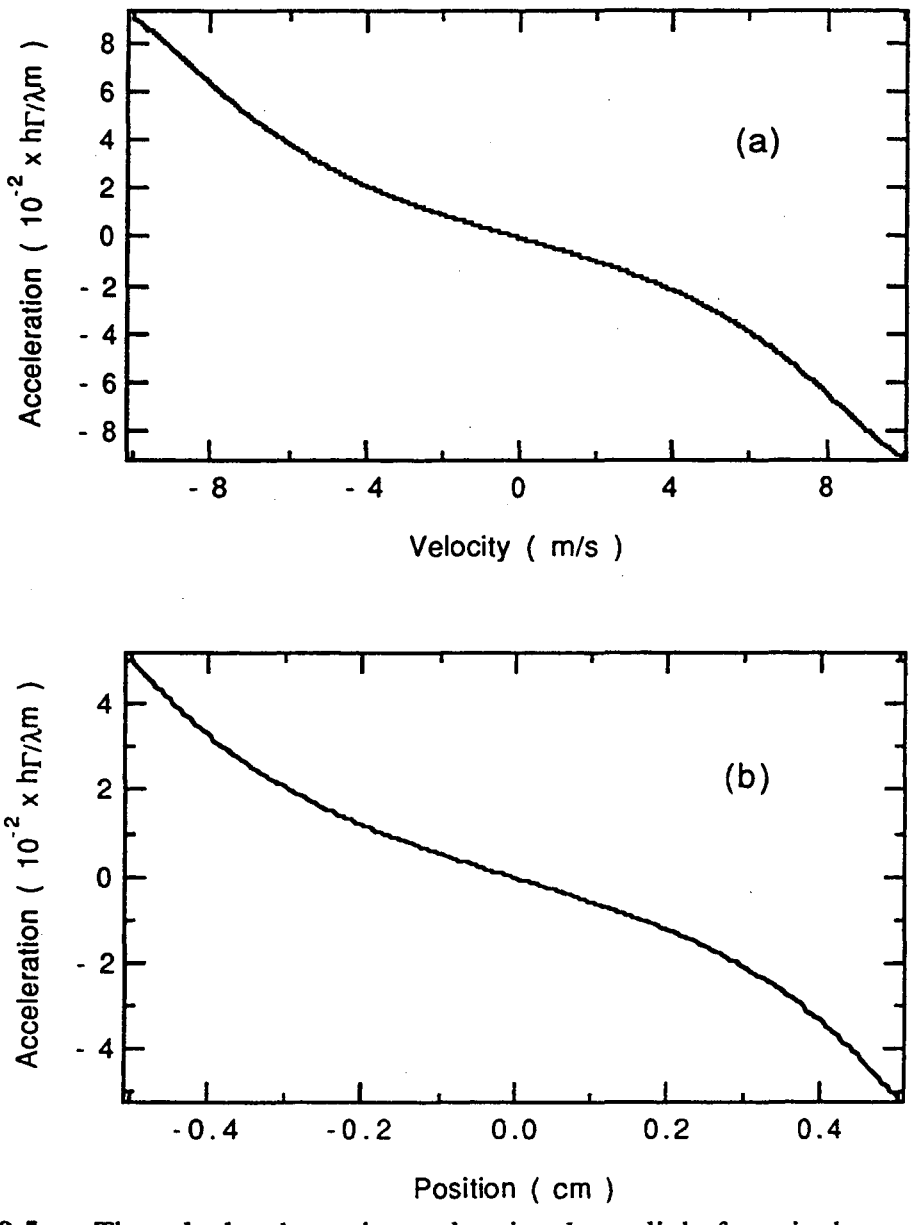

Figure 9.5 The calculated atomic acceleration due to light force in the one dimensional model. Here the intensity of light of both carrier and sideband is 10 mW/cm^2, the carrier is detuned 20 MHz below the resonance of F=2 to F'=3, the sideband is 1774 MHz away from the carrier, dB/dz = 20 Gauss/cm. In (a), acceleration at z=0 is shown as a function of velocity, its unit is $10^{-2} \times \frac{h\Gamma}{\lambda m} = 2 \times 10^4$ m/s^2; In (b), acceleration at v=0 is shown as a function of position z. Since the gradient of acceleration in both graph is negative, both cooling and trapping mechanisms are present, a stable trap is expected with current condition.

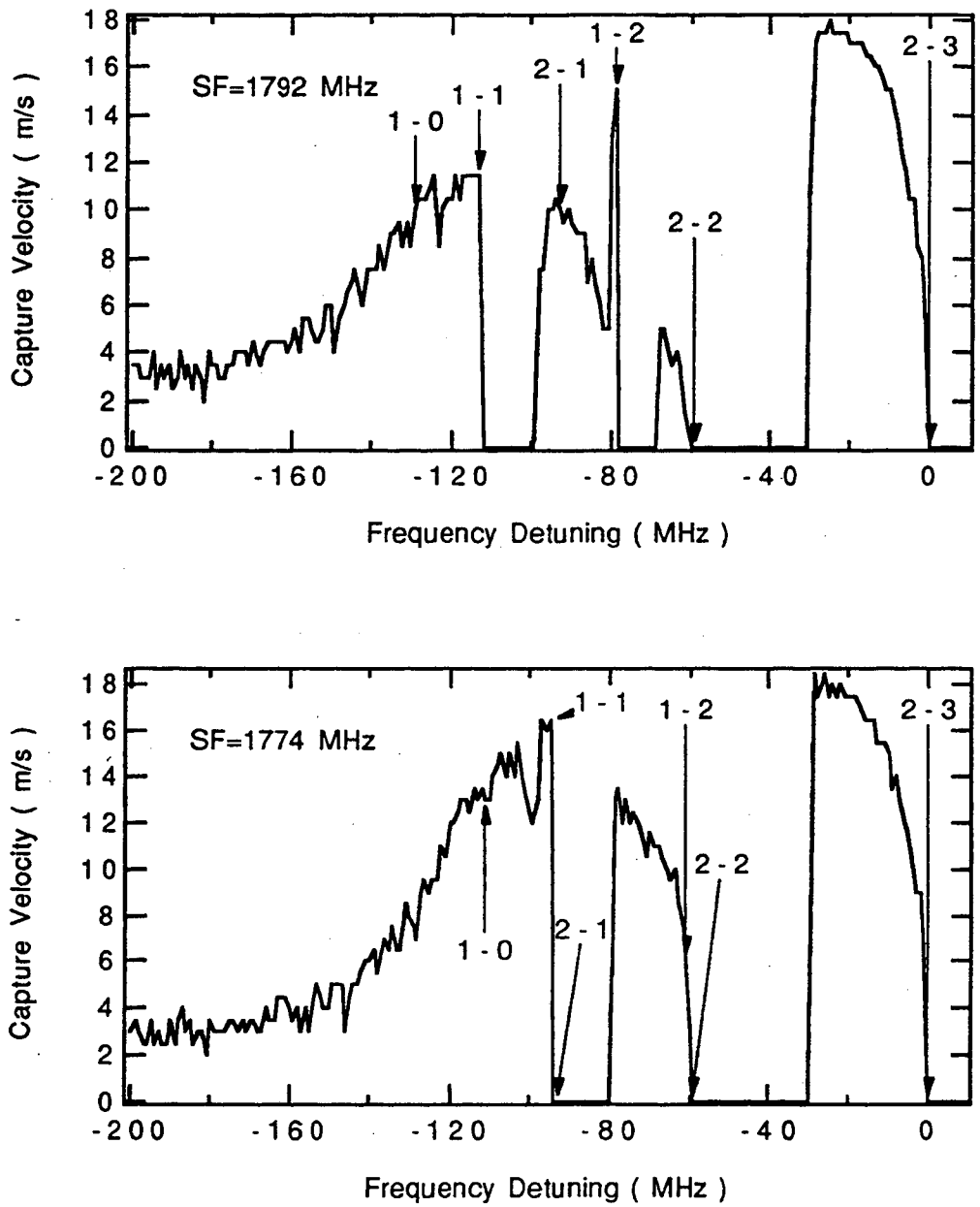

Figure 9.6 The simulated frequency scans of the capture velocity for 1792 MHz and 1774 MHz respectively. The experimental conditions under which the simulations are conducted are listed in Section 9.4.2. The transition resonances are marked with arrows.

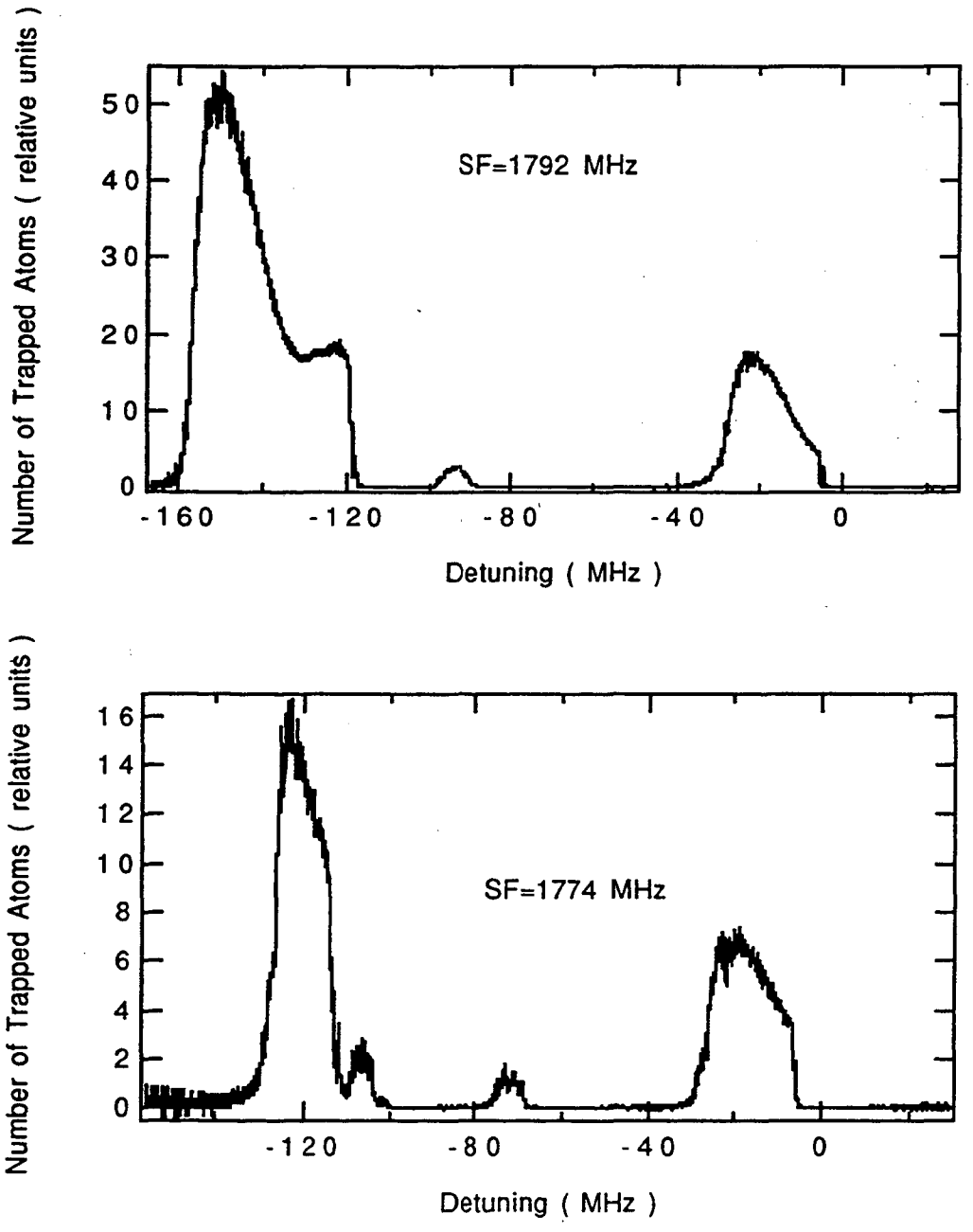

Figure 9.7 Frequency scans of the relative number of trapped atoms for 1792 MHz and 1774 MHz respectively, the relative number is calculated by deviding the measured fluorescence power (Fig 9.3) by the calculated fraction of excited level population.

Chapter X

A Study of Cold Collisions in a Magneto-Optical Trap

10.1 Cold Collisions

10.1.1 General Introduction

Neutral atom traps opened up a new field of cold atom-atom collision studies. In a trap, the relative velocity between atoms is only about 1 m/s, and density of 10^{10} atoms/cm^3 can easily be obtained. These conditions greatly enhance the rate of collisions between cold atoms. Furthermore, a large fraction of trapped atoms in excited levels makes it possible to study cold collisions of excited atoms.

It is important to study cold collisions for several reasons. First, cold collisions influence the applications of traps. For example, the number of trapped atoms is limited by loss rate from cold collisions. The performance of atomic clocks can be degraded with frequency shift caused by cold collisions [VE93]. Cold collisions themselves are interesting and still poorly understood.

Cold collisions in MOTs have been investigated extensively in recent years. The theory was reviewed in [JU93] by P. Julienne. Experimental works on the alkalis include

reference [RI94] on lithium, reference [PR88] and [MA93] on sodium, reference [HO92] and [WA92] on rubidium, and reference [SE89] on cesium.

10.1.2 Trap Loss

An atom can escape from a trap by colliding with a free thermal atom (or molecule) or with another trapped atom in an exorergic process. At high density, the effect of radiation trapping generates an effective density dependent force between trapped atoms [SE91], so the trap potential and the volume changes as the density decreases. However, in a certain regime when the density is below 10^9 atoms/cm^3, the small effect of radiation trapping can be neglected and the volume of trapped atoms is determined by only the effective temperature and the relatively constant trap potential, independent of the density. In this regime, we can assume that volume is constant. This assumption is verified in our experiments by measuring the sizes of a number of traps with different densities under the same laser and magnetic field condition. The density satisfies the equation:

$$\frac{dn}{dt} = -\alpha n - \beta n^2 \quad , \tag{10.1}$$

where n is the density of trapped atoms, α is the "thermal collisional loss constant", and β is the "cold collisional loss constant".

Inside a trap which captures atoms slower than 15 m/s, a collision between two atoms of 1 m/s can not eject an atom out of the trap unless there is excitation energy which

converts to kinetic energy (exorergic) during the collision process. In a trap of sodium atoms, there are two types of exorergic processes between atoms in excited levels:

$$A\left(^2P_{3/2}\right)+A\left(^2P_{3/2}\right)\rightarrow A\left(^2P_{3/2}\right)+A\left(^2S_{1/2}\right)+\hbar\omega'+\Delta E_{RE} \quad ,$$
$$A\left(^2P_{3/2}\right)+A\left(^2P_{3/2}\right)\rightarrow A\left(^2P_{3/2}\right)+A\left(^2P_{1/2}\right)+\Delta E_{FS} \quad .$$

The first process is the "radiative escape collision (RE)", in which one excited atom $A(^2P_{3/2})$ decays to the ground level $^2S_{1/2}$ during the collision process by emitting a red shifted photon with energy $\hbar\omega'$, less than the excitation energy in free space ($\hbar\omega$), and the difference $\Delta E_{RE}=\hbar\omega-\hbar\omega'$ is converted to kinetic energy. The second process is the "fine-structure changing collision (FS)", in which one atom originally in the excited state of $^2P_{3/2}$ is transferred to a $^2P_{1/2}$ state. The energy difference, $\Delta E_{FS}=E(^2P_{3/2})-E(^2P_{1/2})$, is picked up by atoms as kinetic energy. These two types of exorergic processes can also occur between a ground level atom and an excited level atom in similar ways:

$$A\left(^2P_{3/2}\right)+A\left(^2S_{1/2}\right)\rightarrow A\left(^2S_{1/2}\right)+A\left(^2S_{1/2}\right)+\hbar\omega'+\Delta E_{RE} \quad ,$$
$$A\left(^2P_{3/2}\right)+A\left(^2S_{1/2}\right)\rightarrow A\left(^2P_{1/2}\right)+A\left(^2S_{1/2}\right)+\Delta E_{FS} \quad .$$

Between two ground level atoms, there is an exorergic process called "Hyperfine-structure changing collisions (HFS)":

$$A\left(^2S_{1/2},F=2\right)+A\left(^2S_{1/2},F=2\right)\rightarrow A\left(^2S_{1/2},F=1\right)+A\left(^2S_{1/2},F=2\right)+\Delta E_{HFS} \, .$$

This process involves two atoms in the ground level $^2S_{1/2}$ with at least one of them in F=2 state before the collision. It drops to F=1 state during the collision process and the energy difference between F=2 and F=1 states is converted to kinetic energy,

$$\Delta E_{HFS} = E\left({}^2S_{1/2}, F=2\right) - E\left({}^2S_{1/2}, F=1\right).$$

The speed of atoms gained from RE and FS is on the order of 10^2 m/s, far exceeding the capture speed of a trap. Trapped atoms involved in these two processes definitely escape. The speed gained from HFS is less than 10 m/s. At high trapping-light intensities, the damping and restoring forces are stronger and the atoms involved in HFS processes can not escape the trap. Only at low trapping-light intensities does the trap loss due to HFS become possible. This type of loss process has been observed in Cs and Rb trap, but not in Na or Li trap. The reason is that Na and Li are lighter and the effect of the damping force is stronger. A Na atom gains about 6 m/s in speed in an HFS collision. In order to reveal the trap loss due to HFS, we estimated the trapping light intensity of each laser beam has to be about 2% of the saturation intensity, which is too low for the traps of previous works to trap observable amount of Na atoms. However, this extremely low intensity trap is achievable with our trap of high loading efficiency.

10.2 Collisional Loss of a Sodium Trap

The trap has been described in Chapter VI. The diameter of laser beams is 1 mm. In order to form a symmetric potential trap, the slowing laser beam is off-set so it does not pass the center of the trap. A particular leaky direction would make the comparison between experimental results and theoretical calculations difficult.

The time dependence of the atomic density is given by the function:

$$n(t) = \frac{1}{\left(\frac{\beta}{\alpha} + \frac{1}{n_0}\right)e^{\alpha t} - \frac{\beta}{\alpha}} \quad , \tag{10.2}$$

which is the solution to Equation 10.1. Data taking involved a simple sequence. First the trap is loaded with sodium atoms. After the number of trapped atoms reaches equilibrium, both atomic beam and slowing laser beam are simultaneously blocked by shutters. As the trap density decays, the fluorescence is monitored with a calibrated photo-diode (see Section 6.4.1). The measured fluorescence signal is fit with the function (see Figure 10.1)

$$P_{fluo} = K_0 + \frac{1}{K_1 \cdot \exp(K_3 t) - K_2} \quad ,$$
$$\text{here} \quad K_1 = \frac{1}{RV}\left(\frac{\beta}{\alpha} + \frac{1}{n_0}\right) \quad , K_2 = \frac{1}{RV} \cdot \frac{\beta}{\alpha} \quad , K_3 = \alpha \quad , \tag{10.3}$$

where K_0 is the background signal, V is the volume of the trap measured by the CCD camera (see Section 6.4.2), R is the ratio of the fluorescence signal to the number of trapped atoms, which is calculated by the Two-level atom model as described in Section 6.5. The relative error of α is 3% from the fit. The uncertainty in β is much larger, mainly generated in the calculation using R and V. The number of trapped atom has a relative error of 13% (see Section 6.6). The error of the trap volume is due to the 50 μ m spatial resolution of the CCD camera (see Section 6.4.2), the relative error of the volume of Type I traps (diameter = 0.5 mm) is 30% and of Type II traps (diameter = 1.0 mm) is 15%. Therefore, The value of β of Type I traps has a relative error of 33% and of Type II traps is 20%.

10.3 Collisional Loss Constant α

In the naive model on collisions where atoms are treated as classical rigid spheres, we get

$$\alpha = n_b \cdot v \cdot \sigma_{ther} \quad . \tag{10.4}$$

Here n_b is the density of background thermal atoms or molecules, v is the relative speed which is the averaged thermal speed of background particles, and σ_{ther} is the collision cross-section.

Figure 10.2 shows the light intensity dependence of α. The cause of this dependence is probably the velocity dependent collision cross-section σ_{ther}. In general, at lower light intensity the trap potential and the capture velocity are reduced, so σ_{ther} becomes larger.

10.4 Collisional Loss Constant β

10.4.1 Type II Trap

The Type II trap involves atoms mainly in F=1 states. HFS processes don't occur because they are energetically forbidden. Only RE and FS processes are the causes of trap loss.

In the naive classical model of collisions, we have the proportion relation

$$\beta \propto \frac{n_g}{n} \cdot \frac{n_e}{n} \cdot v \cdot \sigma_c \quad , \tag{10.5}$$

here n_g and n_e are the densities of atoms in the ground level and the excited level respectively, v is the relative speed which is about 1 m/s, and σ_c is the cross-section of collisions.

The values of β measured in Type II traps are shown in Figure 10.3. The data were taken in two experimental runs on different days. The consistency between the two runs shows that the data do not depend critically on laser alignment. For comparison, a theoretical prediction by L. Marcassa et al. [MA93] is shown in Figure 10.3.

The result shows that β increases with total light intensity. This is caused by the increases of n_e with the increasing excitation laser power. To better demonstrate this feature, let's introduce a new constant,

$$\beta^* = \frac{n}{n_g} \cdot \frac{n}{n_e} \cdot \beta \propto v \cdot \sigma_c \qquad (10.6)$$

Our model shows that β* only depends on the average velocity of trapped atoms and the collision cross-section, independent of the fraction of excited atoms and the light intensity. The calculated values of β* in traps of different light intensity are shown in Figure 10.4 . The constancy of β * supports our naive model.

10.4.2 Type I Trap

In a Type I trap, atoms in the ground level are mainly in F=2 states, where the HFS processes can occur.

The trap losses due to HFS processes are observed with total trapping laser intensity below 4 mW/cm^2, which corresponds to single beam intensity of 1/20 times the saturation intensity. Our trap of high loading efficiency enabled us to trap desired amount of atoms, even at a laser intensity another order of magnitude smaller.

When total laser intensity is above 4 mW/cm^2, RE and FS are the dominant mechanisms for trap loss. As for Type II traps, the data were also taken in two different experimental runs (see Figure 10.3). The agreement between this data and the theoretical prediction is not as good as for Type II traps, but the theoretical model does not take into account the hyperfine structure effect, e.g. the difference in n_e with transitions to different hyperfine states.

The values of β^* of Type I traps are also shown in Figure 10.4. When total laser intensity is above 20 mW/cm^2, the data shows the same constancy as for Type II traps. However, when total laser intensity goes below 20 mW/cm^2, β^* drops rapidly by an order of magnitude. The smaller β^* at low laser intensity is probably due to the decrease of relative velocity between trapped atoms as a result of sub-Doppler cooling. Previous studies indicate that sub-Doppler cooling mechanisms should be effective at low laser intensities on atomic transitions with multi-level ground states [LE89, ST91]. Sub-Doppler cooling on sodium atoms at the trapping transition of Type I traps, F=2 to F'=3, has been experimentally demonstrated, which lowered the effective sample temperature to 20 mK [LE89]. On the other hand, there is no sub-Doppler cooling mechanism for F=1 to F'=1 transition of Type II trap in one-dimensional models [CO90], it is likely to be absent in three-dimensional cases. Our β^* measurements imply that the temperature of trapped atoms drops by two orders of magnitude at total laser intensity of 10 mW/cm^2, to about 10 m K. A direct velocity measurement (or "temperature measurement") on

trapped atoms is needed in future experiments to further verify this hypothesis.

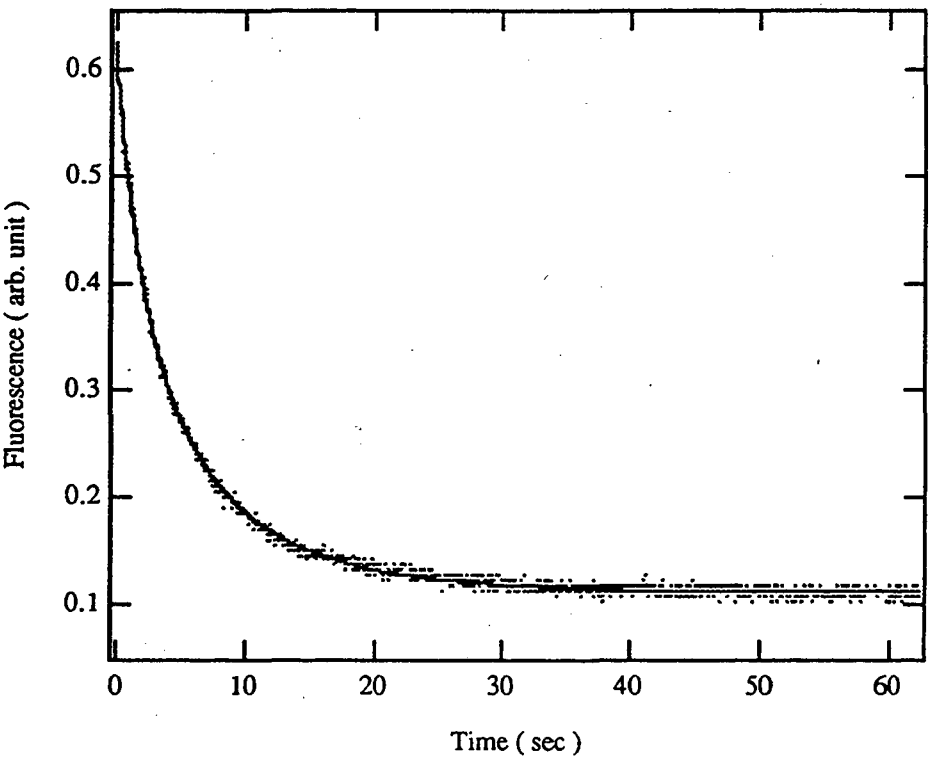

Figure 10.1 Decay of the fluorescence from a MOT after the atomic beam and the slowing laser beam are shut off. The dots are fluorescence signal taken by a photo-diode, the continuos line represents a fit to Equation 10.3, which yields $K_0 = 0.1112 \pm 0.0003$, $K_1 = 6.0 \pm 0.1$, $K_2 = 4.1 \pm 0.1$, $K_3 = (6.6 \pm 0.1) \times 10^{-3}$.

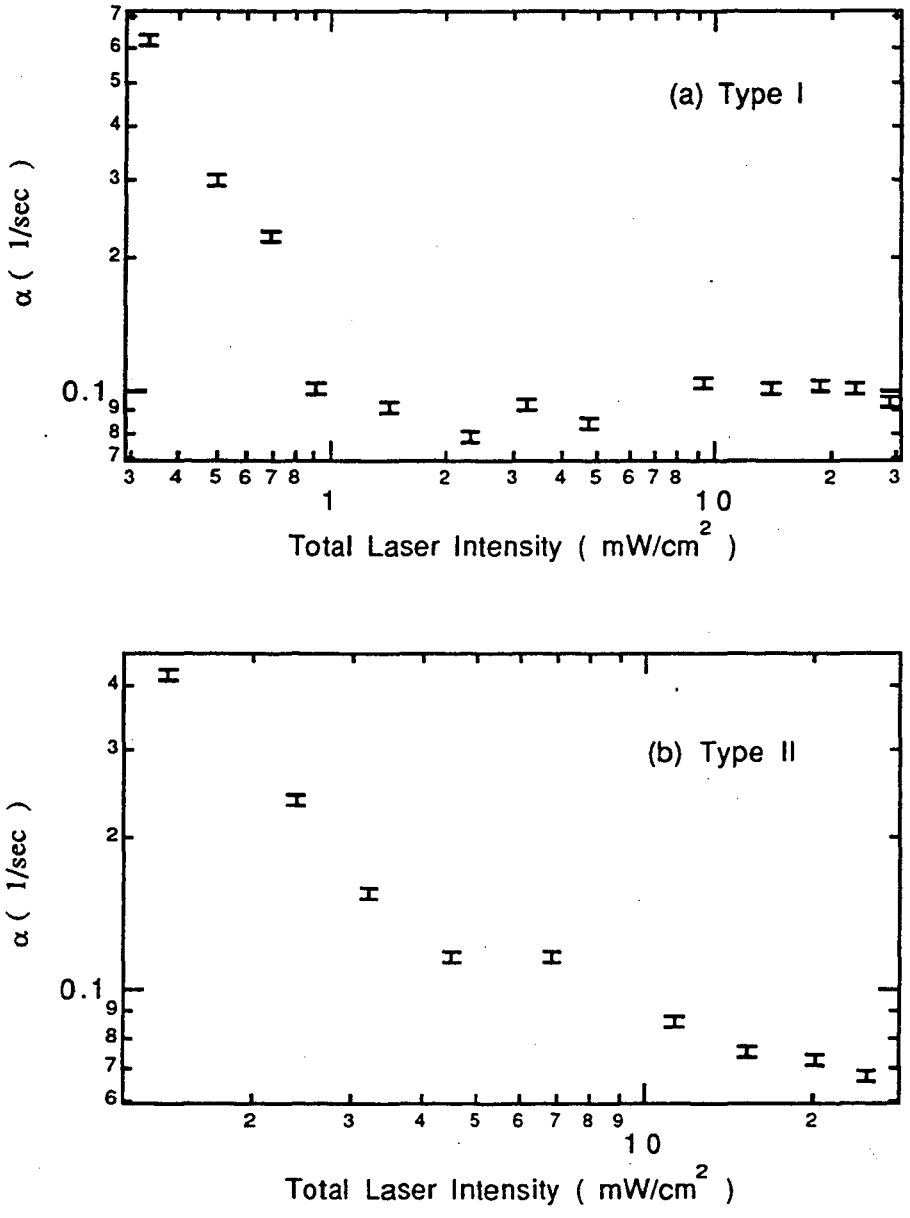

Figure 10.2 The thermal-collisional loss rate constant α as a function of the total laser intensity at the trap region. The vacuum pressure is 4×10^{-10} Torr. The relative error is 3%.

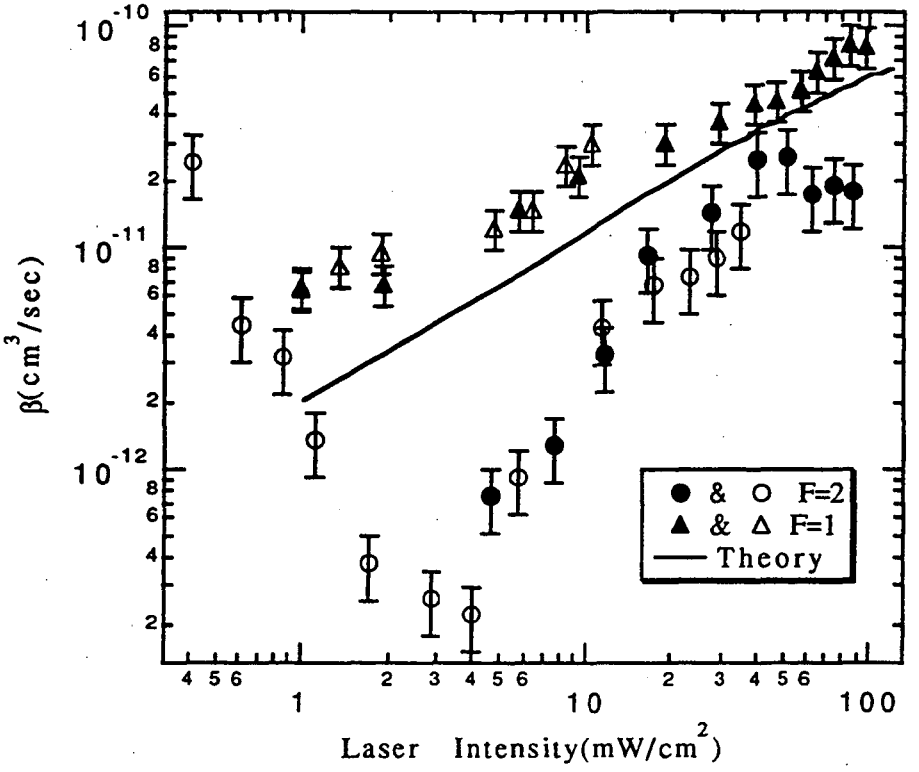

Figure 10.3 The cold-collisional loss rate constant β as a function of total (sum over the six beams) trapping laser intensity. The laser frequency is detuned 10 MHz below F=2 to F'=3 transition for Type I traps, and detuned 21 MHz below F=1 to F'=1 transition for Type II traps. The sideband frequency splitting is 1712 MHz in both cases. The solid curve is a theoretical prediction from [MA93]. Each data of Type I traps has a relative error of 33%, of Type II traps has a relative error of 20%. Solid and open points indicate data from separate runs of the experiment.

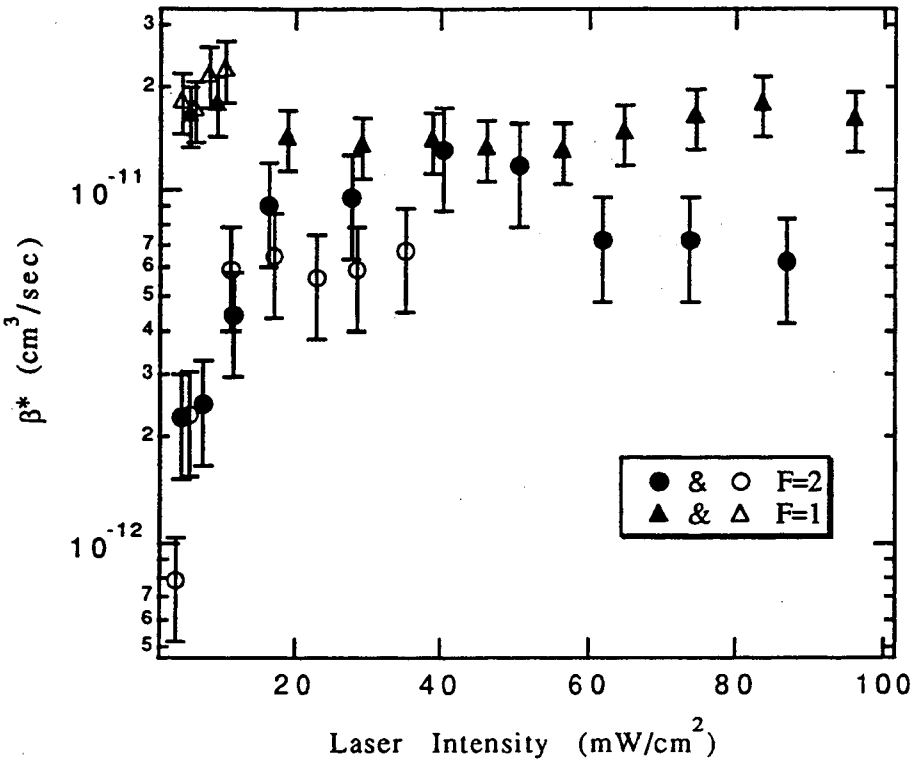

Figure 10.4 The cold-collisional loss rate constant β* as a function of laser intensity. The constancy of β* of Type II traps supports our naive cold collision model, the smaller β* of Type I traps at low laser intensity region may be a result of sub-Doppler cooling. Each data of Type I traps has a relative error of 33%, of Type II traps has a relative error of 20%. Solid and open points indicate data from separate runs of the experiment.

Appendix A

The D2 line of ^{21}Na & ^{23}Na

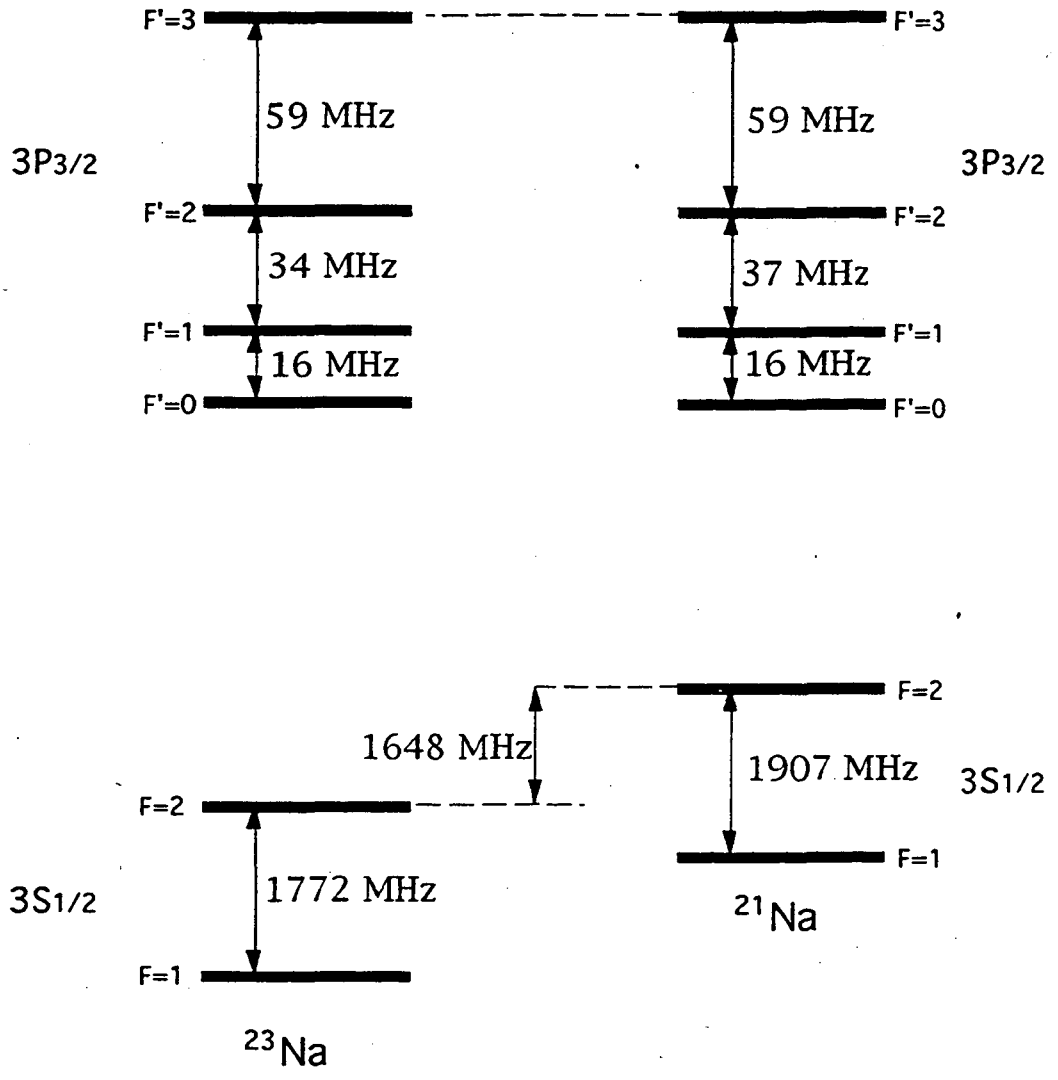

Wavelength 589 nm;

Lifetime of the excited states 16 ns;

Appendix B

Relative Oscillator Strengths [UN89]

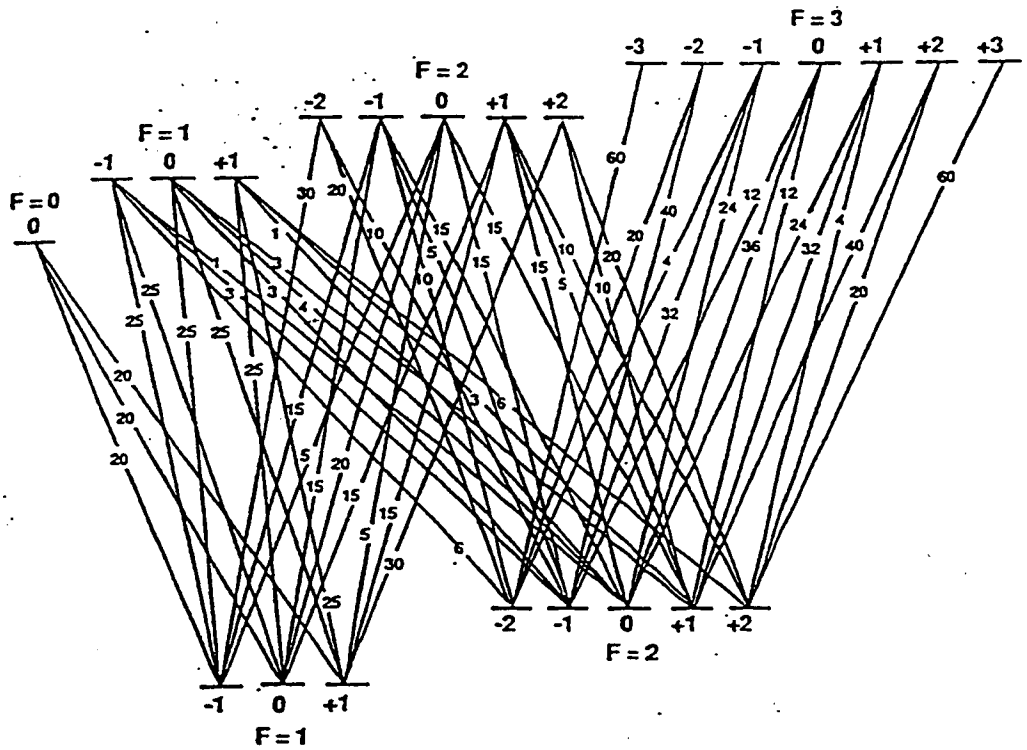

The relative oscillator strength is proportional to the square of electric dipole transition matrix, $f_{osc} \propto |\langle \text{excited state} \mid d \mid \text{ground state} \rangle|^2$, it is used to calculate transition probablities.

Appendix C

Nuclear Decay Properties of ^{21}Na [LE78]

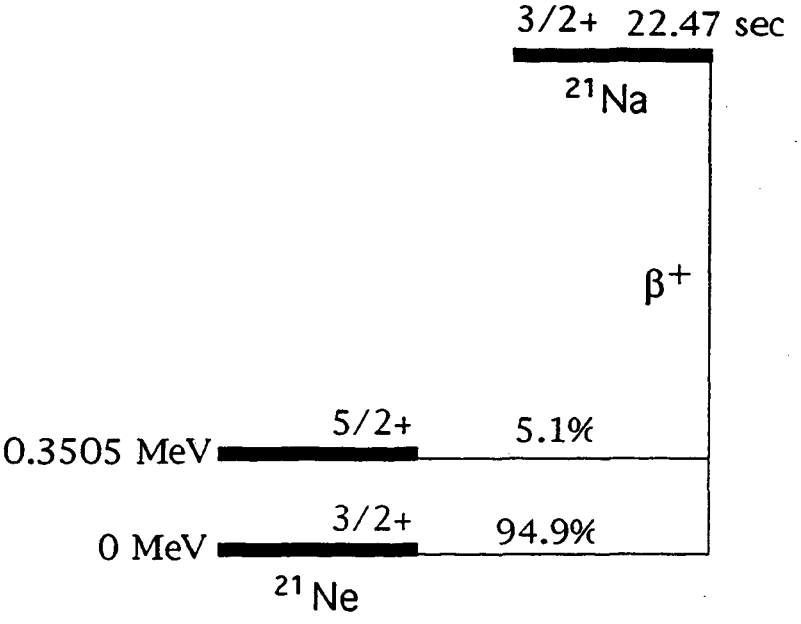

Radiation	β^+	2.51 MeV ;
	γ	0.351 MeV .

The $3/2^+$ state of ^{21}Na and the $3/2^+$ state of ^{21}Ne are isosping doublets, the transition between them is called "mirror decay", the beta-asymmetry parameter of this transition is to be measured to search for the right-handed current in charged-current weak interaction processes.

Reference

[AM65] O. Ames et al., Phys. Rev. **137**, B1157 (1965)

[AM93] C. Aminoff et al., Phys. Rev. Lett. **71**, 3083 (1993)

[AD93] E. Adelberger, Phys. Rev. Lett. **70**, 2856 (1993)

[BA77] R. Baltrusaitis et al., Phys. Rev. Lett. **38**, 464 (1977)

[BA91] T. Barrett et al., Phys. Rev. Lett. **67**, 3483 (1991)

[BE77] M. Bég et al., Phys. Rev. Lett. **38**, 1252 (1977)

[BO68] J. H. de Boer, The dynamical character of adsorption, Oxford, (1968)

[BO74] M. Bouchiat et al., Phys. Lett. **48B**, (1974)

[BO86] P. Bopp et al., Phys. Rev. Lett. **56**, 919 (1986)

[CA75] F. Calaprice et al., Phys. Rev. Lett. **35**, 1566 (1975)

[CA78] L. C. Carraz et al., Nucl. Inst. Meth. **148**, 217 (1978)

[CH80] L. Chirovsky et al., Phys. Lett. **94B**, 127 (1980)

[CL29] P. Claussing, Physica **9**, 65 (1929)

[CO55] B. Cohen et al., Phys. Rev. **99**, 723 (1955)

[CO77] A. Corney, Atomic and Laser Spectroscopy (1977)

[CO83] E. D. Commins & P. H. Bucksbaum, Weak Interactions of Leptons and Quarks, Cambridge Univ. Press (1983)

[CO90] C. Cohen-Tannoudji, Fundamental Systems in Quantum Optics, edited by J. Dalibard et al., North-Holland (1990)

[ER85] W. Ertmer et al., Phys. Rev. Lett. **54**, 996 (1985)

[GA88] J. Garnett et al., Phys. Rev. Lett. **60**, 499 (1988)

[GR77] W. Gruhle and B. Kober, Nucl. Phys. **A 286**, 523 (1977)

[HA75] T. Hansch & A. Schawlow, Opt. Commun. **13**, 68 (1975)

[HO54] J. Hobson et al., Phys. Rev. **96**, 1450 (1954)

[HO89] B. Holstein, Weak Interactions in Nuclei, Princeton Univ. Press, (1989)

[HO92] D. Hoffmann et al., Phys. Rev. Lett. **69**, 753 (1992)

[JO86] A. Jodidio et al., Phys. Rev. **D 34**, 1967 (1986)

[JO89] J. Opt. Soc. Am. **B V6**, No.11 (1989)

[JO93] M. Joffe et al., J. Opt. Soc. Am. **B 2257** (1993)

[JU93] P. Julienne et al., Adv. Ato. Mol. Opt. Phys. **30**, 141 (1993)

[KA91] M. Kasevich et al., Phys. Rev. Lett. **67**, 181 (1991)

[KE87] J. Kelly and A. Gallagher, Rev. Sci. Inst. **58**, 563 (1987)

[LE56] T. Lee and C. Yang, Phys. Rev. **104**, 254 (1956)

[LE78] C. M. Lederer et al., Table of Isotopes, 7th ed., (1978)

[LE88] P. D. Lett et al., Phys. Rev. Lett. **V61**, 169 (1988)

[LE89] P. D. Lett et al., J. Opt. Soc. Am. **B V6**, 2084 (1989)

[LI90] D. R. Lide, CRC handbook of chemistry and physics, CRC, (1990-1991)

[LI92] K. Lindquist et al., Phys. Rev. **A V46**, 4082 (1992)

[MA90] W. Marciano et al., Phys. Rev. Lett. **V65**, 2963 (1990)

[MA91] M. Macpherson et al., Phys. Rev. Lett. **67**, 2784 (1991)

[MAS90] G. Masson & P. Quin, Phys Rev C **42**, 1110 (1990)

[MA93] L. Marcassa et al., Phys. Rev. **A 47**, R4563 (1993)

[ME51] J. Meadows and R. Holt, Phys. Rev. **83**, 1257 (1951)

[ME93] D. Meekhof et al., Phys. Rev. Lett. **71**, 3442 (1993)

[MO90] C. Monroe et al., Phys. Rev. Lett. **65**, 1571 (1990)

[NA91] O. Naviliat-Cuncis et al., J. Phys. **G 17**, 919 (1991)

[NO88] M. Noecker et al., Phys. Rev. Lett. **61**, 310 (1988)

[PA93] C. N. Pannell et al., J. Opt. Soc. Am. **B 10**, 684 (1993)

[PE84] P. Drell & E. Commins, Phys. Rev. Lett. **53**, 968 (1984)

[PH82] W. Phillips & H. Metcalf, Phys. Rev. Lett. **48**, 596(1982)

[PR82] J. Prodan et al., Phys. Rev. Lett. **49**, 1149 (1982)

[PR83] D. Pritchard, Phys. Rev. Lett. **51**, 1336 (1983)

[PR85] J. Prodan et al., Phys. Rev. Lett. **54**, 992 (1985)

[PR88] M. Prentiss et al., Opt. Lett. **13**, 452 (1988)

[RA56] N. Ramsey, Molecular Beams, Oxford University Press (1956)

[RA87] E. Raab et al., Phys. Rev. Lett. **59**, 2631 (1987)

[RI94] N. Ritchie et al., submitted to Phys. Rev. Lett

[SE89] D. W. Sesko et al., Phys. Rev. Lett. **63**, 961 (1989)

[SE91] D. W. Sesko et al., J. Opt. Soc. Am. **B V8**, 946 (1991)

[SEV89] N. Severijns et al., Phys. Rev. Lett. **63**, 1050 (1989)

[SH89] F. Shimizu et al., Phys. Rev. **A 39**, 2758 (1989)

[SH90] F. Shimizu et al., Chem. Phys. **145**, 327 (1990)

[SH91] F. Shimizu, Opt. Lett. **16**, 339 (1991)

[SHA91] S-Q. Shang et al., Phys. Rev. Lett. **67**, 1094 (1991)

[SH94] S-Q. Shang et al., submitted to Phys. Rev. Lett.

[SHU91] Howard Shugart, private communication.

[SM72] R. G. Smith, Appl. Opt. **11**, 2489 (1972)

[ST91] A. Steane and C. Foot, Europhys. Lett. **14**, 231 (1991)

[ST92] D. Stacey, Atomic Physics 13, ed. by H. Walther et al., AIP (1992)

[ST94] M. Stephens and C. Wieman, Phys. Rev. Lett. **V72**, 3787 (1994)

[TO81] F. Touchard et al., Nuc. Ins. Methods **186**, 329 (1981)

[TO82] F. Touchard et al., Phys. Rev. **C 25**, 2756 (1982)

[UN89] P. Ungar et al., J. Opt. Soc. Am. **B V6**, 2058 (1989)

[VE93] B. Verhaar et al., Phys. Rev. **A V48**, R3429 (1993)

[WA92] C. Wallace et al., Phys. Rev. Lett. **69**, 897 (1992)

[WA93] M. Walhout et al., Phys. Rev. **A 48**, R879 (1993)

[WE79] Vacuum Physics and Technology, edited by G. L. Weissler et al., Academic Press, Inc. (1979)

[WI75] D. Wineland et al., Bull. Am. Phys. Soc. **20**, 637 (1975)

[WI78] D. Wineland et al., Phys. Rev. Lett. **40**, 1639 (1978)

[WU57] C. Wu et al., Phys. Rev. **105**, 1413 (1957)

LAWRENCE BERKELEY LABORATORY
UNIVERSITY OF CALIFORNIA
TECHNICAL INFORMATION DEPARTMENT
BERKELEY, CALIFORNIA 94720